Towards reverse engineering of Photosystem II: Synergistic Computational and Experimental Approaches

Abdullah Mahboob, B.Sc.

Biotechnology, PhD

Submitted in partial fulfillment of the requirements for the degree of

Doctor of Philosophy

Faculty of Mathematics and Sciences, Brock University St. Catharines, Ontario

ABSTRACT

Photosystem II (PSII) of oxygenic photosynthesis has the unique ability to photochemically oxidize water, extracting electrons from water to result in the evolution of oxygen gas while depositing these electrons to the rest of the photosynthetic machinery which in turn reduces CO_2 to carbohydrate molecules acting as fuel for the cell. Unfortunately, native PSII is unstable and not suitable to be used in industrial applications. Consequently, there is a need to reverse-engineer the water oxidation photochemical reactions of PSII using solution-stable proteins. But what does it take to reverse-engineer PSII's reactions? PSII has the pigment with the highest oxidation potential in nature known as P680. The high oxidation of P680 is in fact the driving force for water oxidation. P680 is made up of a chlorophyll *a* dimer embedded inside the relatively hydrophobic transmembrane environment of PSII. In this thesis, the electrostatic factors contributing to the high oxidation potential of P680 are described. PSII oxidizes water in a specialized metal cluster known as the Oxygen Evolving Complex (OEC). The pathways that water can take to enter the relatively hydrophobic region of PSII are described as well. A previous attempt to reverse engineer PSII's reactions using the protein scaffold of *E. coli*'s Bacterioferritin (BFR) existed. The oxidation potential of the pigment used for the BFR 'reaction centre' was measured and the protein effects calculated in a similar fashion to how P680 potentials were calculated in PSII. The BFR-RC's pigment oxidation potential was found to be 0.57 V, too low to oxidize water or tyrosine like PSII. We suggest that the observed tyrosine oxidation in BRF-RC could be driven by the $ZnCe_6$ di-cation. In order to increase the efficiency of

tyrosine oxidation, and ultimately oxidize water, the first potential of $ZnCe_6$ would have to attain a value in excess of 0.8 V. The results were used to develop a second generation of BFR-RC using a high oxidation pigment. The hypervalent phosphorous porphyrin forms a radical pair that can be observed using Transient Electron Paramagnetic Resonance (TR-EPR). Finally, the results from this thesis are discussed in light of the development of solar fuel producing systems.

ACKNOWLEDGEMENT

I would like to express my deepest gratitude to Dr. Doug Bruce for giving me the very exciting opportunity to work on this project in his laboratory. His advice, his patience, and his enthusiasm were the main reason for the success of my PhD.

I would like to thank the members of the Doug Bruce lab: Dr. Sergey Vassili'ev, Kristin Schaven, and Allen Derks for their help with using equipment and insightful discussions. In addition to Dr. Bruce's lab, Dr. van der Est and his group have been of utmost importance in helping me conduct EPR experiments and advice on synthesis work from Dr. Prashanth Poddutoori.

Finally, I would like to thank my family for their never-ending moral support through the past years.

Table of Contents

List of Tables

List of Figures

Chapter 1

The use of computational methods to study natural Photosystems and how they provide guidance in the design of artificial ones: A literature review and background to the thesis

1.1 THE OVERALL VISION: REVERSE ENGINEERING OF PHOTOSYSTEM II

The ability of Oxygenic Photosynthesis to utilize light's energy to drive the formation of chemical bonds through redox reaction chains in which water is the electron donor has grand implications to solve an upcoming world energy crisis of peak oil (Gust, Moore, and Moore 2009). One solution envisioned in this thesis is to use what we can learn from natural Photosynthesis to design much simpler and direct redox reaction chains, which still use water as the ultimate electron source. In order to avoid the high cost of synthesis of novel catalysts, proteins from the bacterium *E. coli* are used as the scaffold. But what are the requirements to reverse-engineer a water-oxidizing electron transport chain? A few questions were taken into consideration in this work. These questions were concerned with the natural protein water-oxidizing system known as Photosystem II, and an artificial protein-based "Photosystem" created by engineering the *E. coli* protein scaffold of Bacterioferritin. Photosystem II uses a multi-step charge separation process to eventually oxidize water. This work begun by investigating how Photosystem II's charge separation reactions may affect the role of the protein in subsequent reactions, including regulating the access of water to the Oxygen Evolving Complex (OEC). Work continued to determine if there were any mechanisms in PSII that could be reverse-engineered in artificial photosynthetic proteins. It has been known that the driving force of water oxidation is the high potential of the electron donor pigment in Photosystem II, known as P680. One question that could be answered using computational methods is how does Photosystem II control the redox potential of P680? P680 is a dimer of chlorophyll *a* molecules. The oxidation potential of P680 is increased by approximately 600mV from

the potential of chlorophyll *a* aqueous solution. These questions were addressed in **Chapter 2 and Chapter 3**. The same methods that were used to study the mechanism of regulating the access of water into Photosystem II and the regulation of the oxidation potential of P680 were then used on the engineered Bacterioferritin "Photosystem". The results from that work are given in **Chapter 4**. These purely computational results helped in guiding the experimental work discussed in **Chapter 5** to develop a second generation of Bacterioferritin "Photosystem". The second generation of Bacterioferritin "Photosystem" behaves similarly to Photosystem II in the sense that charge separation can be observed using Time-Resolved EPR (TR-EPR) and Fluorescence Decay Kinetics. Finally, demonstration of the system's ability to oxidize a protein residue and reduce NAD cofactors has been done. Implications of these results to the development of an open electron transport chain in which water is the ultimate electron donor and CO_2 is the ultimate electron acceptor are discussed in **Chapter 6**. Such a system would constitute a Biohybrid platform technology to photochemically generate liquid solar fuel in a cell-free protein-based system.

1.2. HISTORIC BACKGROUND ON OXYGENIC PHOTOSYNTHESIS RESEARCH

Oxygenic photosynthesis is undoubtedly one of the most important chemical reactions occurring on the Earth. It is responsible for the production of oxygen gas by splitting water and hence sustaining all higher life forms. As a matter of fact, it is generally accepted that it was the initial oxygenic photosynthesis of cyanobacteria which introduced oxygen to the planet's atmosphere, consequently allowing the evolution of

oxygenic respiration (Farquhar, Zerkle, and Bekker 2011). Aside from its critical role as a supplier of oxygen gas, oxygenic photosynthesis is the precursor step to the anabolic process of carbon fixation responsible for producing basic sugars from carbon dioxide in higher plants and algae, hence maintaining all major food chains (Barber 2003; Witt 1996). The reverse-engineering of water oxidation and carbon dioxide reduction in a simple photochemical electron chain has been the "holy grail" of solar fuel research (Gust, Moore, and Moore 2009).

Joseph Priestly could be considered the first photosynthesis researcher. In 1772, he made observations concerning the ability of plants to "restore air which has been injured by burning of candles" (Huzisige and Ke 1993). In 1845, the need for carbon dioxide and water in the overall process of photosynthesis was established by Julius Robert Mayer, followed by the discovery of chlorophyll as the major light-absorber in the reaction which utilizes carbon dioxide and water to make oxygen and a simple sugar denoted as [CH_2O]. The overall reaction of photosynthesis was understood to be as follows:

Scheme 1: $$CO_2 + H_2O \rightleftharpoons [CH_2O] + O_2$$

Robert Hill performed a very famous experiment in 1937 in which he decoupled the production of oxygen from organic matter synthesis in chloroplasts using an inorganic oxidant as a terminal electron acceptor. Through this experiment, he observed that the source of the oxygen atoms in the oxygen gas produced by the process of photosynthesis is water and not carbon dioxide (Hill 1937).

The early events of oxygenic photosynthesis consist of capturing photons and converting their energy into chemical energy. In 1932, Robert Emerson and William Arnold measured the rate of the photochemical reaction within a green algae species. Through the construction of rate equations, it was found that several hundred chlorophyll molecules participate in oxygen production. This experiment and others similar to it helped establish the concept of a photosynthetic unit (Emerson and Arnold 1932). The concept of photosynthetic unit was described by Kurt Wohl in 1936 to be an assembly of pigment molecules which function to supply excitation energy to a reaction centre that powers photosynthesis. Hence the consensus that the early events in photosynthesis comprising the capturing of light energy and converting it into chemical energy was established.

Early events of Photosynthesis occur via two membrane embedded multiprotein subunits known as PSI and PSII (Photosystem I and Photosystem II respectively).

The chemical reactions in PSI and PSII are linked together through $Cytb_{6/f}$ which acts along with PSI and PSII in an electron transport chain with a goal to release H^+ ions into the thylakoid in order to use the energy of the pH gradient to convert ADP to ATP through the ATPase complex (Cardona et al. 2012).

The discovery of the above mentioned process came about when Hill and Bendall suggested that there are two light reactions occurring during the process of photosynthetic electron transport. These two reactions in order for them to function together require

cytochromes. Light-induced absorbance change measurements were subsequently done and characterized the two reaction centres further, assigning the wavelengths 700 and 680 for PSI and PSII respectively. The link between PSI and PSII was found to be a plastoquinone molecule that travels to the Cyt $_{b\ 6/f}$ complex (Govindjee and Krogmann 2004).

Oxygen gas has been known since the time of Joseph Priestly to be a by-product of photosynthesis. The mechanism of its production; however, was initially studied by Pierre Joliot and Bessel Kok. The question was how could the one electron process of light-induced electron transfer be coupled to the four electrons process of oxidizing water to oxygen gas? In Joliot's experiment, exposing algal suspensions to a series of light flashes, very little oxygen gas was produced after the 1^{st} flash, very little after the 2^{nd}, while the maximum is made after the 3^{rd} flash. The production of oxygen was observed to be in periods of four. Bessel Kok used Joliot's data to propose that a specialized complex goes through different states known as the S_n states where n is a number between 0 and 4. The S states represent a step-wise accumulation of oxidation equivalent, until S_4 is reached, at which point Oxygen gas is produced (Kok, Forbush, and McGloin 1970). Numerous mutation and spectroscopic studies have pointed to a manganese complex, currently known as the Oxygen Evolving Complex (OEC) in PSII as the site of oxygen evolution (Nelson and Ben-Shem 2004).

The OEC acts to accumulate oxidation equivalents. However, the driving force of water oxidation is the high oxidation potential of the special pair chlorophyll in PSII, known as

P680 due its maximum absorbance wavelength. The P680 radical has the highest oxidation potential in nature. Electron transfer reactions start at the reaction centre in which the excited state of P680 is quenched through an electron transfer reaction to a metal-free chlorophyll *a* molecule known as Pheophyrin D1 ($Pheo_{D1}$). Oxidation of P680 by a pheophytin electron acceptor initiates the charge separation process. Once $Pheo_{D1}$ accepts an electron from P680, that electron is transferred to a secondary electron acceptor, known as $Plastoquinone_A$ (Q_A) and subsequently $Plastoquinone_B$ (Q_B). $Pheo_{D1}$ and then Q_A and Q_B are progressively further from P680, creating a more stable charge separated pair with each electron-accepting step. In order to replenish this electron lost to $Pheo_{D1}$, Photosystem II uses the OEC. This complex in turn oxidizes water using water oxidation to oxygen as the ultimate electron source. It is important to note that the driving force for the oxidation of water is the high oxidation potential of the P680 radical. It is that high potential that drives the electron flow from water to replenish the electron lost in P680. The electron from the OEC goes through a tyrosine residue known as (Tyr_Z). The electron transfer in PSII is not cyclic. The electron lost from P680 is not recycled back through, but the oxidation water into oxygen serves to replenish the lost electron from P680. Once the lost electron from P680 is replenished, another excitation of P680 causes a second flow of electrons from P680 to Q_B. At this point Q_B has a double negative charge and gets protonated to leave the PSII complex as PQH_2.

PQH_2 travels within the membrane to the $Cytb_{6/f}$ complex to which it donates electrons through the cytochrome complex to plastocyanin (PC) through a process known as the quinone cycle. PC is a small soluble protein that is membrane-associated and migrates to

PSI carrying an electron to P700. Similar to P680, P700 is the special pair in PSI and gets excited and eventually loses an electron to a chlorophyll acceptor known as $Acceptor_0$ (A_0), which then transfers the electron to a secondary acceptor, a phylloquinone molecule labeled $Acceptor_1$ (A_1). The electron then travels to a series of Iron Sulfur complexes and ferredoxin eventually leading to the reduction of an $NADP^+$ molecule into an NADPH (Witt 1996). The reduction of NADP to NADPH is a two electrons reduction. It takes two electrons which original from P680 to reduce one NADP to NADPH. P680's lost electron is replenished by the oxidation of the OEC, which in turn oxidizes water. Water oxidation to oxygen is a four-electron process. The replenishment of the P680's lost electron through the OEC is coupled to water oxidation. In this manner, PSII links the four-electrons reaction of water oxidation to the one-electron process of charge separation. This link was initially established by Joliot and Kok (Joliot, Barbieri, and Chabaud 1969). The protons from the water oxidation reaction are ejected into the lumen. The release of protons into the thylakoid lumen, generates an electrochemical gradient which is used by ATPase to convert ADP to ATP, hence converting light's energy into chemical energy stored in the high energy bonds of the ATP molecule. While photosystem II is a Q-type reaction centre (type II) in which the quinone molecules are the final electron acceptors, photosystem I is a type I reaction centre, also known as FeS reaction centre as the final electron acceptor is an Iron Sulfur cluster. The light reactions are shown in the Z-Scheme in figure 1.1. In terms of energetics the electron acceptors are positioned in a downward manner making electron transfer favourable. Due to this arrangement, the energy of the electron is much lowered by the time it gets to P700, too low to transfer to the final NADP+ electron -acceptor. Nature solved this problem by making P700 another special

pair and hence the energy of a second photon gives a “boost” to the electron arriving at PSI. $NADP^+$ is reduced to NADPH. The NADPH molecules are then used in the anabolic process of carbon fixation. Following the electrons from water in PSII. The four electrons from water are used to eventually to produce NADPH.

Within the context of studying natural Photosystems to develop artificial ones, one needs to consider that what the” blind-watchmaker” known as evolution came up with is not necessarily the solution we should aim to design. In fact, the solution one should aim for is a simpler one. The lesson from oxygenic photosynthesis is that one can take electrons from water and deliver them to a final electron acceptor. It is for this reason that the rest of this chapter and the next chapter are concerned only with Photosystem II.

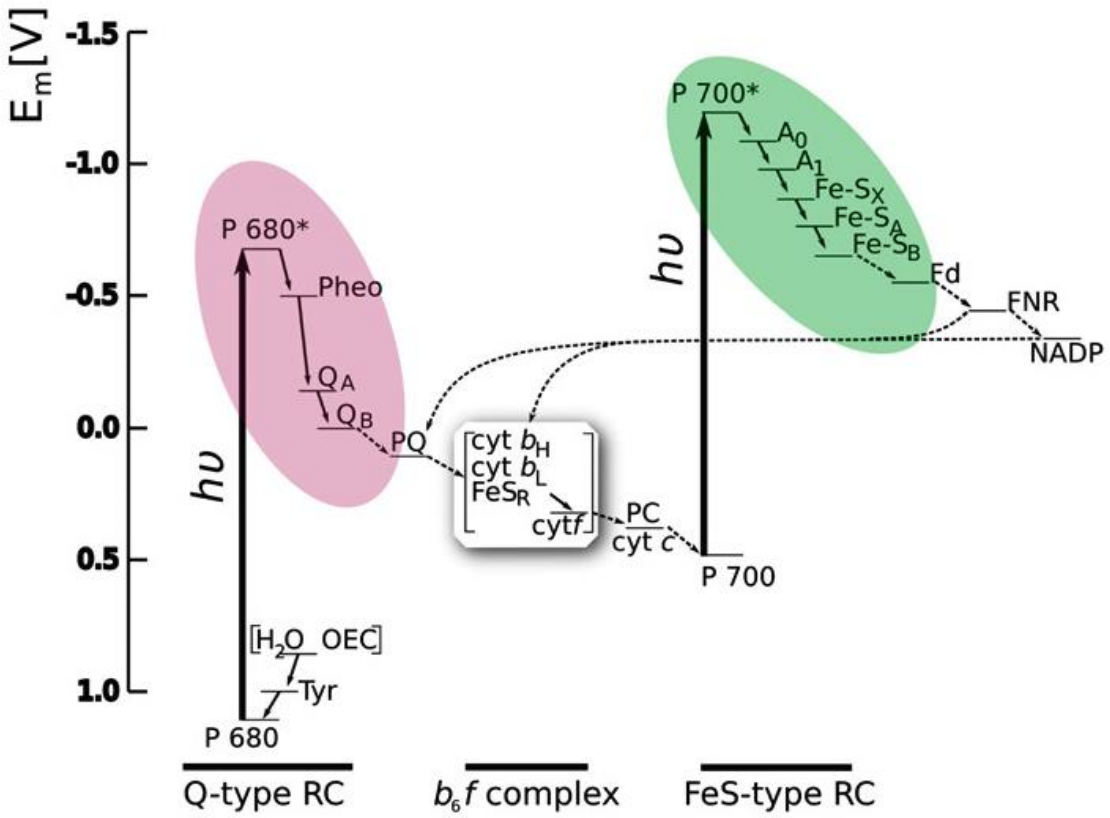

Figure 1.1. The Z-Scheme showing electron transfer during the light reactions of Oxygenic Photosynthesis (Reproduced from Blankenship (2010) with permission)

1.3. PHOTOSYSTEM II

The photochemically-driven production of oxygen gas from the oxidation of water is achieved in the enzymatic 20 subunit complex known as PSII. PSII is described as a light-enabled Water : Plastoquinone oxidoreductase (Barber 2003). PSII performs the redox reaction that can be described in the two half-reactions as follows:

Scheme 2: $2H_2O + 4e^- \rightarrow O_2 + 4H^+$ (I)

$2PQ + 4e^- + 2H^+ \rightarrow 2PQH_2$ (II)

Both of reaction I and reaction II contribute to the creation of a proton gradient across the membrane. The proton gradient contributes to the production of ATP through ATPase. The production of ATP occurs on the stromal side. Reaction I is an oxidation reaction in which water is oxidized into oxygen while reaction (II) is a reduction reaction in which PQ is reduced to PQH_2. Reaction I occurs in the lumenal side of PSII while reaction II occurs in the stromal side of the thylakoid membrane. PSII functions to remove protons from the stromal side while populating the lumenal side with protons. The gradient is used with ATPase to phosphorylate ADP. PQH_2 travels to $Cyt6_{b/f}$ and becomes oxidized again losing its two protons to the lumenal side adding to the gradient.

PSII's many proteins can be divided into the following categories: Reaction Centre (RC) which contains the proteins D1, D2, and Cytb559, Core antennas (CP43 and CP47), and small protein subunits, such as: Photosystem II 33 kDa manganese-stabilizing polypeptide, Photosystem II 12 kDa extrinsic protein as they are responsible for stabilizing the OEC, and cytochrome c-550 as it holds the two heme groups found in PSII. Figure 1.2 shows this arrangement in a PSII dimer (Krausz et al. 2005).

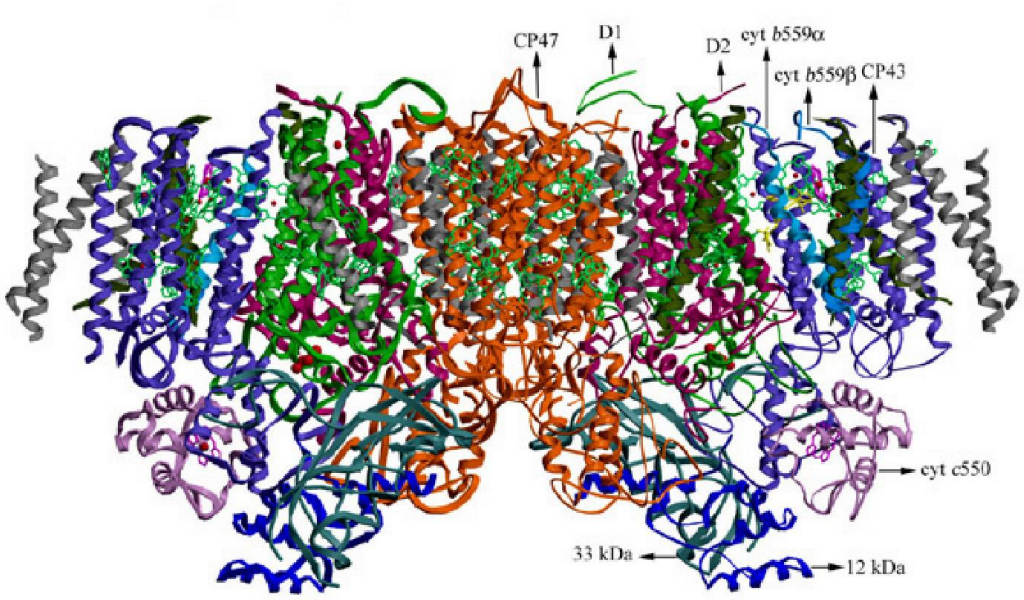

Figure 1.2. Structure of PSII dimer showing subunits CP47,D1,D2,cyt *b*559,CP43,cyt *c*550, 12kDa and 33kDa

The reaction centre of PSII contains polypeptides D1 and D2 that bind all the molecules composing the acceptor side of PSII's charge separation. D1 and D2 are very similar proteins in their sequence and structure and make a two fold pseudo-symmetry (Dekker and Van Grondelle 2000). Each of D1 and D2 consist of a 5 transmembrane alpha helices that contain 5 pigments and two alpha helices which lie parallel to the membrane one on each side. The sequence of D1 and D2 is remarkably conserved both among PSII-bearing organisms, as well as Bacterial Reaction Centres (Hohmann-Marriott and Blankenship 2011). Each of D1 and D2 holds three chlorophylls, a pheophytin, and a plastoquinone as their co-factors. Two chlorophylls, one from D1 and the other from D2, make up the P680 pigment; another chlorophyll is called an "accessory chlorophyll" Chl_{D1} which is believed to be the initiator of charge separation. The last chlorophyll is named Chlz. Chlz

is believed to be involved in an alternative pathway to charge separation. D1 and D2 are held together through a non-heme iron to which two HIS residues from D1 and two HIS residues from D2 coordinate (Dekker and Van Grondelle 2000).

PSII's reaction centre is a heterodimeric reaction centre. Containing D1 and D2 proteins, despite of the similarity in structure and sequence between D1 and D2, charge separation reactions happen only on the D1 side. This observation was explained through the comparison between D1 and D2 electrostatic environments which demonstrated that the D2 side of the protein is not suitable for the charge separation events to occur (Gunner, Robertson, and Dutton 1986). Pigment arrangement inside the reaction centre of PSII is shown in figure 1.3. The pigments can be categorized into the active or the protective branch if they are on the D1 or D2 sides respectively. It is important to note that the protective branch also contains Q_B, which is an active component in charge separation and the final electron acceptor in PSII.

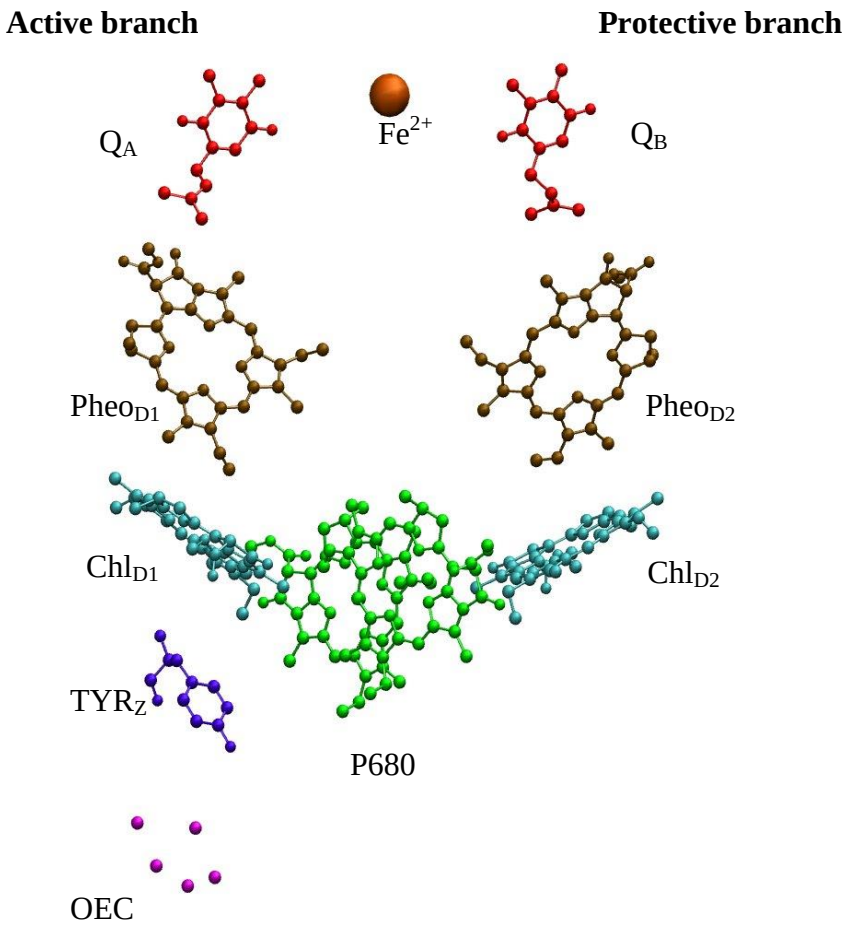

Figure 1.3. Arrangement of pigments inside the RC-PC showing both the active and the protective branches (D1 and D2 sides respectively)

1.4. CHARGE SEPARATION IN PSII

The excitation of a pigment by a photon of light consists of promoting an electron from its Highest Occupied Molecular Orbital (HOMO) to its Lowest Unoccupied Molecular Orbital (LUMO). In the spectra of chlorophyll *a*, transitions from HOMO to LUMO and HOMO-1 to LUMO are assigned to the Q bands; while transitions from HOMO to

LUMO+1 and HOMO-1 to LUMO+1 are assigned to the Soret band(J. Hasegawa et al. 1998). An excited electron can either return from LUMO to HOMO (with the energy released as heat or fluorescence) or becomes transferred to another pigment resulting in the formation of a radical cation and a radical anion (charge separation). Charge separation is the methodology utilized by photosynthetic reaction centres to achieve electron transport (Hohmann-Marriott and Blankenship 2011).

Excitation energy moves through the CP47 and CP43 chlorophylls, eventually arriving at Chl_{D1} which forms the initial radical pair with $Pheo_{D1}$($Chl_{D1}^{+}Pheo_{D1}^{-}$) (Prokhorenko and Holzwarth 2000).

Upon the formation of the initial radical pair in the reaction centre, the energy of the photon of light captured with antenna chlorophylls is converted to the radical pair. Subsequent to the formation of the initial radical pair, the charge moves from the Chl_{D1} pigment to the dimer chlorophyll, or special pair chlorophyll (P680). The radical pair $P680^{+}Pheo_{D1}^{-}$ is far more stable than the initial radical pair. The lifetime of the $P680^{+}Pheo_{D1}^{-}$ radical pair has been estimated to be approximately 1 ps as opposed to only a few femtoseconds for the initial pair (Holzwarth et al. 2006). The increase in stability of the radical pairs as the process of charge separation proceeds is the main reason PSII can maintain a low activation energy for the process.

In spite of the fact that P680 is a dimer of two chlorophylls, spectroscopic evidence strongly suggests that the radical is 80% localized on the D1 side of the pigment (Rigby, Nugent, and Malleyl 1994).

The electron of $Pheo_{D1}^{-}$ is then transferred into Q_A to generate the radical pair $P680^{+}Q_A^{\cdot -}$. A variety of flash-induced absorption changes characteristic for transient populations of quinone radicals confirmed this charge-separated state (Schatz, Brock, and Holzwarth 1987). Kinetic studies on this process as well as curve-fitting of photovoltage measurements concluded times for the electron transfer between the pheophytin anion radical and quinone radicals to be 300-500ps (Leibl et al. 1989). The value of 300-500ps is strikingly similar to that of BRC (Arlt et al. 1993). The similarity should be expected since the electron transfer from pheophytin to quinone is rate determining in charge separation and hence should be conserved in all reaction centres. The significantly longer lifetime of $P680^{+}Q_A^{\cdot -}$ compared to the previous two states ensures the stability of the overall process by increasing the stability of the intermediates, a mechanism which is dominant in enzyme catalysis in general.

PSII complexes containing oxidized Q_A are referred to as “open centres” while those containing a reduced form or containing no Q_A are referred to as “closed centres” (Tyystjärvi, Hakala, and Sarvikas 2005). This nomenclature comes from the fact that open PSII complexes are the only ones capable of trapping excited state energies through the generation of an electrochemical potential difference. A change in the protein environment could accompany this step in charge separation.

Due to the stability of the $P680^{+}Q_A^{\cdot -}$ radical, the oxidation of TYR_Z by P680, creating a tyrosyl radical $TYR^{\cdot +}$ is energetically allowed. The tyrosyl radical is subsequently

reduced by the OEC complex which in its turn takes the electrons from water. Through such a process P680, in an indirect manner, is capable of oxidizing water, making it the strongest oxidant in nature (Barber 2003).

The reduction and oxidation which occurs between OEC,TYR_Z, and P680 is in the order of microseconds (Nugent, Ball, and Evans 2004) which is approximately the same time needed to move an electron from Q_A to Q_B , upon a reduction of Q_B and the consequent oxidation of the OEC, by P680 through TYR_Z, the OEC complex changes its S state to S_{n+1} (Siegbahn 2013).

Charge separation occurs again from the starting point at Chl_{D1} with Q_B negatively charged, the result of this second round is the further reduction of Q_B to Q_B^{2-} which subsequently takes two protons that come from the stromal side resulting in PQH_2. PQH_2 departs from PSII and goes to Cyt $_{b6f}$ delivering its two electrons, from Cyt $_{b6f}$ the electrons are used to replenish the P700 radical of PSI.

Two further rounds of charge separation result in the production of another PQH_2 and an S state of 4 for the OEC, which allows the OEC to perform water oxidation, releasing oxygen gas. During this entire process of electron transfers, protons are pumped to the lumen side creating a proton gradient, which is used to drive the synthesis of ATP.

Changes have been observed between dark and illuminated BRC using X-Ray crystallography where the Q_B head group is displaced by about 5 Angtroms and rotated by 180 degrees around the isoprenoid side chain (Stowell et al. 1997). Such structural

changes could arise from a conformational change in the binding pocket of Q_B that in turn can be accounted for through a change in the protonation states. Once Q_B becomes negatively charged, the same sequence of changes reoccurs starting with $Chl_{D1}^{+\cdot}Pheo_{D1}^{-\cdot}$. There is a "blockage" of charge separation until Q_B becomes negatively charged. The blocking of a second electron going through the charge separation process has been observed through fluorescence measurements, which point to pheophytin being the responsible species. This phenomenon is believed to occur through protein changes around pheophytin which render it incapable of accepting electrons during the state of $P680^{+\cdot}Q_A^{-\cdot}$ and the transfer of charge between Q_A and Q_B. The observation was made through fluorescence measurements (Yruela et al. 1994).

$Pheo_{D1}$, Q_A and Q_B are known as the acceptor side of PSII, since they accept electrons and create anions while OEC, TYR_Z, ChlD1 and P680 are known as the donor side of PSII since they donate electrons. At any step of charge separation, a reverse reaction is prone to occur; this reverse reaction is called charge recombination. In charge recombination, the anionic entity gives the electron back to the cationic entity recreating the two neutral pigments with one of them in the excited state. For example, when the $Chl_{D1}^{+\cdot}Pheo_{D1}^{-\cdot}$ radical pair recombines, it forms neutral pheophytin and an excited chlorophyll molecule on D1. In order to achieve the highest quantum yield possible, PSII has to minimize recombination and increase charge separation; such an optimization can be done through changes in the protein environment. The lifetime of a particular charged separated state may be dependent upon the amount of change to the protein's environment. The process of electron transfer which results in the creation of a charge

separated state is not long enough to allow for significant conformational changes to the protein's backbone. A change to the protonation state of the sidechains of ionizable amino acids has been suggested instead as a mode of stabilization of charge separated states.

1.5. MCCE (MultiConformer Continuum Electrostatics)

Change in the ionization states of amino acid sidechains is of chief importance in the shaping of protein conformation following a change in the electrostatic environment (Georgescu, Alexov, and Gunner 2002). Protonation states of amino acids in the context of this work refer to whether an ionizable side-chain has a proton or not. For example, Glutamic acid can be protonated or deprotonated (neutral or negative respectively). Whether an amino acid would be protonated or not depends on its pKa value. The pKa values for all amino acids have been determined experimentally by taking free amino acids in solution and performing titrations on them. The resulting pKa values, consequently, have no relation to the protein environment. Due to the fact that one cannot determine the experimental pKa of amino acid sidechains inside a protein for any reasonable system, a need arises to use computational methods to simulate a titration process on every titratable amino acid sidechain inside its protein environment. Several methods exist to determine the pKa values of amino acid sidechains in proteins, the most respected of which and most rigorous is known as MCCE (MultiConformer Continuum Electrostatics)(Forrest and Honig 2005). MCCE aims to achieve the theoretical titration of amino acid sidechains inside their protein environment using a Monte-Carlo approach which relates the conformational space to the electrostatic space (overall charge on the

amino acid's sidechain) (H. X. Zhou, Wlodek, and McCammon 1998). The MCCE algorithm can be divided into two parts: The first part finds all the possible conformers of sidechains through steric overlap considerations (Van Der Waals Radii not crashing into each other) along side all the different protonation states of sidechains, while the second performs Metropolis Monte-Carlo sampling to find a most probably conformation and protonation. With this dual approach of finding both conformers and ionization states, MCCE serves not only to determine the protonation states of titratable residues, but also their most likely geometry through a rigorous Monte-Carlo approach. Within this definition, a conformer is the result of rotation about a dihedral angle in an amino acid sidechain. Conformers are evaluated first using steric considerations and then using electrostatic considerations.

Monte-Carlo methods attempt to find a global minimum on the energy surface by considering random perturbations to the structure and evaluating the likelihood of each of these perturbations. Through random perturbations, Monte-Carlo methods not only find a global minimum on the energy surface but also explore the energy surface and provide a statistical analysis of the conformational space defined by the energy surface.

Metropolis Monte-Carlo can apply to a large variety of problems. Conformational searches are the chief application of Monte-Carlo methodologies in computational chemistry. In MCCE, Monte-Carlo is used to find a favourable combination of electrostatic and conformational space. This is done as a form of correction to pKa values of ionizable sidechains in aqueous solution readily obtained from titration experiments.

A generic acid (AH) in water would have the following equilibrium:

Scheme 3: $AH \rightleftharpoons A^- + H^+$

The equilibrium shown above in scheme 3 demonstrates the dissociation of the acid (AH) in solution, such a dissociation can be quantified using the pKa ($-\log K_a$) value where K_a is the equilibrium ratio as shown in scheme 4.

Equation 1: $$K_a = \frac{[A^-][H^+]}{AH}$$

pKa can also be expressed in terms of energy:

Equation 2: $$pKa = - \frac{\Delta G}{RT \ln(10)}$$

Where ΔG is the Gibbs free energy, R is the gas constant and T is the temperature in Kelvin. MCCE employs the thermodynamic cycle scheme shown in scheme 5 to compute the pKa and the protonation state of an amino acid within a protein. MCCE computes the shift due to protein by computing the desolvation energy and the electrostatic effect due to protein starting from the solvation energies in aqueous solution. Specifically, the ΔG rxn(prot) term is computed by MCCE through the thermodynamic cycle in scheme 5.

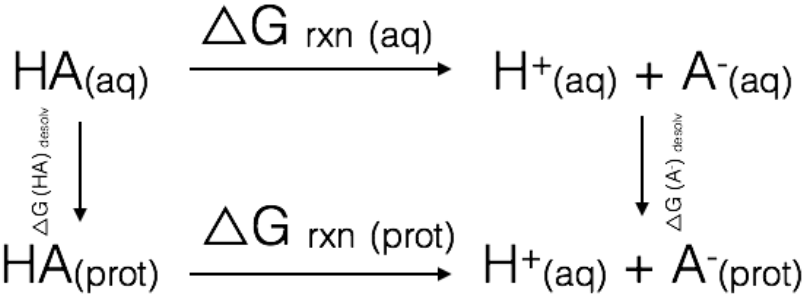

Scheme 5. Thermodynamic cycle of acid dissociation used by MCCE to compute the pKa and the protonation state of an amino acid within a protein. MCCE does this by computing the solvation Gibbs free energy (ΔG_{solv}) of the ionized and neutral species, along with Gibbs free energy of the ionization within the protein the $\Delta G_{rxn\ (prot)}$

The term shown as $\Delta G_{rxn\ (prot)}$ is in reality the sum of the solution Gibbs free energy with the shift due to protein. In order to fully account for the protein shift the pairwise Gibbs free energy has to be taken into account. The electrostatic and the Lennard-Jones pairwise energies that describe how each residue interacts with its surrounding in both ionized and neutral state are included. These energies are all computed using the sum of microstates resulting from the Monte-Carlo sampling process.

Independent Monte-Carlo simulations are carried out at variable pH or E_h values providing a Boltzman distribution of residue ionization and conformation states. The occupancy of the ionized form is calculated assuming a single site of titration with a variable Hill coefficient (n) through the equation 3.

Equation 3: $$< Occ_{ionized} >= \frac{10^{-mn(pH-pK_a)}}{1+10^{-mn(pH-pKa)}}$$

Where m represents the probability for an acid to have a charge of -1 or +1 for base, it is -1 for acidic residues and 1 for basic residues.

These occupancy values can indicate changes to the electrostatic environment due to the process of charge separation in Photosystem II. This data is presented in **Chapter 2**, once the protonation states are collected, the implications on the flow of waters within Photosystem II (an issue of interest to our research group), is presented in **Chapter 3**. Essentially, through the computation of the interactions of the residues with each other, and their respective solvation energies one can arrive to the shift to pKa that can be experienced due to the protein environment. Similarly, the redox potential, Em, can be computed. The redox potential of P680 radical which one would aim to reproduce in an artificial reaction centre that can mimic PSII is presented in **Chapter 2**. In **Chapter 4**, the same computation is done on an artificial 'reaction centre' to compare its oxidation potential to that of P680. It was this data that guided the design of our own 'reaction centre' which amed to reverse-engineer PSII's redox reactions in a stable and easily produced *E. coli* protein scaffold.

1.6. CHOICE OF PIGMENTS FOR ARTIFICIAL 'REACTION CENTRE'

As *E. coli* has no proteins that can bind chlorophyll *a* with its long tail, analogues of chlorophyll should be used instead. Two main factors need to be considered: the absorption and how easily oxidized or reduced a pigment is. Chlorophylls, the pigments employed in natural photosystems, are oxophorbines. Oxophorbines are chlorins that contain a 13^1 keto group and the phorbine isocyclic ring spanning positions 13 and 15.

Various Zinc chlorins have been synthesiszed as analogues of chlorophyll (Kee et al. 2007), some are presented below in figure 1.4.

Porphyrins, which contain an unsaturated macrocycle, compared to chlorins, tend to be harder to oxidize than chlorins, while the absorption to the first excited singlet state tends to be of higher energy with lower oxcillator strength.

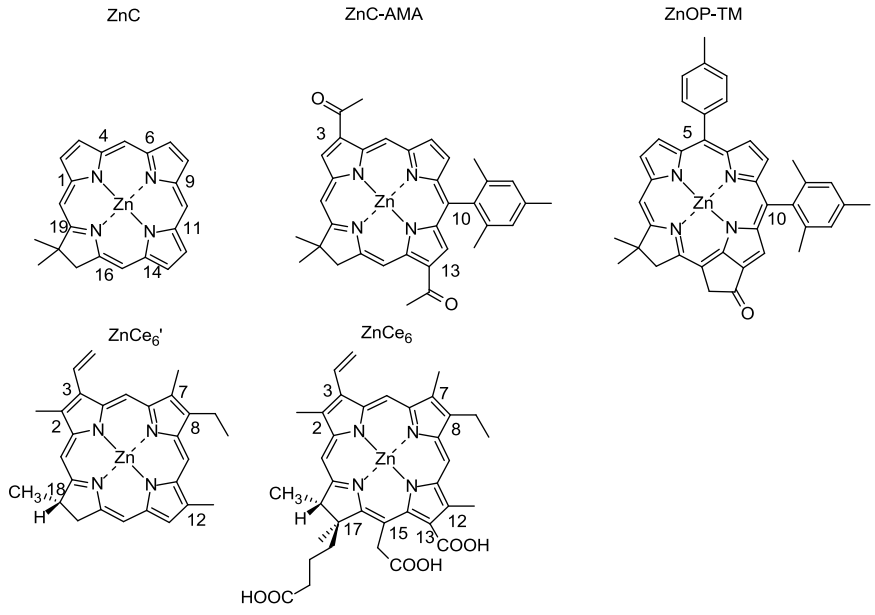

Figure 1.4. Zn - chlorin derivatives used for computation of electrochemical properties. C - chlorin, OP - oxophorbine, A -acetyl, M - mesityl, T - tosyl.

The excitation energy levels and the oxidation potentials are influenced by the saturation of the pyrrole ring.

Porphyrins have been employed as mimics of chlorophylls. The structural diversity of porphyrins, especially relating to the central metal atom has given them a very wide range of redox potentials. While Zinc chlorins have oxidation potentials ranging from 400mV to 800mV vs. NHE in acetonitrile, Phosphorous porphyrins exhibit much higher oxidation potentials due to the high oxidation state of the Phosphorous atom (V state). At this oxidation state, the central Phosphorous atom carries a positive charge of +1. Additionally, the smaller size of the Phosphorous atom causes the ring to pucker towards a "horse saddle" geometry, destabilizing the cationic radical. Due to factors mentioned above, the first oxidation potential of many Phosphorous porphyrin pigments is in excess of 1V, while some exceed 2V. Variation of oxidation potential is determined by the electron density of the macrocycle, which in turn is determined by the substituent groups on the pyrrole rings. For example, addition of electron withdrawing groups such as Fluorine increases the oxidation potential as they make the macrocycle more electron deficient. On the other hand, alkyl groups that act as electron donating to the ring decrease the oxidation potential. Axial ligands to the Phosphorous do not seem to influence the oxidation potential (Akiba et al. 2001).

Within a photochemistry context, Phosphorous porphyrins are able to act as electron acceptors or donors. Generally, Phosphorous porphyrins would abstract an electron from aromatic groups nearby to become the neutral radical. This electron transfer is stabilized

by the loss of charge on the Phosphorous porphyrin. This neutral radical form is stable, allowing Phosphorous porphyrins to be paired as part of dyads and triads with electron-rich aromatic donors with long lifetimes of charged separated states. Such stabilization of the radical pairs allows detailed examination using techniques such as transient EPR (Poddutoori et al. 2010).

In this work, a theoretical explanation of the oxidation potential of P680 within Photosystem II will be obtained using MCCE. This theoretical model will also be used to track protonation state changes as the charge separation process proceeds (**Chapter 2**). The protonation state changes within the protein as charge separation proceeds can be linked to regulation of Photosystem II's function, of particular interest if the access of water to the inside of the relatively hydrophobic PSII complex, the investigation of the effect of protonation states on access of water to PSII is also considered (**Chapter 3**). The MCCE method, along with experimental methods will then be used to determine the oxidation potential of a Zinc chlorin molecule inside an artificial 'reaction centre' based on the Bacterioferritin protein scaffold (**Chapter 4**). Based on those results a new generation of artificial 'reaction centres' will be proposed and experimentally examined (**Chapter 5**). Finally, the future direction of this research area will be discussed and outlined (**Chapter 6)**.

Chapter 2

Oxidation potential calculations of P680 of Photosystem II and tracking of the protein's electrostatic response to charge separation

2.1. ABSTRACT

What contributes to making the oxidation potential of P680 the highest in nature? What is the electrostatic response to the progressive placement of charges resulting from the radical chemistry of charge separation? Does this electrostatic reaction help control the functions of Photosystem II? Such questions are important background information towards the design of an artificial Photosystem II which could provide a means of extracting electrons from water to build chemical bonds of fuel. This chapter uses a computational model known as MultiConformer Continuum Electrostatics to answer these questions and compare them to previous works. The aim is to gain insight into how does Photosystem II control the oxidation potential of P680 in order to use that information towards the development of artificial photosystems that might mimic the reactions of PSII.

2.2. INTRODUCTION

Photosystem II is the redox active pigment–protein complex embedded in the thylakoid membrane that catalyses oxidation of water and reduction of plastoquinone in oxygenic photosynthesis. This catalytic function is performed by light driven electron transfer reactions through redox cofactors of the PSII reaction center. The PSII core complex is a large multisubunit membrane protein complex molecules (Barber 2003). Light energy absorbed by one of the PSII pigment molecules is used to initiate a sequence of electron transfer steps leading to formation of a stable radical pair.

The electron transfer reaction cycle starts with charge separation between the monomeric "accessory" D1 chlorophyll (Chl_{D1}) and D1 pheophytin (Pheo). After this event P680 is oxidized by Chl_{D1}^{+} with the rate of $(7.7\ ps)^{-1}$ and the secondary radical pair, $P680^{+}Pheo^{-}$, is formed. Next, electron transfer from $Pheo^{-}$ to Q_A occurs with a much slower rate constant of $(175\ ps)^{-1}$(Dekker and Van Grondelle 2000). $P680^{+}$, which has very high redox potential, oxidizes a tyrosine residue of the D1 protein (Y_Z) on a nanosecond time scale while Q_A reduces the second quinone associated with the D1 polypeptide (Q_B) in approximately 300-500 μs (Cardona et al. 2012). In a second photochemical cycle, Q_B becomes doubly reduced and protonated to become plastoquinol (PQH_2). While Q_A is a firmly bound one-electron acceptor, Q_B leaves the binding site after forming the quinol (Q_BH_2) state (Barber 2003). Q_A oxidation by Q_B has a halftime of 150-250μs, while Q_A oxidation by the semiquinone Q_B proceeds with a halftime of 400-600 μs (Cardona et al. 2012).

The protein scaffolding, consisting primarily of the entwined D1 and D2 polypeptides, CP47, CP43 and $Cytb_{559}$, holds the PSII cofactors in their proper positions and orientations. The transmembrane nature of these peptides means that they can be quite hydrophobic which can increase the oxidation potential of P680 and other cofactors. Additionally, the long alpha helices of the peptides can create an effect from the backbone on the redox potential of cofactors. The backbone contribution to the redox potential is a polarization effect. The amide part of the backbone has a dipole which can be oriented through secondary structure to exercise a stabilizing or destabilizing effect on buried charges.

PSII polypeptides also contain ionized and polar residues, essential for protein stability and function. The protein interacts with the embedded cofactors to modify their electronic properties by electrostatic and steric interactions, hydrogen binding, etc. PSII is a protein where electrostatic forces play important functional roles. Light driven formation of the radical pair and subsequent electron transfer reactions in PSII affect the distribution of charge inside the protein. Polar groups and waters rearrange to stabilize the radical pairs throughout the reaction cycle. Thus, the PSII protein not only statically modifies electronic properties of cofactors, it does so in a dynamic manner in response to electron transport. Changes of charge distribution of the cofactors are expected to modify the ionization pattern of the protein along the reaction cycle. These changes may facilitate the process of photochemistry. They may be essential for regulatory feedback mechanisms. It has been suggested that the charge separation - induced processes lead to conformational changes of the protein environment which in turn modulates energy and

electron transfer processes (Ishikita et al. 2005). Computational studies of conformation changes related to charge separation and electron transfer processes can provide insights into mechanisms of these reactions. Knowledge of the protonation pattern in the different charge states in PSII is essential for such simulations.

Computation of protonation patterns and driving forces of electron transfer reactions in PSII are of great interest and have been subject of several theoretical studies (Saito, Rutherford, and Ishikita 2013; Ishikita and Knapp 2005; Siegbahn and Blomberg 2004; Siegbahn 2013). The protonation states will be computed with respect to the various charge separation steps.

The calculation of protonation states of all of the titratable aminoacids in PSII in its different charge states is a computationally intensive task, which had not yet been done. It is an important calculation because protonation changes are caused by long-range electrostatic forces, and they can propagate through the protein. Important protonation changes may occur far from the sites of electron transfer reactions. Results of the calculations revealed a number of interesting changes in protonation states that are correlated with electron transfer reactions. The study forms the basis for future computational studies of protein dynamics and structural changes occurring in charge separation and electron transfer reactions using MD and QM.

2.3. METHODS

2.3.1. Atomic coordinates

The 3ARC PSII structure from the Protein Data Bank was used to calculate the redox potential and the protonation state changes. The structure is at a 1.9 Å resolution making it of high quality and detailed.

2.3.2. Partial atomic charges

Partial atomic charges of cofactors (Pheo*a* and Chl*a*) in different ionization states were obtained by a restrained electrostatic potential fit using RESP program from AMBER8 (UCSF, San-Francisco, CA) suite as described (Cornell et al. 1995). Atomic charges of the oxygen evolving manganese cluster were assigned according to the redox state of its atoms in the dark adapted (S_1) state as follows: Mn1-Mn3: +3, Mn4: +2; O1-O4: -2, Ca: +2. Atomic charge of non-heme iron +2.

2.3.3. Computation of redox potential of cofactors and protonation states of amino acids in the reaction centre of Photosystem II

MCCE2.5 (Song, Mao, and Gunner 2009) was used to predict the ionization state of each cofactors as a function of E_h (applied reduction potential) while the protonation states patterns of amino acids were computed similarly as a function of pH (see introduction for more information on the MCCE algorithm). The computation of ionization states of

titratable residues and cofactors in the protein was based on the electrostatic continuum model in which the Poisson-Boltzmann equation is solved by the program DelPhi (Li et al. 2012). For each titratable amino acid, an ensemble of conformation states was sampled by the MCCE program to determine the equilibrium distribution of position and ionization state of the side chain and ligands (Georgescu, Alexov, and Gunner 2002). MCCE was used to calculate the Boltzmann distribution of residue side chain position and ionizations state in PSII structures in several charge separation states. As part of the algorithm, waters that have a higher solvent accessibility than 30% are deleted and an ε=80 is placed in their place. All titratable residues of the protein were sampled.

PSII is an integral membrane complex surrounded by low dielectric lipid bilayer and high dielectric water. To model the native lipid/water protein environment, essential for continuum electrostatic calculations, the entire PSII core complex was placed into a pre-equilibrated lipid bilayer composed of monogalactosyldiacylglycerol (MGDG), digalactosyldiacylglycerol (DGDG) and phosphatidylglycerol (PG) with 18:3 and 16:0 fatty acids. The lipid bilayer components were chosen to represent the most abundant lipids and fatty acids found in photosystem II preparations in an approximately correct proportion. The initial coordinates of the lipid bilayer were taken from our previous MD study of PSII core complex. Then lipids were relaxed using AMBER99 molecular mechanics force field. Protein and cofactors were frozen during relaxation.

2.4. RESULTS

2.4.1. Redox potentials of P680 and Pheophytin D1

The oxidation potential of P680 matches the reported range of 1.2-1.4V (K. Hasegawa and Noguchi 2005). Two main factors are seen to contribute to the high oxidation potential of P680: desolvation and backbone. Desolvation is affected by the hydrophobicity of the region the pigment is found in. In other words the desolvation energy contribution is explained in terms of how unfavorable is the appearance of a charged species in a hydrophobic environment. Shifts due to the backbone, sidechains and specific shift due to the OEC are also presented in table 2.1.

Table 2.1. Redox potentials computed using MCCE of P680 (PD1 and PD2) and the Pheophytin $_{D1}$ (Pheo $_{D1}$). Contributions to the shift of the redox potential are shown divided into desolvation contribution (ΔG_{desvol}), backbone contribution (ΔG_{bkn}), contribution from amino acid sidechains (ΔG_{res}), and finally contribution from the Oxygen Evolving Complex (ΔG_{OEC})

	$E_{m(sol)}$	$\Delta\Delta G_{desolv}$	ΔG_{bkbn}	ΔG_{TOTAL}	ΔG_{res}	ΔG_{OEC}	E_m^{mfe}
PD1	0.73	0.17	0.18	0.61	0.26	0.27	1.34
PD2	0.73	0.23	0.14	0.56	0.19	0.13	1.29
$Pheo_{D1}$	-0.62	0.25	-0.08	0.03	-0.14	-0.11	-0.59

* Redox potentials computed at pH=7.0

The internal dipole of the protein in the MCCE calculations is assumed to be 4, while the solution dielectric constant is that of water, ε=80. As the amino acids surrounding P680 are not solvent exposed, the ΔG associated with removal of the pigment from ε=80 to ε=4 is high. Previous calculations have attempted to explain the high oxidation potential of P680 purely in terms of dielectric constant. The use of Density Functional Theory (DFT) along with a continuum solvation model demonstrated the dependence of the oxidation of chlorophyll on dielectric constant (K. Hasegawa and Noguchi 2005). This model ignores the dipole effect of the backbone surrounding the pigment. Our calculations demonstrate that the backbone contributes as well as the dielectric constant of the hydrophobic binding site of P680. P680 is a dimeric pigment as with special pairs of other reaction centres. PD1 is the chlorophyll on the D1 protein side and PD2 is the chlorophyll on the D2 side. Previous computational work, as well as experimental work suggested that PD1 should have the higher potential(Ishikita et al. 2005). Our calculations agree with previous work in this respect. This higher potential of PD1 is due to the backbone contribution and the OEC contribution. The effect of the OEC is higher on the PD1 than on the PD2. This is due to orientation of the PD1 pigment with respect to the OEC.

Previously, computations aiming to estimate the shift due to protein to the chlorophylls of PD1 and PD2 utilized Chlorophyll a in DMF (Dimethylformamide) as a reference due to lack of experimental values in aqueous solution (Ishikita et al. 2005). DFT calculations indicate that the oxidation potential of chlorophyll is approximately 80mV higher in DMF than in aqueous solutions (K. Hasegawa and Noguchi 2005). We are able to

produce similar results by using the aqueous solution value estimated by DFT calculations (K. Hasegawa and Noguchi 2005). This is likely the result of the higher quality X-Ray structure used in this study as opposed to the previous work (Ishikita et al. 2005). In fact, when oxidation potential calculations were performed for the first time by our group using the lower resolution 2AXT structure, the DMF value of 0.83V was used as a reference and produced similar results to the work by Ishikita. The differences in the contributions between the work done on the 2AXT structure and this work are predominantly in the residues contributions due to the new placement of various amino acid sidechains.

The oxidation potential of $Pheo_{D1}$ was also determined in the same manner as P680. $Pheo_{D1}$ is the primary electron acceptor. Experiments were conducted to determine its redox potential. Because the redox potential of P680 is too high to be determined directly, the values available in literature of P680 oxidation are derived from the redox potential of $Pheo_{D1}$(Tyystjärvi, Hakala, and Sarvikas 2005). The values obtained for $Pheo_{D1}$'s reduction potential depend on the experimental conditions. In particular, it was found that the use of betadine upshifts the reduction value. Our theoretical value agrees very well with the experimental value of -0.589V (Allakhverdiev et al. 2010). As with the P680, the OEC has an influence on this value. The fact that the OEC affects the redox potential of $Pheo_{D1}$ by making it more negative has been known from experimental results from Mn-depleted PSII preparations (Allakhverdiev et al. 2010).

An interesting realization arises from the observations that both P680 and $Pheo_{D1}$ are affected by the OEC: in tuning redox potential of possibly water-oxidizing artificial 'reaction centre' the effect of the metal cluster itself has to be taken into consideration. By testing the MCCE method's ability to reproduce this dependency on the well-understood system of PSII, one can hope to be able to use it to decide how to tune the redox potentials within artificial reaction centres. An example of using the MCCE method to understand how a Manganese cluster affects the pigment within an artificial reaction centre is given in **Chapter 4**.

2.4.2. Protonation state changes during charge separation

The ionization states of all titratable residues were calculated at pH=7 for six intermediate steps of electron transport, representing a cycle of electron transport from photoactive RC pigment to Q_B. The six charge states are described in detail in table 1. Ionization states of titratable residues are shown in **APPENDIX I**. Table 2 shows the cumulative effect of the various amino acids changing protonation states. This representation is useful in establishing that even though there may be many amino acids changing protonation states as charge separation proceeds, the changes tend to cancel each other and hence establish a buffering effect. Figure 2.1 shows the different amino acids changing protonation states. The majority of them are found around the plastoquinone sites (for Q_A and Q_B). It is note-worthy that table 2 shows the highest overall charge difference. This is expected since the plastoquinone-tyr radical pair has a

negative charge that is unbalanced unlike the other stages since the tyrosine radical is formed through a proton-coupled electron transfer (PCET) mechanism (Ishikita and Knapp 2006) resulting in a neutral tyrosyl radical. Tyrosine radicals do not necessarily have to be formed through a PCET mechanism. For example, **Chapter 4** gives an example of a tyrosyl radical formation that is likely to result in a positively charged tyrosine.

We found 29 residues changing ionization states in the charge separation cycle (Table 2.2). As expected, most of the changes occurred in the D1 subunit responsible for binding most of the cofactors of the active branch of electron transport.

The changes in the protonation states of residues constitute an electrostatic response of the protein to the placement of charges on cofactors upon photoinduced radical formation. Figure 2.1 shows the sites of protonation state changes that accompany charge separation.

Table 2.2. Description of the charge states of PSII RC used for calculation of ionization states.

#	TYR_Z	*P680*	Chl_{acc}	*Pheo*	Q_A	Q_B
1	0	0	0	0	0	0
2	0	0	+1	-1	0	0
3	0	+1	0	-1	0	0
4	0	+1	0	0	-1	0
5	$Y^{\cdot}$	0	0	0	0	-1
6	0	+1	0	-1	0	-1

Table 2.3. The absolute cumulative difference in charge changes with respect to stages of charge separation as an indication to the overall protonation state changes of titratable amino acids in Photosystem II

Stages	Δ2-1	Δ3–2	Δ4–3	Δ5–4	Δ6–5
Cumulative charge	0.2	0	0.04	0.8	0.4

Many of the protonation state changes act to counteract the charge of the radical, in essence creating salt-bridges between the photoinduced radical cations or anions and amino acids. These salt bridges cause shorter distances between the cofactor and the amino acid sidechains. This model could possibly help explain the electrostriction observation in photoacoustic measurements of Photosystem II (Hou and Mauzerall 2011), especially that the most dramatic change in volume observed is associated with the PQ radical. As seen in figure 2.1, this is the region where the majority of protonation state changes occur.

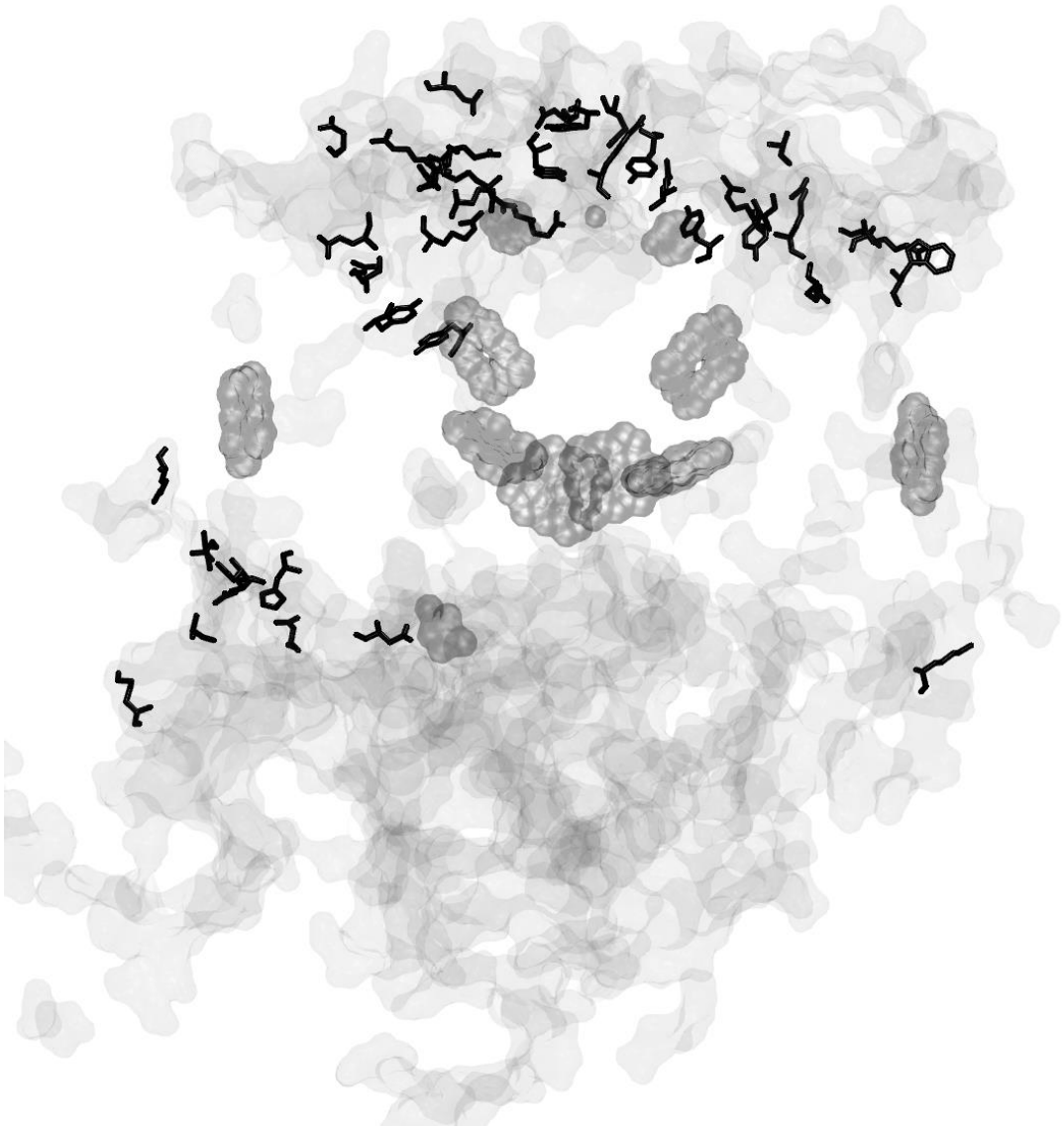

Figure 2.1. Sites of protonation state changes happening through all the stages of charge separation indicated in table 1. Amino acids shown in black licorice change charge by more than 0.5 as indicated by the MCCE Monte-Carlo sampling at pH of 7

2.5. CONCLUSION

This chapter aimed at calculating the redox potential of P680 and $Pheo_{D1}$, results of both agree well with experimental work and computational work. It was found that the new structure with the higher resolution allows one to arrive at an oxidation of P680 using the reference in water and not in DMF. In both cases of P680 and $Pheo_{D1}$, the OEC was found to contribute to the shift due to protein. Protonation states changes were determined with respect to charge separation. It was expected to see that the protonation states respond to radical pairs during charge separation in PSII. These changes acted as counterions to the radical ions charges. A larger amount of counter charge was found with respect to steps of charge separation in which the plastoquinones are involved, likely due to the fact that the radical pair involves one neutral species (tyrosine). A question of interest is: are these protonation states necessary for the entry of water into the relatively hydrophobic site of OEC in PSII. In order to examine that possibility, molecular dynamics simulations were done on PSII and water channels were examined to see if access to the OEC is tightly controlled.

Chapter 3

A river runs through it! Access of water within Photosystem II

This chapter has been published in Biochemistry Journal

S. Vassiliev, P. Comte, **A. Mahboob**, and D. Bruce Biochemistry 49(9):1873-81 **(2010)** "Tracking the flow of water through photosystem II using molecular dynamics and streamline tracing"

*Contribution to paper was with regards to parameterizing cofactors and preparation of structure

3.1. ABSTRACT

The $CaMn_4$ cluster of the oxygen-evolving complex (OEC) of photosynthesis catalyzes the light- driven splitting of water into molecular oxygen, protons, and electrons. The OEC is buried within photosystem II (PSII), a multisubunit integral membrane protein complex, and water must find its way to the $CaMn_4$ cluster by moving through protein. Channels for water entrance, and proton and oxygen exit, have previously been proposed following the analysis of cavities found within X-ray structures of PSII. However, these analyses do not account for the dynamic motion of proteins and cannot track the movement of water within PSII. To study water dynamics in PSII, we performed molecular dynamics simulations and developed a novel approach for the visualization of water diffusion within protein based on a streamline tracing algorithm used in fluid dynamics and diffusion tensor imaging. We identified a system of branching pathways of water diffusion in PSII leading to the OEC that connect to a number of distinct entrance points on the lumenal surface. We observed transient changes in the connections between channels and entrance points that served to moderate both the flow of water near the OEC and the exchange of water inside and outside of the protein. Water flow was significantly altered in simulations lacking the OEC which were characterized by a simpler and wider channel with only two openings, consistent with the creation of an ion channel that allows entry of Mn^{2+}, Ca^{2+}, and Cl^{-} as required for construction of the $CaMn_4$ cluster.

3.2. INTRODUCTION

Photosystem II is the redox active pigment–protein complex embedded in the thylakoid membrane that catalyzes oxidation of water and reduction of plastoquinone in oxygenic photosynthesis. This catalytic function is performed by light driven electron transfer reactions through redox cofactors of the PSII reaction center. The PSII core complex is a large multisubunit membrane protein complex molecules(Barber 2003). Light energy absorbed by one of the PSII pigment molecules is used to initiate a sequence of electron transfer steps leading to formation of a stable radical pair.

The oxidation of water to O_2 requires an extremely strong oxidant and is prone to side reactions resulting in the formation of reactive oxygen species. The OEC is surrounded by a hydro- phobic pocket and buried deep in the protein to prevent excessive access of water and solute to the catalytic site(Wydrzynski, Hillier, and Messinger 1996). The restricted access of large competitive water analogues to the water splitting reaction first led to the proposal that the site of water oxidation was protected by the protein (Radmer and Ollinger 1983). Subsequent studies confirmed this idea by showing that perturbation of the protein, via release of extrinsic PSII polypeptides, resulted in the formation of H_2O_2 at the expense of $O2$ evolution, a condition reversed by the addition of kosmotropic solutes that promote protein aggregation(Wydrzynski, Hillier, and Messinger 1996). Kosmotropic solutions contribute to protein aggregation by stabilizing water-water interactions. Access to the OEC was probed in an ESEEM (Electron Spin Echo Envelope Modulation) study that showed the level of binding of alcohols to the $CaMn_4$ cluster decreased with the increasing size of the alcohol molecule, leading the

authors to suggest the presence of a water channel(Force et al. 1998). As O_2 and protons are released from the same catalytic site, channels for the exit of both have also been suggested (Anderson and Chow 2002; Wraight 2006). With requirements for three potentially independent channels, the "plumbing" of PSII appears to be complex. Additional complexity arises during the assembly or repair of PSII. Insertion of the $CaMn_4$ cluster occurs after protein assembly and thus requires the presence of an ion channel to facilitate the movement of Mn^{2+}, Ca^{2+}, and Cl^{-} ions through the protein to the site of the OEC. A search for channels became possible after publication of crystal structures of the PSII core complex (Ferreira et al. 2004; Loll et al. 2005). The "Caver" program was used to search for connecting cavities that might form channels within the structure of Protein Data Bank (PDB) entry 1S5L(Murray and Barber 2007). Three channels were found. The widest and the least hydrophilic (i) was suggested to be for oxygen. A more polar channel (ii) was assigned to water and protons, and the most polar channel (iii) was designated for protons alone. Note that the Caver algorithm searches for the shortest pathways of a chosen minimal diameter from a given point inside the protein to the surface. The application of this program thus biases the search for channels toward a set of round "pipelines". Later, a comprehensive identification of all cavities near the OEC in the structure of PDB entry 2AXT, regardless of whether they connected to the surface, revealed a complex system of potential channels(Ho and Styring 2008). The approach taken in that work was a step forward in understanding how water is carried to the active site as it revealed a complex interconnected network of water pores and cavities inside the PSII protein.

The most recent structure of PSII (PDB entry 3bz1) was again analyzed with Caver

(Guskov et al. 2009; Gabdulkhakov et al. 2009) which generated a system of eight channels originating at the OEC that merged into six exits on the lumenal side of PSII. The largest channels were in positions similar to those of the "water channels" found in earlier studies. A number of "new" channels with smaller minimum diameters were also identified, and on the basis of their size and the placement of hydrophilic residues, they were assigned as proton channels.

To date, efforts to identify water channels within PSII have been based on the analysis of cavities within X-ray structures. There are two problems with this approach.

(1) The existence of a cavity in a crystallographic structure does not necessarily mean that it is occupied by water. Placing explicit water molecules and assessing their potential is the way to solve this problem. Such an approach was used in a DFT-QM/MM study of OEC, which identified a chain of hydrogen-bonded water molecules approaching the $CaMn_4$ cluster along two distinct pathways (Sproviero et al. 2008). This study, however, was limited by the inclusion of only a small protein area adjacent to the active site of water splitting.

(2) Channels in static structures have fixed boundaries and a rigid "brick wall" lining(Murray and Barber 2007). This is an unrealistic picture as proteins and the channels within them are dynamic at physiological temperatures. Thermal motions of the protein will continuously modify channel networks and may lead to transient opening and closing of some pores (Cohen et al. 2005). These processes may be critical in controlling the movement of water with the

protein. Dynamic simulations of water diffusion are essential to the understanding of water channels and water movement in PSII (Ho 2008).

Dynamic simulations of water diffusion pathways have been limited to proteins in which well-defined channels with relatively simple geometry have been identified, such as aquaporins (Zhu, Tajkhorshid, and Schulten 2001; de Groot et al. 2003) and lysozyme crystals (Hu, Jiang, and Sandler 2008; Hu and Jiang 2008). In cases like these, standard simulation analysis methods, including radial distribution functions, mean square displacement, and calculation of solvent density along the direction of the channel, are sufficient. However, large protein systems, like PSII, often have multiple nanopores with complex shapes, different sizes, interconnections, and branch points. Dynamics of water may be further complicated by formation of transient nanopores. For such systems, identification of the most probable pathways from the active site to the bulk solvent becomes a major problem.

Unlike previous static cavity searches, in this work we have identified energetically favorable locations for water molecules in all cavities of PSII protein and placed explicit water molecules within them. We then simulated motion of the whole PSII core complex, including water at physiological temperature, and, finally, developed a novel way of looking at the movement of water into and through proteins. Our streamline tracing approach was used to map the patterns of equilibrium water flow within PSII. We identified a network of dynamic water channels leading to and controlling the flow of water to the OEC. In addition, our simulation of PSII in the absence of the OEC revealed

the formation of a shorter and wider channel consistent with the movement of metal ions into the active site required for assembly of the $CaMn_4$ cluster.

3.3. METHODS

3.3.1. Molecular Dynamics Simulations

Our MD simulations were similar to that described in (Vasil'ev and Bruce 2006) with the following changes. The current simulation was based on the 2AXT X-ray structure of the PSII core complex with the unassigned subunit X removed. Waters were added suing the DOWSER program (Zhang and Hermans 1996). The protocol used by DOWSER was to place water in internal cavities, to relax them to minimize their interaction energy, and finally to select and retain only water molecules with energies of less than -12 kcal/mol (Zhang and Hermans 1996). The threshold was used as it reproduced X-ray structure waters. The MD simulations were conducted with NAMD (Kal et al. 1999) and performed with periodic boundary conditions at a constant pressure (1 atm) and temperature (300 K) using Langevin dynamics with Nose-Hoover Langevin piston pressure control. The long-range electrostatic interactions were calculated using the particle mesh Ewald algorithm. Both the electrostatic and the Lennard-Jones interactions had a twin-range cutoff of 10-12 Å. The AMBER-1999 force field (Wang, Cieplak, and Kollman 2000) with modification of the φ and ψ dihedral parameters as described in (Simmerling, Strockbine, and Roitberg 2002) was used for protein, and the GLYCAM-2000a force field (Basma et al. 2001) was used for the headgroups of galactolipids. The force field for cofactors was based on the parameters described previously (Vasil'ev and

Bruce 2006). The geometry and partial atomic charges of the OEC were taken from the QM- refined model of the OEC and its ligands in the S1 state described in (Sproviero et al. 2007). After an initial equilibration period of 2 ns during which the protein backbone and heavy atoms of all cofactors were constrained to their initial X-ray positions and side chains were allowed to relax, all constraints were removed and a 10 ns production run was performed. The whole system, including the PSII complex, the membrane patch, and TIP3P water, contained 320000 atoms; its size was 183 Å x 132 Å x 132 Å. TIP3P water model allows for interaction with the lone pair with the water molecule.

3.3.2. Tracking of water movement within PSII

To identify channels we designed a tool to find areas characterized by a highly anisotropic motion of water, "streams". We implemented a streamlining technique, "fiber tracking" originating from fluid dynamics. This technique is used in MRI imaging to measure the location, orientation, and anisotropy of water tracts in soft fibrous tissues (Le Bihan et al. 1986; Basser et al. 2000). Fiber tracking is based on determination of the velocity field and subsequent calculation of the motion of particle in it. To implement this technique, time-averaged 3D direction field data must be extracted from the dynamics simulation by determination of a diffusion tensor. To calculate the tensor field we divide the simulation system volume into n small cubic elements (voxels) with a volume of about 1 $Å^3$ each.

For all voxels containing a water molecule at time t we find the position of this water molecule at time (t+**Δ**t) and calculate the tensor elements according to the Einstein

relation:

$$T^{\alpha\beta} = \frac{\langle[\alpha(t+\Delta t)-\alpha(t)]\rangle \bullet \langle[\beta(t+\Delta t)-\beta(t)]\rangle}{2\Delta t}$$

Where $ab = \{x, y, z\}$

Tensor elements are averaged over the time window of the MD run and the diffusion tensor is diagonalized to find the direction of fastest motion:

$$T = \{v_1, v_2, v_3\} \begin{pmatrix} \lambda_1 & 0 & 0 \\ 0 & \lambda_2 & 0 \\ 0 & 0 & \lambda_3 \end{pmatrix} \{v_1, v_2, v_3\}^T$$

Eigenvalue λ_i of the diffusion tensor describes the diffusion rate along the direction of the corresponding eigenvector $\mathbf{v}_i$. Channels (fibers) are characterized by anisotropic linear diffusion ($\lambda_1 > \lambda_2 \cong \lambda_3$). The eigenvector associated with the largest eigenvalue of the diffusion tensor is parallel to the local channel direction (de Groot et al. 2003). Therefore, the vector tangent to the trajectory at point s is equal to the eigenvector calculated at this point, and the channel trajectory is described by a system of three differential equations:

$$\frac{d\mathbf{r}}{ds} = \mathbf{v}_1(\mathbf{r}(s))$$

To track a channel we solve the system numerically for an initial condition which specifies a starting point: $\mathbf{r}(0) = \mathbf{r}_0$. Solution of this system of differential equations requires a continuous and smooth direction field. Due to a limited time frame in molecular dynamics simulations, the diffusion tensor data is discrete, noisy and coarsely sampled. To perform reliable and robust fiber tracking we generated a continuous smooth presentation of the direction field using a trilinear interpolation on the tensor matrix

elements (Basser et al. 2000) and implemented a moving least squares filter which approximates data locally with a low degree polynomial considering location, orientation and history of motion (Zhukov and Barr 2002). To find all channels originating in a region of interest we first identify "seed points", voxels with high linear anisotropy: $\mathbf{c}(\mathbf{x}, \mathbf{y}, \mathbf{z}) = (\lambda_1 - \lambda_2) / (\lambda_1 + \lambda_2 + \lambda_3)$. We then integrate the streamline from each of the seed point in both directions. We stop tracking the streamline if its length exceeds an allowed length; if anisotropy or diffusion rate becomes smaller than the allowed minimums or if streamline turns at an acute angle.

3.4. RESULTS

3.4.1 Placement of waters inside Photosystem II

We found more than 900 water molecules buried inside protein subunits (Figure 3.1A). Most of the internal water molecules were located in the area of the "large channel system" as described in (Ho and Styring 2008). Initial water placement suggested multiple potential water entrance points and multiple potential pathways to the OEC. To understand the nature of the interaction between the OEC and its surrounding proteins, to facilitate the investigation of mechanisms responsible for controlling the access of water to the OEC and to test our method for detecting equilibrium water streams we performed two simulations of the PSII core complex. In one simulation the OEC was present and in the other it was removed. During the assembly of PSII, or its repair after photoinhibition, the $CaMn_4$ cluster is inserted after the polypeptides are assembled. The OEC-less simulation was done to shed light on the patterns of water diffusion in the interior of PSII

before/during construction of the OEC, especially with respect to the delivery of metal ions to the active site. Each system was simulated for 10 ns after an initial 2 ns equilibration. During the simulations we observed equilibrium motion of water across the protein/water interface at multiple entrance points as well as water motion inside the protein (Figure 3.1B, C). Trajectories of motion of several representative water molecules are shown in figure 3.1B to illustrate the different mobilities of water molecules in different parts of the PSII protein. Identification of time averaged structures for all of the nanopores inside PSII cannot be easily achieved in this large and complex system containing many hundreds of interior water molecules.

3.4.2 Water streams within Photosystem II

Computed water streamlines were found in spaces free of protein backbone atoms and in most cases free of all protein heavy atoms (Figure 3.1D). Some streams were found in areas transiently occupied by protein sidechains. Inside PSII, streamlines formed a complex network of interconnected channels leading from the surface of the protein to the buried OEC. In general we found the streamline system to be located in the same regions as the cavities found previously in analyses of the static structure (Murray and Barber 2007; Ho and Styring 2008). Motion of individual water molecules matched the streamline direction, but also showed some random deviations, expected due to the stochastic nature of diffusion (Figure 3.1E).

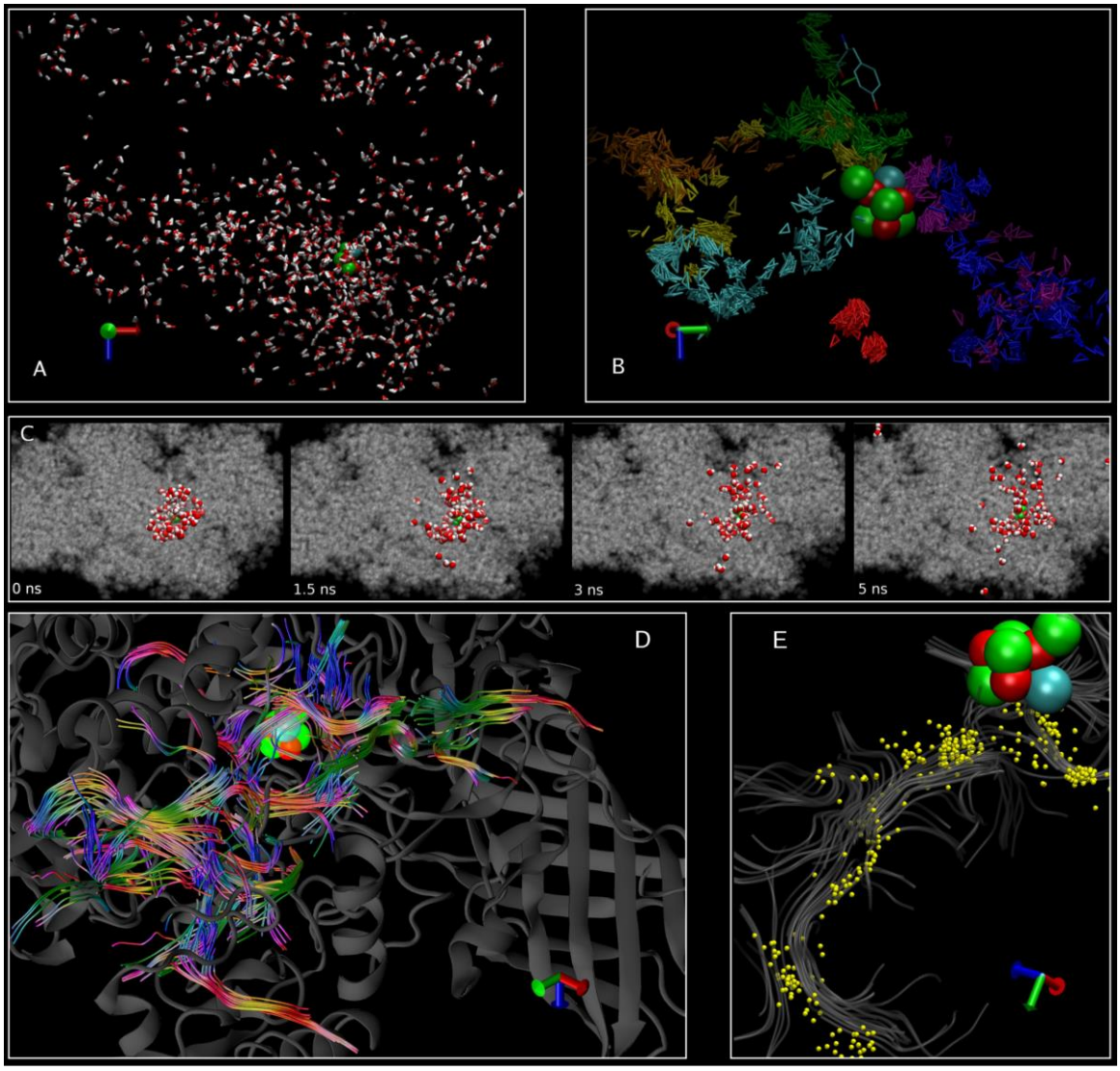

Figure 3.1. Structure and dynamics of water in PSII. A -water molecules in the PSII core complex found using the DOWSER program. B - Trajectories of motion of several representative water molecules in the interior of PSII protein. View along the membrane plane. C - Snapshots from dynamics simulation showing diffusion of water molecules inside the protein. Water molecules within 10 Å from OEC were initially selected. Also shown are OEC (green and red) and protein (grey), clipped for clarity at the level of OEC. View from the lumenal side of the membrane. D - Water streamlines in the PSII

core complex. The Mn and Ca atoms of the OEC are shown by spheres. E - Water streamlines in the interior of PSII core protein obtained from analysis of 10 ns long MD simulation. Streamlines propagating along the surface of the protein are not shown and the protein is clipped for clarity. Streamlines are color coded by direction: red streamlines propagate along the X-direction, green -Y, blue - Z. Right panel: streamlines (grey) overlapped with the trajectory of one representative water molecule from the MD run (yellow). The axis defines the world coordinate system which stays the same in all subsequent figures: the Z axis is normal to the plane of the thylakoid membrane.

3.4.3. Comparison of water channels found in this work to channels obtained from static structures

Previous dynamic simulations of water conduction within proteins (aquaporin-1 and aquaglyceroporin) revealed that water molecules moved in single file along a well defined channel and that their translocations were correlated(Zhu, Tajkhorshid, and Schulten 2001; Jensen et al. 2002). This study of water movement within PSII has shown very different patterns of motion. The water inside PSII protein is characterized by a complex hydrogen bond network within a highly branched channel system composed of wide and narrow areas and transiently connected hydrophilic pockets. It was found that water fills all previously known channels and moves inside them. This finding does not support the concept of exclusive O_2 or proton channels. In our simulation water molecules moved from the vicinity of OEC to the bulk water at the exterior of the PSII protein on a time scale of 5 ns which is much shorter than rate of water splitting (Dau and Haumann 2008) indicating that organization of PSII depends more on consideration of

restriction of the access of water to the OEC than on water delivery. Keeping water molecules at the active site long enough to complete water oxidation is one of the reasons to restrict water flow. A control gate preventing excessive water flow when OEC is not functioning would also help to stabilize the $CaMn_4$ cluster in the dark and minimize side reactions with small molecules carried with water. Regulation of substrate delivery to the active site by transient opening of passages in protein has been observed previously in acetylcholine esterase (H.-X. Zhou, Wlodek, and McCammon 1998). Water molecules were observed moving through transiently open pores both at the surface of the protein and in regions connecting different channel systems Formation of a straight and wide path through the PSII protein in the absence of the OEC would facilitate the delivery of metal ions to the site. PSII lacking the $CaMn_4$ cluster is a common occurrence under physiological conditions during the process of assembly or repair(Burnap 2004; Miller and Brudvig 1989; Aro, Virgin, and Anderson 1993). In this case a channel providing access of Mn^{2+}, Ca^{2+} and Cl^- to the active site must exist. When the active cluster is built and activated, incoming ions and cellular reductants are potentially harmful as they could impair water splitting by over reducing OEC or competing for the binding sites. A denser protein with narrow pores would then be desirable for strict control over water access.

Water streamlines and exit points obtained from analysis of an unconstrained MD simulation of the PS II core complex, including OEC, are shown in figure 3.2. It was found that water streams in all four of the channels or channel systems described in(Ho and Styring 2008), which had been named “broad”, “back”, “large” and ”narrow”. Our streamline analysis revealed new entrance points and interconnections between channels

that were not observed in the X-ray structure. MD simulations also showed that thermal motions of the proteins in PSII caused channel opening and closing. Figure 3.2A shows the transient opening and closing of an entrance in the area of the "two dotted arrow" entrance reported in figure 3.3, which permits water access into the "large" channel system described in the same work.

We determined the most probable pathways of water to OEC by counting water molecules that moved between the protein exterior and the OEC. 8 water molecules traveled between the protein surface and a 6 Å sphere, centered at the geometric center of OEC atoms. One of them took the "broad" channel via entrance 3. Seven water molecules used the "large" channel system, one each via entrances 7, 8, 10, 11 and 13, and two molecules used entrance 12 (Figure 3.2). Identification of potential water access control points. According to the previous functional assignments for the channels, incoming water molecules would need to cross a gap between the "back" channel (assigned as a water channel) and "narrow/broad" channels (assigned as proton exit channels) to reach the active site of the $CaMn_4$ cluster.

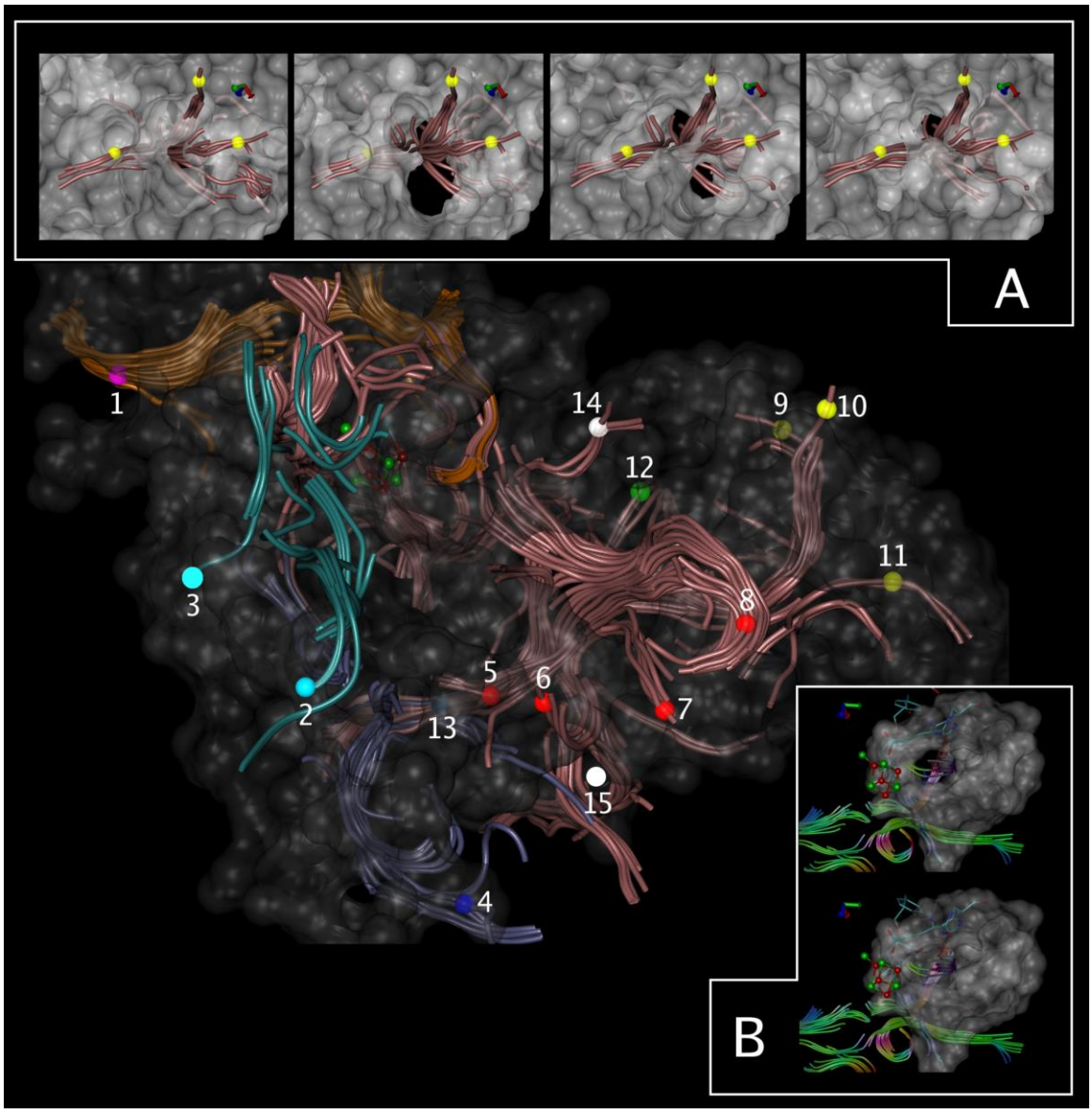

Figure 3.2. Water streamlines and exit points for PSII in the presence of OEC. Streamlines in the area of the "back" channel (see text for details) are shown in orange with a purple exit point (exit 1). Streamlines and exit points in the area of the "broad" channel are shown in cyan (exits 2,3). Streamlines and exit points in the area of the "narrow" channel are shown in blue (exit 4). Streamlines in area of the "large channel system" and near OEC are shown in pink. Red spheres – exits in the area of dashed arrow

exit in figure 4 of (Ho and Styring 2008)(exits 5-8). Yellow spheres - exits in the area of two dotted arrow exits in figure 4 of (Ho and Styring 2008) (exits 9-11). Green sphere - exit in the area of solid arrow exit in figure 4 of (Ho and Styring 2008)(exit 12). Blue sphere –exit from the large channel system leading into the "narrow channel" (exit 13). Upper white sphere – new exit near CP43-Thr412 (exit 14). Lower white sphere – new exit near PsbV-Asp79 (exit 15). Inserts A and B show snapshots of the protein solvent-accessible surface and streamlines in different areas of PSII. Insert A - shows the area of the "two dotted arrow" exits found previously (Ho and Styring 2008) . Transient opening and closing of the channel permits water access into the large channel system. Insert B shows the proximal end of the "back" channel. Streamline in the "back" channel continues all the way to the $CaMn_4$ cluster due to transient opening of the proximal end of the channel. Residues proposed to act as a "control gate" already reported in literature (Ho and Styring 2008) are shown by licorice. The surface of the protein was calculated using a probe radius of 1.4 Å.

This gap (residues D1-Tyr161, -His190, -Asp189, -Phe186 and -Asn165, and the Ca^{2+} ion) was proposed to act as a control gate for regulating substrate water access to the manganese cluster through transient changes in the diameter of the opening (Ho and Styring 2008). Many of the residues forming the gap have been also proposed to be important for water oxidation (Sproviero et al. 2008) indicating the possibility of differential water access to the Mn cluster during the S-state cycle. Our simulations did not detect water streamlines going from the "back" channel to the "narrow" or "broad" channels. However, we did find water streams inside the "back" channel extending beyond its previously found boundary towards the OEC to reach it directly (Figure 3B). This water stream is possible due to a transient widening of the proximal end of the back channel. Synergistic movement of the aminoacids lining this part of the back channel results in the opening of the back channel for water access to the active site.

This proximal extension of the back channel is lined by D1-Gln165, -Glu189, -His190, -Asn296, -Asn298, -Asp342, -Ala344, CP43-Leu401, -Gly402, -Gly409, -Val410, Ala411. This region includes three of the five aminoacids proposed to act as a gate between the back channel and narrow/broad channels. Our simulations confirmed that these aminoacids are important for water dynamics, however, the mechanism of water access to the active site revealed by our simulation is quite different from the previous proposal (Ho and Styring 2008). As a number of these residues have also been implicated in water oxidation it would be interesting to study water flow in this region as a function of charge accumulation during the S-state cycle. The protonation states of titratable residues within the protein are expected to be affected by the changing charges on the

$CaMn_4$ cluster this may influence the dynamic protein structure.

Although similar numbers of water molecules moved between the protein exterior and the OEC in both simulations, the pathways taken by the water molecules were different. Without OEC the “back” channel and the “large” channel system were used exclusively and water exited from only two areas: exit 1 and closely spaced exits 5-6, which had fused into one exit (Figures 3.2 and 3.3). The relatively straight water pathway in the simulation without OEC is in stark contrast with the curved and branched water path in the simulation with OEC (Figure 3.3). Many water exits in the presence of OEC were transient and relatively small in contrast to the wider and continuously open exits observed in the absence of OEC.

Differences between water streams with and without OEC arose from changes in protein conformation in two regions: OEC and an area where three C-terminal domains (CTD) of PsbU, PsbV and D2 are in close proximity to each other and the surface of the protein. This was also the area of the highest probability for water to exit from the large channel system in simulation without OEC (exits 5-6, Figure 3.2 and 3.3).

In all three chains, the aminoacids near CTD are highly conserved. A comparison of the two PSII structures (PDB ID 1S5L and 2AXT) revealed a significant difference in the folding of the PsbU and PsbV CTDs even though the folding was identical for the rest of subunits. This difference may arise from flexibility of the protein in this region and could result from different crystallization conditions. In the 1S5L stucture the two CT

aminoacids of both PsbU and PsbV form a flat and approximately round closed patch on the surface of the protein which would seal water access to the "large" channel system. Three of these aminoacids are tyrosines which are well suited for gating (H.-X. Zhou, Wlodek, and McCammon 1998). In the 2AXT structure, CTDs of PsbU and PsbV are not oriented to form a continuous surface patch. In our simulation with OEC, the two CT tyrosines of PsbV were in a different conformation than in either of the experimental structures. Due to a high degree of freedom in interaction between these three CTDs it is likely that a number of protein configurations characterized by different solvent accessibility may exist at physiological temperature. In our simulation without OEC, we observed an outward displacement of the CTD of PsbU leading to the fusing of two narrow and transiently open exits 5-6 into one wide and continuously open water exit. This process is initiated by a conformational change of the D1 CTD (Glu333- Ala344) which is stabilized by coordination of three aminoacids, Glu333, Asp342 and Ala344 with the $CaMn_4$ cluster. When the OEC is absent this loop shifts away from its initial position dragging along the CTD of D2. This conformational change of the D2 CTD directly affects the CTDs of both PsbU and PsbV and initiates the opening of the gate.

3.5. CONCLUSION

Our results have demonstrated the benefits of streamline tracing for analysis and visualization of water flow in MD simulations. This technique is particularly useful for the identification of transiently formed channels in a complex system of nanopores. Our investigation of water movement in PSII has introduced a novel perspective to the study of the supply of water to the OEC. We have shown that functional PSII is characterized by a complex branched water supply structure with transient entrances and multiple control points. Loss of the OEC from PSII causes a transition to a simpler, straighter, and wider channel with two permanent openings that is well suited to the transport of ions required to rebuild the $CaMn_4$ cluster. It seems unlikely that the access of water to the OEC is controlled by changes in protonation states as more than enough water can access the OEC through the channels found in this work.

Chapter 4

Factors controlling the redox potential of $ZnCe_6$ in an engineered bacterioferritin photochemical 'reaction centre'

Paper was published in PLoS One

A. Mahboob, S. Vassiliev, P. Podutoori, A. van der Est, and D. Bruce, PLoS ONE 8(7):e68421 **(2013)** "Factors Controlling the Redox Potential of $ZnCe_6$ in an Engineered Bacterioferritin Photochemical 'Reaction Centre'"

*Contribution was performing the MCCE calculations, spectroelectrochemical measurements, and DFT calculations

4.1. ABSTRACT

Photosystem II (PSII) of photosynthesis has the unique ability to photochemically oxidize water. Recently an engineered bacterioferritin photochemical 'reaction centre' (BFR-RC) using a zinc chlorin pigment ($ZnCe_6$) in place of its native heme has been shown to photo-oxidize bound manganese ions through a tyrosine residue, thus mimicking two of the key reactions on the electron donor side of PSII. To understand the mechanism of tyrosine oxidation in BFR-RCs, and explore the possibility of water oxidation in such a system we have built an atomic-level model of the BFR-RC using ONIOM methodology. We studied the influence of axial ligands and carboxyl groups on the oxidation potential of $ZnCe_6$ using DFT theory, and finally calculated the shift of the redox potential of $ZnCe_6$ in the BFR-RC protein using the multi-conformational molecular mechanics–Poisson-Boltzmann approach. According to our calculations, the redox potential for the first oxidation of $ZnCe_6$ in the BRF-RC protein is only 0.57 V, too low to oxidize tyrosine. We suggest that the observed tyrosine oxidation in BRF-RC could be driven by the $ZnCe_6$ di-cation. In order to increase the efficiency of tyrosine oxidation, and ultimately oxidize water, the first potential of $ZnCe_6$ would have to attain a value in excess of 0.8 V. We discuss the possibilities for modifying the BFR-RC to achieve this goal.

4.2. INTRODUCTION

The water splitting reaction of photosynthesis has been the most influential biologically catalyzed reaction on Earth. Acquiring the ability to use water as a source of electrons about 2.5 billion years ago allowed oxygenic photosynthesis to power a massive increase in the diversity and numbers of aerobic life forms. Photosystem II (PSII) is the pigment-protein complex embedded in the thylakoid membranes of plant chloroplasts and cyanobacteria that catalyses the light induced oxidation of water and reduction of plastoquinone in oxygenic photosynthesis (Barber 2003). This catalytic function is performed by light driven electron transfer (ET) reactions through redox cofactors of the PSII reaction center. Oxidation of water by PSII requires several essential cofactors: a photoactive strongly oxidizing pigment (P680), a redox-active tyrosine (Y_Z) and the oxygen-evolving complex (OEC) containing four high-valence manganese ions bound by μ-oxo bridges and a calcium ion (Umena et al. 2011). Electronic excitation of P680 and subsequent electron transfer to the primary pheophytin electron acceptor forms the strongly oxidizing $P680^{\bullet+}$ cation radical (E_m ~ 1.12 V) which then oxidizes Y_Z. Subsequently, Y_Z oxidizes the OEC where water oxidation occurs after the accumulation of four oxidation equivalents in the Mn_4CaO_5 cluster according to the S-cycle proposed by Joliot and Kok (Joliot, Barbieri, and Chabaud 1969; Kok, Forbush, and McGloin 1970). The coupling of water oxidation to photochemistry in PSII was a crucial milestone in the evolution of life allowing for the essentially unlimited conversion of sunlight energy to chemical potential energy which now powers most life on Earth. The successful mimicking of this reaction in an artificial system could form the basis of a clean alternative energy source. Recently, bacterioferritin (cytochrome b1, BFR) was used as a

protein scaffold for constructing a linear electron pathway that mimics some of the electron transfer components within PSII (Conlan et al. 2009).

Ferritins are the principal iron storage proteins in most living organisms (Andrews, Robinson, and Rodríguez-Quiñones 2003; Andrews 2010; Carrondo 2003). The protein BFR is a robust iron storage bacterial protein that forms a homodimer, with each subunit (~18.5 kDa) being composed of an antiparallel, four-helical bundle (Dautant et al. 1998; Frolow, Kalb, and Yariv 1994; Crichton and Declercq 2010) as shown in figure 4.1. The homodimers self-assemble into a dodecamer that forms a spherically shaped protein shell surrounding an internal cavity encapsulating an iron core composed of ferric hydroxyphosphate micelles (Crichton and Declercq 2010). Each BFR subunit binds 2 iron ions (Fe^{2+}) and contains seven tyrosine residues (Crichton and Declercq 2010; Frolow, Kalb, and Yariv 1994). The BFR dimer binds one b-type heme at the interface between subunits(Andrews, Robinson, and Rodríguez-Quiñones 2003). In each subunit three tyrosines are located close to both metal ions and the heme (figure 4.1). Thus, a protein scaffold of BFR is suitable for constructing a photoactive reaction center mimicking the electron transfer reactions of PSII. A prototype of such a 'reaction center' (BFR-RC) has been created by replacing the heme with a photoactive zinc-chlorin-e_6 ($ZnCe_6$) pigment and the iron ions with Mn(II) ions (Conlan et al. 2009). It has been found that the bound $ZnCe_6$ species are capable of initiating electron transfer upon illumination, oxidizing a tyrosine residue and the bound manganese Mn(II) ions (Conlan et al. 2009). The mechanism of the light activated electron transfer observed in BFR-RC, however, remains poorly understood. It is not clear whether photooxidation of tyrosine

and the bound manganese are sequential or independent events. One of the central questions key to understanding ET pathways, overall efficiency and limitations of BFR-RC is the unknown value of the oxidation potential of the $ZnCe_6$ cation radical in BFR-RC. The E_m of $ZnCe_6$ provides the driving force for oxidation of cofactors and its value will determine which mechanisms of tyrosine oxidation are possible and whether this BFR-RC may eventually be able to oxidize water. To our knowledge the oxidation potential of $ZnCe_6$ has not been measured experimentally in either solvent or protein. The present article investigates the oxidation and reduction potentials of $ZnCe_6$ in solution and in BFR-RC with a combination of experimental and computational methods. Our focus is on understanding factors influencing the redox potential of $ZnCe_6$ within BFR-RC with an aim to identify possible means of controlling it.

4.3. METHODS

4.3.1. Synthesis of $ZnCe_6$

$ZnCe_6$ was prepared by metallating chlorin e_6 with $Zn(OAc)_2$ by standard methods (Patiño, Campos, and Torres 2007). Typically, 40 mg (0.067 mmol) of chlorin e_6 and 37 mg (0.20 mmol) of $Zn(OAc)_2$ were stirred at room temperature in a $CHCl_3$/CH3OH (8/4 ml) solvent mixture. The reaction was monitored by absorption spectroscopy. A red shift of the Q_Y absorption band from 661 to 640 nm accompanied incorporation of zinc. We also confirmed formation of $ZnCe_6$ by observing the disappearance of the free base pigment protons by NMR spectroscopy. After completion of metallation the solvents

were evaporated and the residue was washed with water and cooled methanol to get spectroscopic grade pure compound. The yield of reaction was 39 mg (89%).

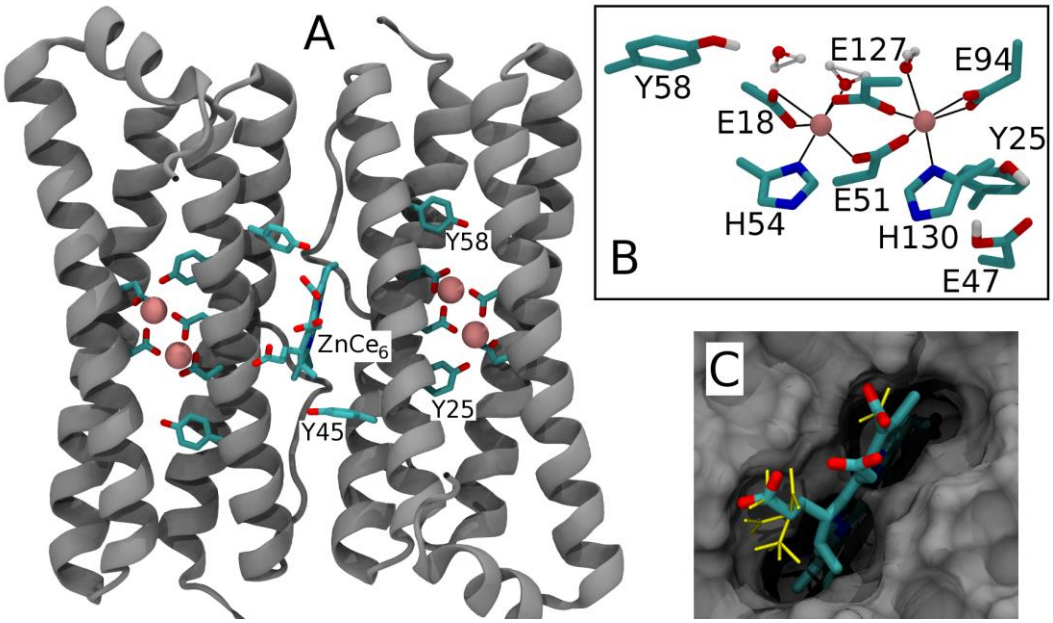

Figure 4.1. Atomic level model of the *E. coli* bacterioferritin. A - homodimer showing two identical subunits each hosting two manganese ions and $ZnCe_6$ bound at the interface of the subunits. B – manganese binding site. C - $ZnCe_6$ in its binding site. The ensemble of carboxylic acid conformations used to compute pKas is shown in yellow. Model is based on the X-ray diffraction structure PDB ID: 3E1M.

4.3.2. Electrochemical measurements

Differential pulse voltammetric measurements were performed in pyridine and DMSO containing 0.1 M tetrabutylammoniumhexafluorophosphate ($TBAPF_6$) on a BAS Epsilon electrochemical analyzer (working: Pt, auxiliary electrodes: Pt wire; reference electrode: Ag). The pulse width, period and amplitude used were 50 ms, 200 ms and 50 mV,

respectively. Sample concentration was 1 mM and ~100 fold excess of N-methylimidazole was added to prevent aggregation between $ZnCe_6$ molecules. Resultant solutions were purged with nitrogen gas for 10 min prior to the scan. The ferrocene/ferrocenium couple was used to calibrate the redox potential values. All experiments were performed at 296 K. The use of water as solvent for electrochemical measurements was avoided to eliminate reactions of cations and di-cations with water and any changes in E_m which could arise from ionization of $ZnCe_6$ carboxylic acid groups.

Spectroelectrochemical measurements were performed at a platinum mesh electrode in a thin layer spectroelectrochemical cell (0.5 mm). Potentials were applied and monitored using the same potentiostat as for the differential pulse volammetric measurements. Absorption spectra were recorded with an Ocean Optics USB650 Red Tide spectrometer.

4.3.3. Calculation of the shifts to the redox potential of $ZnCe_6$ due to coordination to axial ligands, ring substituent groups, and dielectric constant

To calculate the shift to the redox potential due to axial ligation for the $ZnCe_6^+$/ $ZnCe_6$ couple, we performed computations using density functional theory (DFT). The B3-LYP functional with the LanL2TZ+ basis set for the Zn atom and 6-311G+** for C, H, N and O were used. Gas-phase zero-point energies, thermal corrections, and entropic corrections were calculated using standard formulas for the statistical thermodynamics of an ideal gas using optimized geometries and scaled by 0.9613 B3-LYP/6-31G*/LanL2TZ+ frequencies (Merrick, Moran, and Radom 2007). Solvation energies of

the studied species in the various solvents were calculated using the solvation model SM8 (Marenich et al. 2007) at the B3-LYP/6-31G* level of theory. In all solvation energy calculations the LanL2TZ+ basis set was used for Zn.

4.3.4. Model of BFR-RC

The X-ray bacterioferritin structure, (PDB ID: 3E1M), from *E. coli* with a resolution of 2.7 Å was used as a starting point for calculations. The structure was modified to match an engineered BFR-RC described in (Conlan et al. 2009; Hingorani et al. 2009). Two surface exposed histidines (H46, H112) were mutated to arginines, the heme was replaced with photoactive $ZnCe_6$ and iron ions were replaced with Mn(II) ions.

In BFR protein the heme binds in a symmetrical hydrophobic pocket located on a twofold axis between symmetry related subunits. As the structure of $ZnCe_6$ is similar to the structure of *b*-type heme ($ZnCe_6$ has formyl, acetyl and propyl groups at positions 13, 15 and 17 and saturated ring IV while heme has propyl groups at 13 and 17 and all rings unsaturated) we placed $ZnCe_6$ in the same position and orientation as heme in the BFR. After initial placement of $ZnCe_6$ in its binding pocket, conformations of the three carboxylic groups of $ZnCe_6$ were optimized using a Monte-Carlo search as implemented in MCCE. The highest occupancy conformers were then used as a starting structure for a complete energy minimization of the whole BFR-RC with constrained backbone atoms which was then followed by a short 10-ps unconstrained molecular dynamics run. AMBER version 10 (Case, D. A., Darden, T. A., Cheatham, T. E., Simmerling, C., Wang, J. 2008) was used for molecular mechanics computations. The "pairwise" generalized Born implicit solvent model (Hawkins, Cramer, and Truhlar 1996) was used

in these simulations. Initially we used standard ionization states for all aminoacids, and all 3 carboxylic groups of $ZnCe_6$ were protonated. The final RMSD of the protein backbone between the original PDB ID: 3E1M structure and BRF-RC was 0.15 Å. Next we performed ONIOM QM/MM geometry optimization of the whole protein with $ZnCe_6$ and its methionine ligands treated quantum mechanically at the B3LYP/6-31g* level using Gaussian 09 (Frisch, M. J., Trucks, G. W., Schlegel, H. B., Scuseria, G. E., Robb, M. A.). In QM/MM optimized structures both methionine ligands were almost equidistant from Zn. The equilibrium distances between Zn and S were found to be 2.80/2.85 Å. The QM/MM optimized structures of neutral and radical $ZnCe_6$ with its 2 methionine ligands were used to refine atom-centered point charges obtained from the initial model. The optimized structure of the BFR-RC with bound $ZnCe_6$ is available in PDB format in supporting Model S1 in (Mahboob et al. 2013).

4.3.5. Derivation of the atomic partial charges for $ZnCe_6$

The atomic partial charges for $ZnCe_6$ were obtained using the two stage RESP formalism (Bayly et al. 1993)., , with a weighting factor of 0.0005/ 0.001 from a wavefunction computed at the HF/6-31G* level for H, N, C, O, and HF/LanL2TZ+ for Zn. Schematic diagram of $ZnCe_6$ is shown in **APPENDIX II** - Figure S1, atomic point charges for $ZnCe_6$ are available in Table S1. QM calculations were done with the Gaussian09 package (Frisch, M. J., Trucks, G. W., Schlegel, H. B., Scuseria, G. E., Robb, M. A.).

4.3.6. Computation of protonation pattern and shift of the redox potential of $ZnCe_6$ in BFR-RC

MCCE2.4 (Song, Mao, and Gunner 2009) was used to predict the ionization state of each protein residue and cofactor as a function of E_h and pH. The algorithm performs Monte-Carlo sampling of multiple aminoacid side chain geometric and ionization conformations, where conformer energies include electrostatic and van der Waals terms. Before sampling, rotamers of aminoacid side chains were generated using 60 degree increments for each rotatable bond, while conformers of carboxylic acid groups of $ZnCe_6$ were generated in 14 degrees increments. Pairs of conformers with clashes not exceeding 5 kcal/mol had their positions optimized. Finally, a genetic algorithm was used to optimize side chain conformers (Comte et al. 2011). Electrostatic conformer-conformer pairwise interactions and reaction field energy for each conformer were computed by solving the linearized Poisson-Boltzmann equation using the Delphi program (Li et al. 2012). The dielectric constant was set to 4 inside the protein and 80 in the solvent. PARSE radii and charges (Baker et al. 2010) were used in Poisson-Boltzmann calculations for all elements except Zn. For Zn, a radius of 1.47 Å was used (Tan, Yang, and Luo 2006). To obtain the E_m of $ZnCe_6$ in BRF-RC the shift of the redox potential in the protein was added to the E_m of the reference model system.

In calculations of the shift of E_m in a protein environment several factors were considered: (i) the desolvation energy difference arising from moving the cofactor from water into protein , where the protein volume is simply considered as dielectric medium $\Delta\Delta G_{desolv}$, (ii) the electrostatic and VDW non-electrostatic interaction of the cofactor

with the protein backbone ΔG_{bkbn}, and (iii) the mean field pairwise interaction between the cofactor and side chains of residues in the protein in the distribution derived by Monte Carlo sampling ΔG_{res}^{mfe}. The difference in each energy term is between the oxidized and the reduced cofactor. Details of the calculations of these factors are described in (Song, Michonova-Alexova, and Gunner 2006).

In continuum electrostatics calculations $ZnCe_6$ and side chains of its methionine axial ligands were represented as a single residue with an oxidized or reduced conformer. The backbone atoms of the axial ligands remained as part of the protein backbone. QM treatment of the complex of $ZnCe_6$' ($ZnCe_6$ without carboxylic groups) with 2 methionine axial ligands yielded $E_{m(sol)}$ of 0.58 mV (see Results section 3.3) which was used as the reference for MCCE calculations. The three carboxylic groups of $ZnCe_6$ were treated as independently ionizable groups.

4.4. RESULTS

4.4.1. Oxidation and reduction potentials of $ZnCe_6$ in solution

$ZnCe_6$ has low solubility in most organic solvents. We were able to measure its redox potential in only two solvents (pyridine and DMSO). Although we observed oxidation waves in both solvents, only with N-methylimidazole were two clear waves visible. Voltammograms measured in DMSO without N-methylimidazole showed multiple redox waves (data not shown), suggesting that under these conditions several different aggregation states of $ZnCe_6$ co-existed in the sample. Aggregation occured most likely

due to the coordination of Zn by Lewis base atoms of the substituent carboxyl groups. These aggregates can be broken down by addition of stronger Lewis bases such as N-methylimidazole. Indeed, after addition of N-methylimidazole to the $ZnCe_6$/DMSO solution, two distinctive redox couples appeared in the oxidative scan. The major oxidation peaks were centered at 0.54 and 1.01 V vs. standard hydrogen electrode (SHE) (Figure 4.2A). In addition a smaller and broader feature was observed at 0.8 V. The spectral changes obtained during oxidation of $ZnCe_6$ at 0.54 V are shown in figure 2B. The Q_Y band of the neutral compound at 640 nm decreased in intensity while a new absorption band grew at around 800 nm. These spectral features can clearly be assigned to a chlorin π cation radical. The difference between the first and the second oxidation of methylimidazole-coordinated zinc porphyrins has been reported to be in the range of 0.46-0.66 V (Lin, Fang, and Cheng 2002).

In this study, the voltammogram the peak centered at 1.01 V, matching this difference of methylimidazole-coordinated zinc porphyrin, was assigned to a two electron oxidation of $ZnCe_6$. There was one redox couple in the reductive scan at -1.26 V tentatively assigned to the formation of the $ZnCe_6$ anion radical (Figure 4.2).

4.4.2. Effect of axial ligands and carboxyl groups on the oxidation potential of $ZnCe_6$ in solution

To calculate the E_m of $ZnCe_6$ in BFR we needed a reference E_m corresponding to $ZnCe_6$ ligated by methionine without carboxyl groups in water. To obtain this value from the measured E_m of $ZnCe_6$ in DMSO we computed shifts to the E_m due to different solvents,

axial ligands and carboxyl groups. Axial ligands are known to induce changes in the electrochemistry of metalloporphyrins and metallochlorins (Lin, Fang, and Cheng 2002; Heimdal et al. 2007). For example, it was found that upon imidazole ligation the first oxidation potential of zinc porphyrins shifts negatively by 150 mV in CH_2Cl_2 (Heimdal et al. 2007). In contrast the second oxidation potential of complexed zinc porphyrins shifted positively by 50-270 mV when compared with the uncomplexed zinc porphyrins depending on the nature of the substituents (Heimdal et al. 2007).

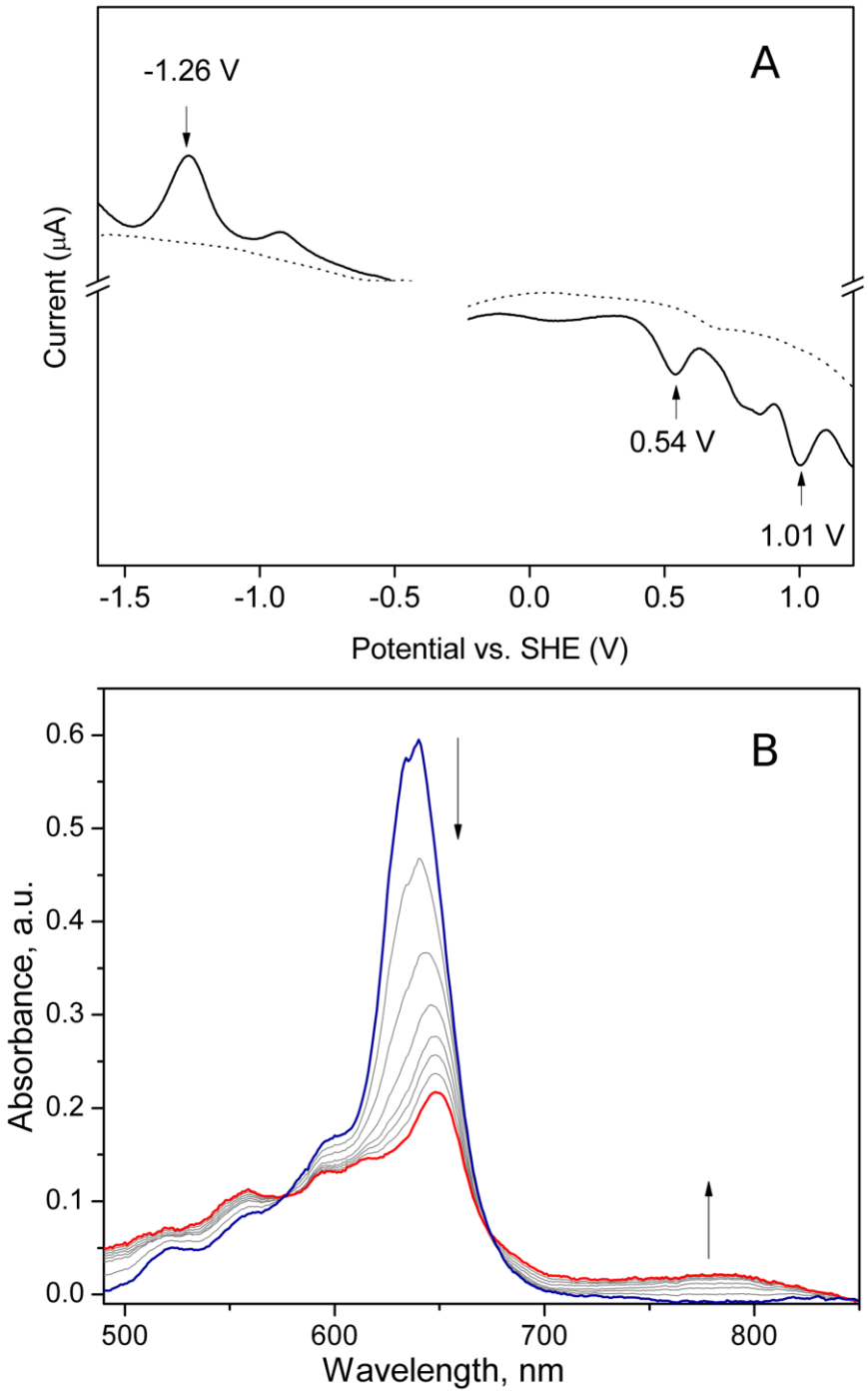

Figure 4.2. A: Differential pulse voltammogram of $ZnCe_6$ in DMSO with 0.1 M $TBAPF_6$. [$ZnCe_6$] = 1 mM. Voltammogram of the solvent is shown by dotted line. B: Spectral changes during the oxidation of $ZnCe_6$ at 0.54 V. See Results section for details.

Our DFT calculations showed that N-methylimidazole shifts the first oxidation potential of $ZnCe_6$ in water negatively by 70 mV, while the coordination to 2 methionines had a smaller negative shift of only 20 mV (Table 4.1). This trend is similar to the results of previous computational work on chlorophyll *a* (Kee et al. 2007).

A second factor affecting the oxidation potential is the nature of ring substituent groups (Kee et al. 2007). In general, electron withdrawing groups shift the oxidation potential up while electron rich groups shift it down. Protonated carboxyl groups, being electron withdrawing, are expected to up-shift the redox potential. This effect is pH dependent as ionization of carboxyl groups stabilizes the cation radical, and hence will down-shift the redox potential.

To estimate the shift of the redox potential of $ZnCe_6$ in BFR-RC protein we treated the carboxyl substituent groups and Zn–chlorin as separate units, affecting each other via classical electrostatic and VDW interactions. This approach allowed us to sample efficiently multiple conformational and ionization states of carboxylic acids. A similar approach was previously successfully used for calculation of heme redox potentials in different proteins (Zheng and Gunner 2009). These calculations require knowledge of the reference redox potential of Zn–chlorin without carboxyl groups in water, while experimentally we measured $ZnCe_6$ with three substituent carboxylic groups in DMSO. Therefore, to obtain the reference redox potential of Zn–chlorin we estimated differences in redox potential due to solvent and the presence of carboxyl groups computationally.

The DFT calculations of this work showed that the redox potential of both coordinated and non-coordinated $ZnCe_6$ changes insignificantly between DMSO and water. This

result is consistent with previous experimental and theoretical studies of chlorophyll *a* (K. Hasegawa and Noguchi 2005) in solvents with different dielectric constant. However, the attachment of protonated carboxyl groups to Zn-chlorin in different coordination states leads to an increase of the redox potential by 0.13-0.14 V in water.

Table 4.1. Oxidation potentials of the $ZnCe_6$ and $ZnCe_6$ without carboxylic acids in continuum solvents with different values for the dielectric constant.

Axial ligand	**$ZnCe_6$ w/o carboxylic groups**			**$ZnCe_6$**		
	Gas □=1	DMSO □=46.8	Water □=78.4	Gas □=1	DMSO □=46.8	Water □=78.4
No	1.54	0.44	0.51	1.59	0.55	0.64
2 Met	1.32	0.35	0.48	1.36	0.47	0.62
Imidazole	1.15	0.36	0.44	1.20	0.48 (0.54[a])	0.57

[a] - experimentally measured value.

To estimate the accuracy of our DFT calculations we determined the E_ms of 10 different zinc chlorins and compared them to experimental values (Kee et al. 2007). All computed values were systematically lower than the experimental values by 0.1 V. After correction for this systematic shift, the computed E_ms were within 0.03 V of the experimental values **APPENDIX II**- Figure S2. Overall, the reference oxidation potential corresponding to

the first oxidation of bis-methionine coordinated $ZnCe_6$ in water without carboxylic groups was estimated to be 0.58 V vs. SHE.

4.4.3. Oxidation potential of $ZnCe_6$ in BFR-RC

In BFR-RC $ZnCe_6$ is partially buried in the protein. Our Monte-Carlo simulations estimate that desolvation due to embedding into the protein's lower dielectric increases the E_m of $ZnCe_6$ by 0.07 V. Another modest increase of the E_m arises from interaction with dipoles of the protein backbone (0.05 V). In contrast the side chains of aminoacids (including the $ZnCe_6$ carboxylic groups) decrease the redox potential (Table 4.2).

The ionization state of the carboxyl groups is expected to affect the $ZnCe_6$ redox potential. While neutral carboxyl groups increase E_m by 0.14 V in water (Table 4.1), ionized groups will stabilize the cationic form and shift the E_m down. In addition the redox state of $ZnCe_6$ is bound to affect the pKas of its carboxyl groups. Oxidized $ZnCe_6$ will tend to lower the pKas and increase ionization of the carboxyl groups. This would tend to further lower the $ZnCe_6$ oxidation potential.

Table 4.2. Effect of ionization state of three carboxylic groups of $ZnCe_6$ on its E_m.

	$E_{m(sol)}$	ΔG_{desolv}	ΔG_{bkbn}	ΔG^{mfe}_{total}	ΔG^{mfe}_{prot}	ΔG^{mfe}_{desolv}	E^{mfe}_m
All 3 titrated	0.58	0.07	0.05	-0.13	-0.10	-0.04	0.57
All 3 neutral	0.58	0.07	0.05	-0.03	-0.12	0.08	0.67
All 3 ionized	0.58	0.07	0.05	-0.22	-0.08	-0.14	0.48

*Computed at pH=6.

The case when all carboxyl groups are protonated before oxidation and remain protonated after oxidation provides an upper bound for the $ZnCe_6$ redox potential. With pKa values determined in the previous section, the charges of carboxylic groups with neutral $ZnCe_6$ at pH 6 are: -0.25, -0.56, -0.88 for formyl, acyl and propyl respectively when all carboxylic groups were titrated together. The probability of fully protonated $ZnCe_6$ (the product of occupancies of all 3 protonated groups) in this case is fairly low (4.4%). However, performing a titration of $ZnCe_6$ while the propyl group is fully charged decreases the redox potential by only 0.02 V compared to an all-neutral titration. The charges of carboxyl groups with the cation radical of $ZnCe_6$ at pH 6 increase to -0.93, -0.25, -0.93 for formyl, acyl and propyl respectively. The probability of a fully protonated cationic form of $ZnCe_6$ is very low. If all carboxylic groups are protonated in both cationic and neutral forms, the $ZnCe_6$ has an E_m of 0.67 V (Table 4.2). This result gives an idea of how high the E_m of $ZnCe_6$ in BFR-RC could be if the carboxyl groups were to be replaced by neutral groups. In another extreme, when all carboxyl groups are ionized, $ZnCe_6$ has the lowest E_m of 0.48 V (Table 4.2). Of course the actual value of E_m is somewhere between 0.48 and 0.67 mV. In agreement with upper and lower bound estimates we obtained an E_m of 0.57 V at pH 6 in calculations when the ionization of titratable groups was sampled simultaneously with the redox titration of $ZnCe_6$. Our calculations also showed that in the pH interval from 4 to 8, the E_m decreases by 0.21 V (Figure 4.3).

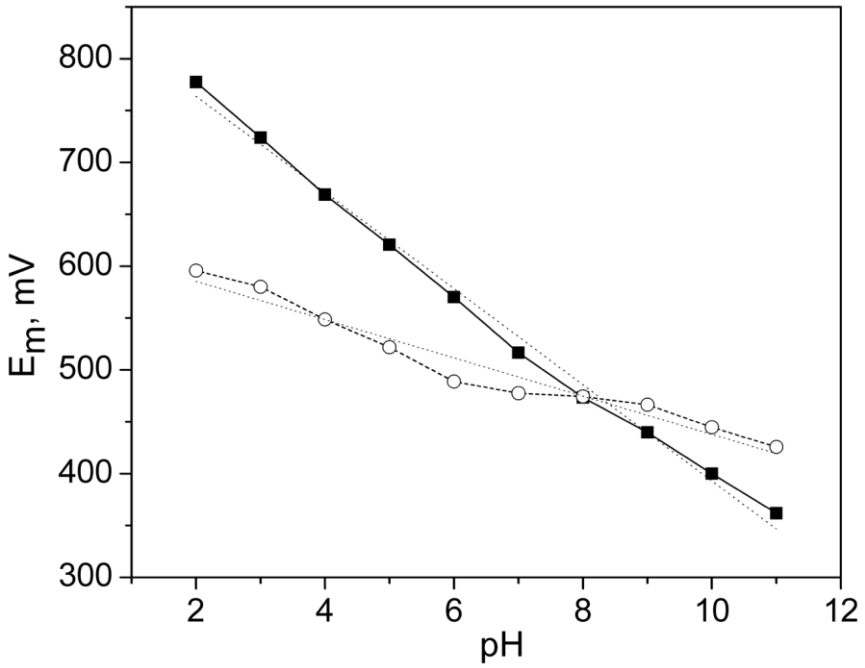

Figure 4.3. Calculated pH - dependence of the E_m of $ZnCe_6$ in BFR-RC (solid line, slope −46.4, R = 0.994) and in water (dashed line, slope −18.4, R = 0.950).

Contributions to the E_m shift from individual aminoacids in the BFR-RC are listed in Table 4.3. Seven aminoacids, located close to $ZnCe_6$, have the largest contributions to the E_m shift (Figure 4.4). Four of these aminoacids form two pairs of salt bridges between two monomers, while one pair (Asp50-Lys53) forms a salt bridge within a single protein subunit. Although each of these charged aminoacids would have a large effect on E_m if considered separately, their participation in salt bridges neutralizes their effective charge greatly, thus decreasing their ability to shift the E_m. Finally a large fraction of the decrease comes from Asn23. This aminoacid decreases E_m by -0.02 V in both monomers of the homodimer resulting in total shift of -0.04 V. The two manganese clusters

contribute -0.02 mV each, and the longrange electrostatic contributions from the rest of the protein aminoacids decrease the E_m by -0.02 mV.

Table 4.3. Contributions from aminoacid side chains to the shift of $ZnCe_6$ E_m.

Aminoacid	E_m shift	Aminoacid	E_m shift	Total
Arg30	**0.08**	**Asp56**	**-0.08**	0.00
Lys 33	**0.01**	**Glu 60**	**-0.02**	-0.01
Lys 53	**0.03**	**Asp 50**	**-0.02**	0.01
Asn 23	-0.04			-0.04
Others				-0.05

*Computed at pH=6. Aminoacid pairs participating in salt bridges between chains A and B are shown in bold in the one row. The total E_m shift, computed as sum of both monomers is shown.

4.4.4. Oxidation potentials of tyrosines in BFR-RC

Three tyrosines in BRF-RC are located near $ZnCe_6$ and the di-metal center. Tyr25, 45 and 58 are found at 3.8/10.6, 13.7/4.5 and 5.8/10.4 Å from the di-metal center/$ZnCe_6$ respectively. The four other tyrosines are located at the periphery of the protein far from both cofactors. After performing Monte-Carlo sampling of protonated neutral and protonated cationic radical species to determine the redox potential of each tyrosine in BFR-RC we found that Tyr25 has the lowest oxidation potential.

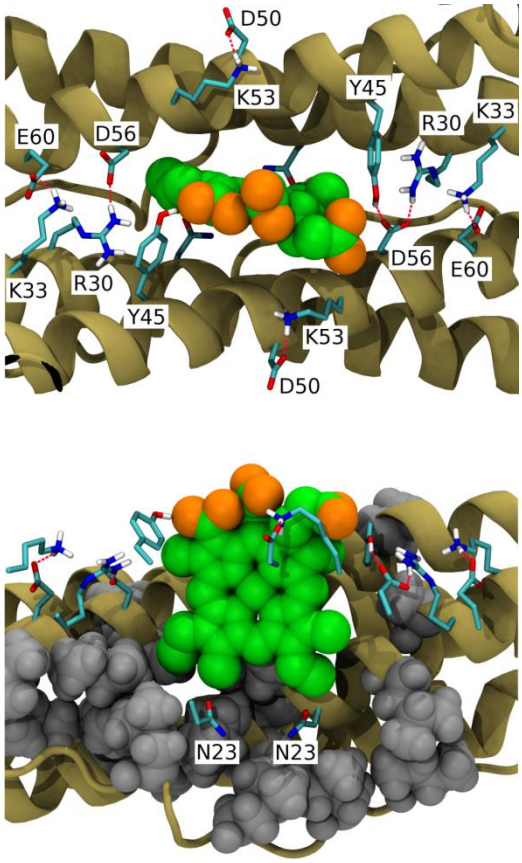

Figure 4.4. Aminoacids contributing the most to the E_m shift of $ZnCe_6$.

Grey spheres represent hydrophobic side chains.

The decrease of Tyr25's oxidation potential arises from the high polarity of its immediate environment which stabilizes the Tyr25 cation radical. The protein environment of Tyr25 is shown in figure 4.5. The polarity of the Tyr25 environment is reflected by increase in its pKa of ~10 units. Most of this shift is due to Asp90 and Glu47. The presence of these two negatively charged amino acids in the vicinity of Tyr25 destabilizes the deprotonated form of Tyr25, while the positively charged radical is favoured.

Our Monte-Carlo simulations indicated that at pH 8 the Tyr25 oxidation potential is decreased in BFR-RC by 160 mV relative to the tyrosine reference potential of 1380 mV in solution. The oxidation potentials of all other tyrosines in BFR-RC are increased by >250 mV. The largest contributions to the E_m shift of Tyr25 are from Asp90 (-300 mV), the di-metal center with its ligands (-108 mV), Glu47 (-50 mV), Glu44 (30 mV) and Asp50 (-40 mV). Glu44, Glu47 and Asp90 are located approximately equidistantly from Tyr25, but only Asp90 has a large effect on its oxidation potential. This difference is because only Asp90 is fully ionized. Occupancy of the charged species of Glu47 is 0.2, and Glu44 which has the lowest influence on the shift of Tyr25 E_m is neutral. The occupancy of the neutral species of both Glu47 and Glu44 is high because both of them are located in a hydrophobic environment (Leu40, Leu87, Leu134, Trp133). Despite the decreased oxidation potential of Tyr25 in BFR-RC (1220 mV) it is still too high for a cation of $ZnCe_6$ to oxidize.

4.4.5. Implications for the oxidation of tyrosine

The E_m of $ZnCe_6$ in DMSO is 0.54 V and our calculations predict that it remains not far from this value when $ZnCe_6$ is embedded in BFR-RC. This E_m value is significantly lower than was anticipated (Conlan et al. 2009), and well below that required to oxidize water. It also raises the question of how $ZnCe_6$ oxidizes tyrosine in the BFR-RC, as in all known cases the redox potential of tyrosine in proteins is near 1 V (Moore et al. 2010; Berry, Martinez-Rivera, and Tommos 2012; Ishikita and Knapp 2006). However, light-induced tyrosine oxidation has been observed in BFR-RC (Conlan et al. 2009).

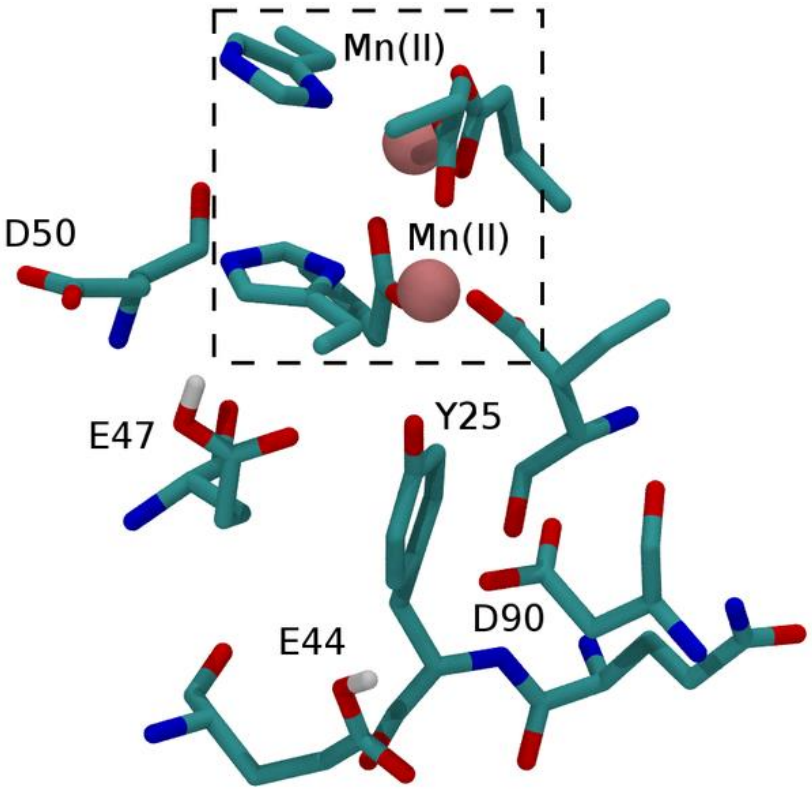

Figure 4.5. Details of the protein environment of Tyr25.

How can tyrosine be oxidized by $ZnCe_6$?

In PSII there are three possible mechanisms for the oxidation of tyrosine in the redox reaction between P680 and Mn-cluster (Tommos and Babcock 2000).

Reaction 1. $Y^- \rightarrow Y^{\cdot} + e^-$, $E_{m\,(sol)}^{Y^{\cdot}/Y^-}$ = +680 mV

Reaction 2. $YH \rightarrow Y^{\cdot} + H^+ + e^-$, $E_{m\,(sol)}^{Y^{\cdot}/YH}$ = +970 mV

Reaction 3. $YH \rightarrow YH^{\cdot +} + e^-$, $E_{m\,(sol)}^{YH^{+\cdot}/YH}$ = +1380 mV

Where species of tyrosine are denoted as: YH, protonated neutral; $YH^{\cdot +}$, protonated cationic radical; $Y^{\cdot}$, deprotonated anion; $Y^{\cdot}$, deprotonated neutral radical. These standard potentials were measured for N-acetyl-$_L$-tyrosinamide in aqueous solutions (Tommos and Babcock 2000; Klapper 1991).

In aqueous solution, the pathway of tyrosine oxidation depends predominantly on pH. In a protein, these reactions can also be controlled by hydrogen bonds or electrostatic interactions of tyrosine with its local environment.

Our computations suggest that none of the above reactions could be driven by photooxidation of $ZnCe_6$. Reaction 1 requires the redox active tyrosine to be ionized. Tyrosine ionization can only occur if positive charges near the tyrosine significantly lower its pKa. None of the tyrosines in BFR-RC satisfy this requirement.

Reaction 2 requires a somewhat higher oxidation potential as compared to reaction 1. In solution Tyr is oxidized by this mechanism at +970 mV. Reaction 2 is proton-coupled

and requires a suitable proton acceptor e.g. a nearby His, able to bind the proton released by tyrosine. None of the tyrosines in BFR-RC have suitable His proton acceptors nearby. However, we cannot exclude that water hydroxyls in specific hydrogen bond networks may accept protons from tyrosine.

In solution, reaction 3 occurs at +1380 mV, in PSII the calculated E_m for this reaction is raised to +1576 mV (Ishikita and Knapp 2006). We estimated that Tyr25 has the lowest oxidation potential of all tyrosines in BFR-RC, its E_m is around 1220 mV. Our calculations indicate that the single oxidized $ZnCe_6$ with oxidation potential of 570 mV at pH 6 would not be capable of tyrosine oxidation. Considering that a tyrosine cation radical EPR signal in BFR-RC has been observed after a prolonged exposure to saturating light or several saturating laser flashes (Hingorani et al. 2009) we suggest that a photogenerated $ZnCe_6$ di-cation (Fajer et al. 1970) may be responsible for oxidizing tyrosine. The $ZnCe_6$ di-cation, having a solution value of 1022 mV, would have a sufficiently high E_m to oxidize tyrosine in BFR-RC after taking protein effects into account.

4.4.6. Comparison of $ZnCe_6$ to natural primary donors

It is clear from our results that the relatively low oxidation potential of $ZnCe_6$ limits its use in the construction of a BFR-RC that would eventually be capable of oxidizing water. What factors could help increase the oxidation potential of $ZnCe_6$? Oxidation potentials of reaction center chlorophylls in photosynthetic organisms span a wide range from only 500 mV for P700 in PSI (Brettel 1997) and P870 in purple bacteria (Williams et al. 1992)

to 1,100–1,200 mV for P680 in PSII (Rappaport et al. 2002; Ishikita et al. 2005). Several major factors give rise to the differences in E_m (Ishikita et al. 2006). Most of the difference in E_m between reaction centers of PSI and PSII originates from the protein atomic charges and charges of cofactors. Together they up-shift the E_m of P_{D1} in PSII by 325 mV, but, in contrast, shift the E_m of P_A in PSI down by -125 mV (Ishikita et al. 2006). One of the major factors raising the E_m of P680 in PSII is the unique Mn_4Ca cluster, bearing a large positive charge. This cluster alone shifts the E_m of P_{D1} in PSII up by 214 mV. The BFR-RC has two di-manganese centers composed of Mn(II) ions. Each of the di-manganese centers shifts the E_m of $ZnCe_6$ up by 85 mV. However, this effect in BFR-RC is compensated by the charged ligands to the manganese, which down-shift the E_m by -90 mV. The combined effect of all aminoacid sidechains was found to shift the E_m of BFR-RC down by about -92 mV, not as much as the sidechains of PSI lacking the Mn_4Ca cluster. It is likely, however, that this down-shift would become smaller and maybe even turn into an up-shift with photooxidation of Mn(II) ions and formation of □-oxo bridges. Another major factor contributing to the increase of the E_m in P680 in PSII is its position close to the luminal edge of two transmembrane □-helixes (helixes $d_{D1/D2}$ providing axial His ligands to $P_{D1/D2}$). The protein backbone dipole of helix d shifts the E_m of P_{D1} in PSII by about 95 mV. The corresponding helix in PSI (helix j) shifts the E_m of P_A down by 28 mV (Ishikita et al. 2006). The organization of helices coordinating $ZnCe_6$ in the BRF-RC is more similar to PSI than to PSII, which is reflected by similar contributions from the backbones (40 mV).

The choice of $ZnCe_6$ for the role of photoactive pigment is attractive because of its availability and solubility in water, however, our work demonstrated that this pigment is not capable of providing sufficient oxidative power for the water splitting reaction. One of the problems is the detrimental effect of ionized carboxyl groups on the redox potential. Our calculations indicate that a simple replacement of these groups with neutral groups would increase the E_m of $ZnCe_6$ by 130 mV. Even higher potentials may be achieved by replacement of the acidic groups with basic groups.

Axial ligands to Zn are another factor known to affect redox potentials. For example, it has been shown that Met-Met coordination increases the potential of heme by about 200 mV compared to His-Met ligated heme (Barker and Freund 1996).

In this aspect BFR-RC already has the best axial ligand, and replacing Met with His in BRF-RC would likely shift the potential down.

A large fraction of the E_m decrease observed in BFR-RC comes from interaction with the two Asp23 residues. Interestingly, this polar aminoacid is located in the hydrophobic region of the $ZnCe_6$ binding pocket. In addition, this aminoacid is conserved among ferritins from several organisms (PDB ID: 2FKZ, 3E1M, 3IS8, 3FVB) suggesting that it serves to regulate heme potential. Replacing it with an aliphatic residue is expected to eliminate this negative effect. Another potential modification is replacement of Asp50. In native BFR Asp50 forms a salt bridge with Lys53. Replacement of Asp50 with a polar or even basic aminoacid would break this salt bridge without affecting the interaction between the two monomers. This would facilitate the interaction of Lys53 with the carboxylic acids of $ZnCe_6$ potentially neutralizing the effect of their negative charge.

4.5. CONCLUSION

In summary we have determined a number of protein structural factors contributing to the redox potential of $ZnCe_6$ in BFR-RC, and by emulating some of the features of PSII it may be possible to raise the potential by several hundred millivolts, but not likely all the way up to the 1.2 V required to oxidize water. Hence efforts will focus on the use of entirely different pigments to $ZnCe_6$.

Chapter 5

Second generation of the Bacterioferritin 'reaction centre'

This manuscript is to be submitted to Biochemistry Journal

5.1. ABSTRACT

Photosystem II (PSII) of oxygenic photosynthesis has the unique ability to photochemically oxidize water and evolve oxygen. In 2009, an engineered Bacterioferritin photochemical 'reaction center' (BFR-RC) using a zinc chlorin pigment (ZnCe6) in place of the native heme was suggested to oxidize a bound manganese (II) ion through a tyrosine residue, thus mimicking two of the key reactions on the donor side of PSII. However, tyrosine oxidation was observed only in presence of manganese (II) ion. Recently the ability of $ZnCe_6$ to oxidize tyrosine efficiently has been questioned due to the low oxidation potential of $ZnCe_6$ (640mV) (See chapter 4) . In order to develop more robust BFR reaction centre capable of oxidizing tyrosine and the manganese cluster efficiently, we proposed using phosphorus porphyrin pigment instead of $ZnCe_6$. We aimed at oxidizing a tyrosine residue in the absence of the manganese cluster using this protein-phosphorous pigment complex. The phosphorus pigment was cross-linked to BFR-RC through two cysteine residues axially, we call this arrangement the second generation of the Bacterioferritin 'reaction centre' BFR-RC2. Fluorescence decay kinetics studies suggest that charge separation is occurring in BFR-RC2. Transient and CW-EPR data suggests that in the absence of the manganese cluster, the pigment oxidizes a tyrosine residue forming a radical pair in which the triplet state of the pigment dominates. Additionally, photochemical reduction of NAD using this 'reaction centre' was observed.

5.2. INTRODUCTION

The goal of artificial photochemical water oxidation is of great interest to creating a carbon neutral source of fuels (Gust, Moore, and Moore 2009). Photosystem II has the unique ability to extract electrons from water, by oxidizing water into oxygen gas (Barber 2003). This is a four electron oxidation reaction and is primarily driven by the high oxidation of the P680 radical (Ishikita et al. 2005). This potential is accepted to be nearly 1.2V and is the highest oxidation potential in nature (Barber 2003). It is through this pigment that nature couples the one electron reactions of photo-induced radical pair formations to the four electron oxidation of water. This coupling is done through the Kok cycle (Kok, Forbush, and McGloin 1970). P680 is a chlorophyll *a* dimer in the case of cyanobacteria, chlorophyll *a* has an oxidation potential of ~700mV in polar organic solvents (Hasegawa and Noguchi 2005). The high oxidation of P680 is primarily due to the highly hydrophobic environment of the P680 site in PSII and the polarization effect due to the protein backbone (Ishikita, Saenger, Biesiadka, et al. 2006). The high oxidation potential of P680, which allows such coupling of photochemistry to oxidation of water may be used to develop a system in which water oxidation can be coupled to CO_2 reduction for the purpose of Solar Fuel production. The use of PSII in such a system is complicated by PSII's instability in solution environments and the fact that it is prone to damage (Cardona et al. 2012). The di-Manganese cluster of Mn-Catalase has been shown to be a good mimic of the environment and reactions of the oxygen evolving complex of PSII (McConnell et al. 2012). Bacterioferritin is a protein known for its resistance to

oxidative damage and stability in solution (Carrondo 2003). It has a promiscuous di-metal binding site, which can be turned into a di-Mn cluster (Janowski, Auerbach-Nevo, and Weiss 2008). Previously, a Bacterioferritin 'reaction centre' (BFR-RC) was constructed by replacing the Heme b with an artificial pigment known as $ZnCe_6$ and binding two Mn ions in place of the natural di-iron cluster (Conlan et al. 2009). This attempt was a very attractive option for water oxidation in a stable and easily produced engineered protein system. Moreover, the authors were able to observe oxidation of the Mn-cluster from the Mn^{II}-Mn^{II} to Mn^{III}-Mn^{III}. If this engineered system is to function as an artificial Photosystem II, it should have a high oxidation pigment to drive the oxidations of the Mn cluster. We set out to determine the oxidation potential of $ZnCe_6$ in solution and in the engineered protein system (Mahboob et al. 2013) found in **chapter 4**. It was found the oxidation potential of $ZncCe_6$ inside BFR-RC is in the range of 600mV making it below the required potential to oxidize water (820mV) and very far from the likely needed 1.2V of P680 to drive the reaction forward. It was also found that the BFR-RC protein environment does not upshift the $ZnCe_6$ by a significant amount (Mahboob et al. 2013). This finding suggests that the use of point mutants to increase the potential of $ZnCe_6$ in BFR-RC would not be a fruitful avenue. Instead, pigments with a high oxidation potential in solution should be used. Hypervalent Phosphorous porphyrins have oxidation potentials near 1.4V in organic solutions (Akiba et al. 2001) partially due to the pre-existing positive charge on the Phosphorous atom and the none-planar nature of the macrocycle. These hypervalent Phosphorous porphyrins have been previously investigated in chemical donor-acceptor complexes. (Poddutoori et al. 2010). In this study, we aim to chemically-link a mutant form of Bacterioferritin to a hypervalent

Phosphrous Octaethylporphyrin and examine the properties of the ‘reaction centre’ known as the Bacterioferritin Reaction Centre Second Generation (BFR-RC2) using a combination of EPR and optical spectroscopy techniques.

Electron Paramagnetic Resonance (EPR) is the method of choice for studying paramagnetic intermediates in photosynthetic reactions. The photo-induced trapped radicals give rise to signals that can be used to identify the character of the radical. These trapped radicals are characterized by the g factor (Lubitz, Lendzian, and Bittl 2002). In low-field EPR, most organic radicals give a g factor in the vicinity of 2.00. The use of higher field EPR instruments can allow distinguishing different organic radicals by g factors. In the case of generating a triplet state, or a bi-radical, electron-electron interactions can give rise to Zero Field Splitting (ZFS). ZFS parameters are obtained from the EPR spectra, they are known as the axial and none-axial parameters, D and E respectively:

Equation 1:

$$\square = \frac{3}{4}(\square\square)^2 \langle \frac{\square_{12}^2 - 3\square_{12}^2}{\square_{12}^5} \rangle$$

Equation 2:

$$\square = \frac{3}{4}(\square\square)^2 \langle \frac{\square_{12}^2 - \square_{12}^2}{\square_{12}^5} \rangle$$

The angular brackets signify averaging over the wavefunction, gβ is the gyromagnetic ratio of spins: β is the Bohr magneton, g-factor is a dimensionless quantity which characterizes the magnetic moment and gyromagnetic ratio of a particle (electron in this

case), g factors can be determined for a single electron from quantum electrodynamics, and r_{12} is the vector in Cartesian space joining the spins. The z-axis is the normal axis.

In the case of triplet states, the ZFS contain information regarding the delocalization of the unpaired electron. In the case of biradicals and radical pairs, the ZFS gives information regarding the distance and the relative orientation of the radicals to each other. This is because in planar organic molecules such as porphyrins and chlorins, the z-axis is the normal. In other words, $\langle \square_{12}^2 \rangle << \langle \square_{12}^2 \rangle, \langle \square_{12}^2 \rangle$. The consequence is that D becomes positive. The dependence of D on the distance between the spins is inferred from the equation 1 as $1/r^3$. So the value of D can help determine the distance between the two species involved in the radical pair. On the other hand, the value of E indicates the plane symmetry with regards to the electron distribution.

An interesting example regarding the use of ZFS to characterize photo-induced triplet states comes from the work of Sieckmann (Sieckmann and Brettel 1993). In Sieckmann *et al.*, the authors performed a time-resolved EPR analysis of the P700 triplet state of Photosystem I at room temperature. It was previously known that the low-temperature data were consistent with a monomer chlorophyll triplet state (Rutherford and Mullet 1981). On the other hand, D and E parameters taken from the EPR spectra on Bacterial reaction centre (BRC), have shown a scenario consistent with a dimeric triplet state. The D and E values obtained from low-temperature EPR spectra of the BRC are smaller than the values obtained from the low-temperature EPR data on P700. Generating an admixture of the charge transfer states will cause the r value to increase, hence giving rise

to lower D and E parameters. Delocalization of the triplet state will also give rise to lower D and E parameters. If one assumes that the excitation leading to the triplet state hops incoherently between the two chlorophylls, the ZFS parameters are dictated by the average ZFS tensors of both triplets. Alternatively, the triplet state is a coherent superposition of the two individual chlorophyll triplet states. In either case, the ZFS parameters will be lowered. While the low-temperature data for P700 suggest a monomeric chlorophyll triplet state, the room-temperature data shows a 49% decrease in the E value while the D value remains unchanged from low-temperature spectra. In other words, admixture charge transfer states are not in effect as they would change the D value. E value reduction indicates that the distribution of the radical has changed towards a more delocalized environment.

As seen in equations 1 and 2, one can make use of the D and E parameters to arrive at the distance (r). The dependence of D on the distance is $1/r^3$, making the elucidation of the distance between spins very sensitive to the changes in the D and E parameters. However, as seen above, the analysis of D and E in natural Photosystems is complicated by the fact that all primary donors are in dimeric form, which influences the spectra and affects D and E values. As discussed above, this influence can be temperature dependent as well. In our system of interest, BFR-RC, the primary donor is a single Phosphorous pigment, removing this complication of the analysis. The simplest relationship between the radical pair spectra and the ZFS parameters D and E is that the width of the spectra is 2D. However, this relationship only holds true if the axial parameter (D) is much higher than the difference in the g values.

5.3 METHODS

5.3.1 Synthesis of pigment and BFR-RC2 assembly

Preparation of dichloro Phosphorous(V) octaethylporphyrin was done using a modified version of the procedure by Akiba and co-workers(Akiba et al. 2001). In short, 50mg of $(OEP)H_2$ was dissolved in dry DCM (15mL). PCl_3 was added and the solution was stirred for 2 days under N_2 at room temperature. The reaction was stopped by the addition of water:DCM in 1:1 ratio, acidic workup using 1M HCl was performed and the solution was bright pink. Extraction, removal of solvent and purification by chromatography (DCM/Methanol 9:1) afforded the $[P(OEP)Cl_2]^+Cl^-$. In order to confirm the formation of the dichloro product, P^{31} NMR was taken and a δ of -230ppm **APPENDIX III**-Figure 1 was obtained in agreement with the formation of $[P(OEP)Cl_2]^+Cl^-$ reported previously (Akiba et al. 2001). Moreover, proton NMR of the starting material and product shows the disappearance of the δ -2.8 indicative of the N-H protons **APPENDIX III** – Figure 2,3.

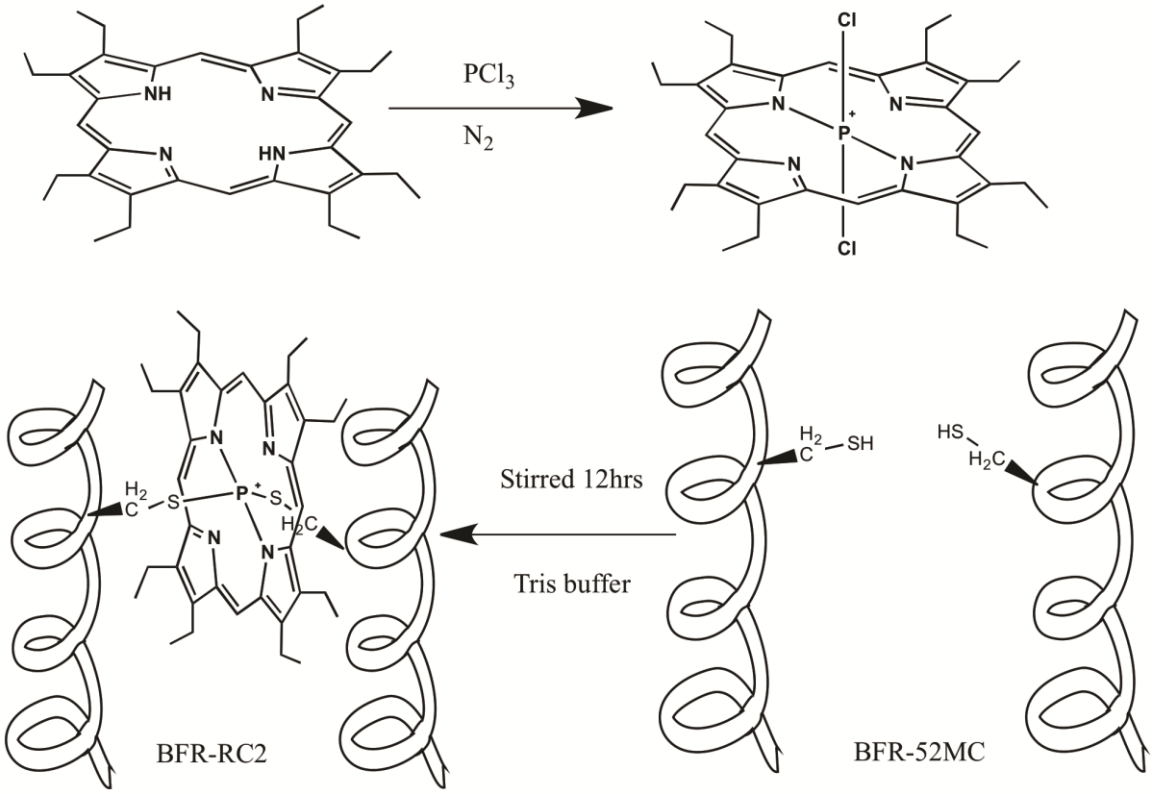

Figure 5.1. Reaction to form the $[P(OEP)Cl_2]^+Cl^-$ pigment, followed by reaction with BFR-52MC mutant to form BFR-RC2

BFR-52MC mutant protein was kindly provided by Dr. Nick LeBrun (University of East Anglia). BFR-52MC was dissolved in 0.05 Tris buffer pH 7.0 and in a mixture of DMSO:Tris Buffer 50/50 in two independent attempts at reaction. With respect to reaction in aqeous solution, a 1:2 molar equivalents with respect to protein of $[P(OEP)Cl_2]^+Cl^-$ was dissolved in a small amount of DMSO and then dissolved in Tris buffer. It was slowly added over a period of 12 hours at room temperature while stirring. In the case of 1:1 DMSO:Tris reaction, protein and pigment were dissolved in the same solution, and pigment added over 12 hours to the protein. Size exclusion column

(Amicon 15kDa) was used to isolate the protein from the unbound pigment. The synthesis of the pigment and the assembly of the BFR-RC2 are summarized in figure 5.1. An SDS-PAGE gel was run to show whether or not a dimer can be formed from the protein-pigment reaction.

5.3.2 Optical spectroscopy measurements

Steady state absorbance UV-vis spectra were recorded with a Thermo Spectronic/Unicam UV-4 UV-vis spectrometer. A time-correlated single photon counting apparatus utilizing a picosecond pulsed diode laser was used to measure the porphyrin fluorescence decays. Excitation pulses were delivered at 420 nm by a picosecond diode laser (PicoQuant, PDL 800-B). The porphyrin fluorescence was measured by a Hamamatsu R-3809 micro channel plate photomultiplier screened by a double monochromator as reported previously (Poddutoori et al. 2010).

5.3.3 EPR measurements

Freeze-trapping EPR spectra were recorded using a Bruker Elexsys E580 pulse spectrometer operating in CW mode. The temperature was controlled using a Bruker VT 1000 temperature control system. Transient EPR time/field data sets were recorded using a modified Bruker EPR 200D-SRC X-band spectrometer equipped with a Flexline dielectric resonator and a liquid Nitrogen cryostat. Optical excitation at 532 nm was achieved using 10 ns pulses from a Continuum Surelite Nd:YAG laser at a repetition rate of 22 Hz.

5.4 RESULTS

5.4.1 Characterization of $[P(OEP)Cl_2]^+Cl^-$

The formation of the pigment was confirmed by using UV-VIS spectroscopy, along with ^{31}P, ^{13}C, and ^{1}H NMR. Proton NMR showed disappearance of the Hydride signal from the freebase pigment in the product, while ^{31}P NMR showed the characteristic δ -230 indicative of dichloro high valence Phosphorous (Akiba et al. 2001). The UV-VIS spectrum is shown in figure 5.2. The freebase pigment, which was used as the starting material has two protons that appear in Hydride NMR. The UV-VIS spectrum of freebase porphyrins has long been understood in terms of the Martin Gouterman model proposed in 1959 (Gouterman, Wagnière, and Snyder 1963). The model states that the spectrum can be explained by transitions between four orbitals (HOMO-1, HOMO, LUMO, LUMO+1). The symmetry of the transitions is changed upon the introduction of the central Phosphorous atom. This change in symmetry of the molecule and causes two of the four energy transitions to become degenerate, giving rise to only two Q bands in the dichloro product as opposed to four in the freebase.

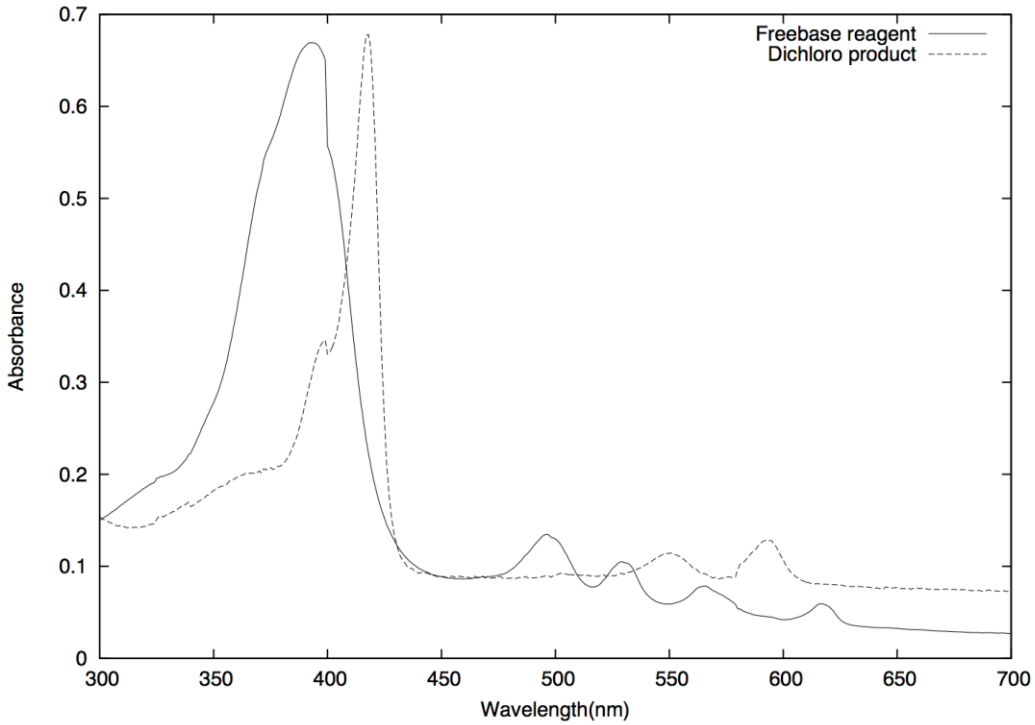

Figure 5.2. UV-VIS of starting material (Octaethylporphyrin free base shown in solid line) and dichloro product (dashed line)

The proton NMR of the freebase octaethylporphyrin pigment shows a peak at δ -2.9. The peak corresponds to the pyrole protons (Minnetun and Abraham 1984). Upon reaction with PCl_3, this peak disappears. Moreover, the dark pink-coloured dichloro product shows only two Q bands in UV-Vis as opposed to four (Figure 5.2).

5.4.2 Crosslinking $[P(OEP)Cl_2]^+Cl^-$ to BFR-52MC

As show in figure 5.1, the pigment should bind to the cysteine residues found on each monomer at the dimer interface of BFR-52MC mutant. The reaction is possible because of the electron withdrawing nature of chlorine atoms connected to the central phosphorous atom of $P(OEP)Cl_2$ makes the phosphorous-chlorine bond easily accessible. In this case, the sulfur atom of cysteine 52 acts as a nucleophile and the chlorine acts as a leaving group. If the reaction occurs, the pigment will be inserted at the dimer interface causing the formation of a dimer band on SDS-PAGE gel. This band should be resistant to DTT treatment as it is not formed by a disulfide bridge, but rather the thioether bond between the pigment and the protein. Figure 5.3 shows SDS-PAGE gel of BFR-52MC (A) and BFR-RC2 (B). BFR-RC2 is formed by the reaction described in Figure 5.1. The upper band in BFR-RC2 lane corresponds to the dimer weight of the BFR-52MC mutant, it is resistant to DTT treatment. Despite the fact that the cysteines on each monomer in the dimer face each other, they do not form a disulfide bridge. This is because the distance between them is too large for the formation of such a bond. The pigment, once inserted in the dimer interface, is likely at a good distance to form the thioether linkage shown in Figure 5.1. As shown in Figure 5.3, the monomeric band seems to be much more concentrated than the dimeric band, indicating that the reaction either does not progress to completion, or possibly that side-products exist in which the pigment reacts with the monomer form through another nucleophilic group such as phenol or alcohol.

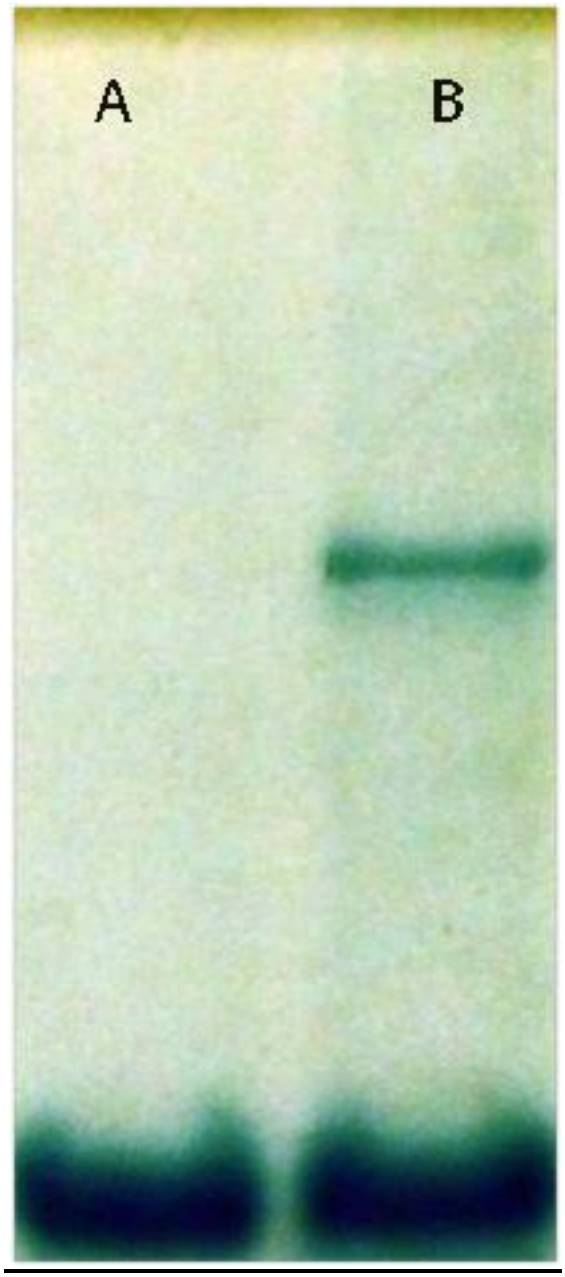

Figure 5.3. SDS-PAGE Gel of BFR-M52C (A) and BFR-RC2 assembled in 0.05 M pH 5.6 MES buffer (B)

When using buffers such as MES 5.6 and Tris pH 7, the washout from the size exclusion column contains unbound pigment as can be confirmed from UV-Vis. When compared to concentration of protein, the amount of unbound pigment in the washout solution indicates that the majority of the pigment did not react and hence in neutral to slightly acidic pH ranges, side reactions aren't very likely and the yield of dimeric BFR-RC2 is low. In order to solve this problem, slightly basic buffers and also a mix of DMSO/buffer was used. In this situation, no pigment is found in the washout; however, the SDS-PAGE gel has a band in the stacking gel, which fluoresces under blue LED light as shown in figure 5.4. This band is likely the product of protein aggregates in which the pigment acts as a cross-linking agent, creating very large protein aggregates that cannot enter the running gel.

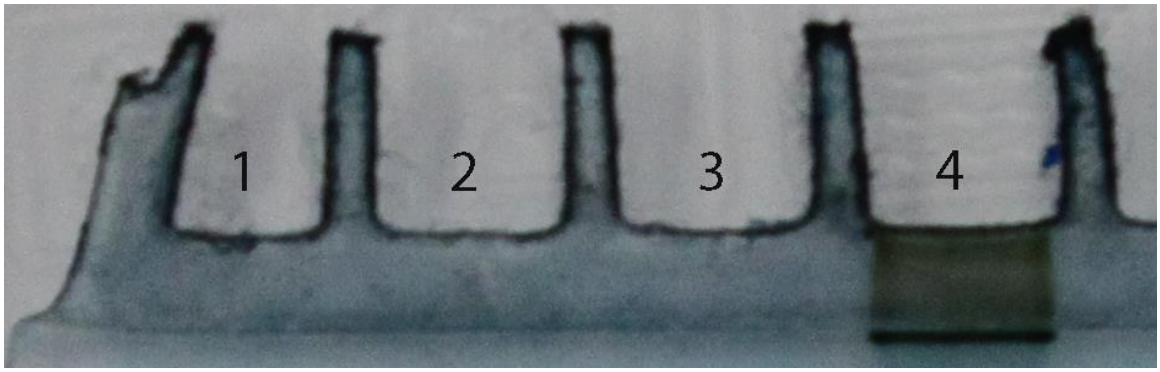

Figure 5.4. SDS-PAGE Gel showing top of lanes for ladder (1), BFR-M52C (2), BFR-RC2 assembled in MES 0.05 M pH 5.6 (3), and BFR-RC2 assembled in 50% DMSO: MES 0.05 M pH 5.6 (4). The band shown is aggregated protein that fluoresces under blue LED light

5.4.3 EPR measurements on BFR-RC2

CW-EPR was performed on samples of the BFR-RC2 at liquid nitrogen temperatures. Light minus dark spectra are shown in figure 5.5. Samples illuminated in room temperature and then frozen show a sharp line with width of approximately 5 Gauss, the samples frozen in darkness and illuminated in liquid nitrogen, show a spectrum that has a "shoulder" with a width of approximately 10 Gauss. In the former case, the sharp line likely corresponds to the porphyrin radical, which is caused by the reduction of the porphyrin. This spectrum is consistent with previously known spectra of hypervalent phosphorous porphyrins (Poddutoori et al. 2010). On the other hand, the shoulder shown in the spectrum of dark-frozen samples has the width of a tyrosyl radical. In BFR-RC (the first generation of the Bacterioferritin reaction centre), CW-EPR showing tyrosyl radicals had the same width (Hingorani et al. 2009). However, the lack of hyperfine features of the shoulder spectrum shown in figure 5.5 makes the assignment of the shoulder based on width alone to tyrosyl radical rather too optimistic! Repeating the experiment in higher field can provide some hyperfine features leading to a more confident assignment. Previously reported tyrosyl radical light-induced spectrum of Photosystem II took a shape similar to the shoulder spectrum reported here (Havelius and Styring 2007). The CW-EPR signal was much wider than observed here, which was attributed to the interaction with the manganese cluster of Photosystem II. BFR-RC2 samples examined in the CW-EPR spectra shown here do not have manganese clusters. Examination of the tyrosyl D radical of Photosystem II with CW-EPR, which resembles this situation as it has no Manganese cluster to interact with, shows a width of ~10Gauss appearing as a shoulder to the main signal. The main reason to suggest that the shoulder arises from a tyrosyl

radical remains the width of the signal. Because the results are unchanged regardless whether or not the samples are degassed, the involvement of oxygen reactive species in the formation of the shoulder or any parts of the spectrum for that matter is not likely.

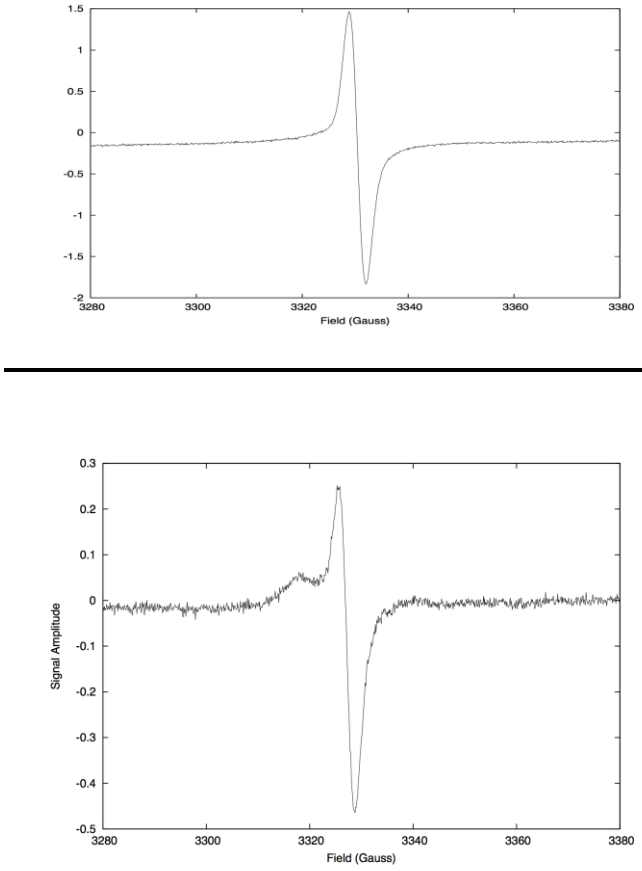

Figure 5.5. CW-EPR spectrum taken by illuminating in room temperature and frozen under illumination (top). CW-EPR spectrum taken by freezing in dark and illumination at 80K (bottom)

Tyrosine remains a good candidate for the shoulder observed due to the signal's width of 10Gauss. However, the signal is much smaller overall from the sharp line shown in top of

figure 5.5. Moreover, the shoulder cannot be photoaccumulated in low temperature illumination. It is likely that the potential tyrosyl radical is not very stable. TR-EPR spectrum in figure 5.6 shows both a triplet-dominated signal at low temperatures and a radical pair at room temperature. The radical pair and the triplet state-dominated spectrum are in agreement with observations in similar hypervalent phosphorous porphyrins (Poddutoori et al. 2010). The spectrum seen at liquid nitrogen temperature (80K), has a width of approximately 400 G, which is quite consistent with hypervalent phosphorous triplet state. In the middle of the spectrum is a smaller sharp line arising from a radical pair. At room temperature, this radical pair signal dominates. The TR-EPR shows unambiguously that charge separation occurs. The width of this radical pair spectrum is approximately 10G. Such a narrow spectrum could imply that the radical pair is strongly coupled (Jakob et al. 2006). One interesting feature regarding the shape of the radical pair spectrum seen at room temperature is that the emissive and the absorptive parts of the spectrum are not equal. An explanation for this could be that the triplet state gives rise to radical pair. In other words, charge separation occurs from the triplet state of the porphyrin and not the singlet. This is further supported by the fact that at 80K, the sharp signal representing the radical pair appears more clearly later, after the initial triplet state signal has been observed.

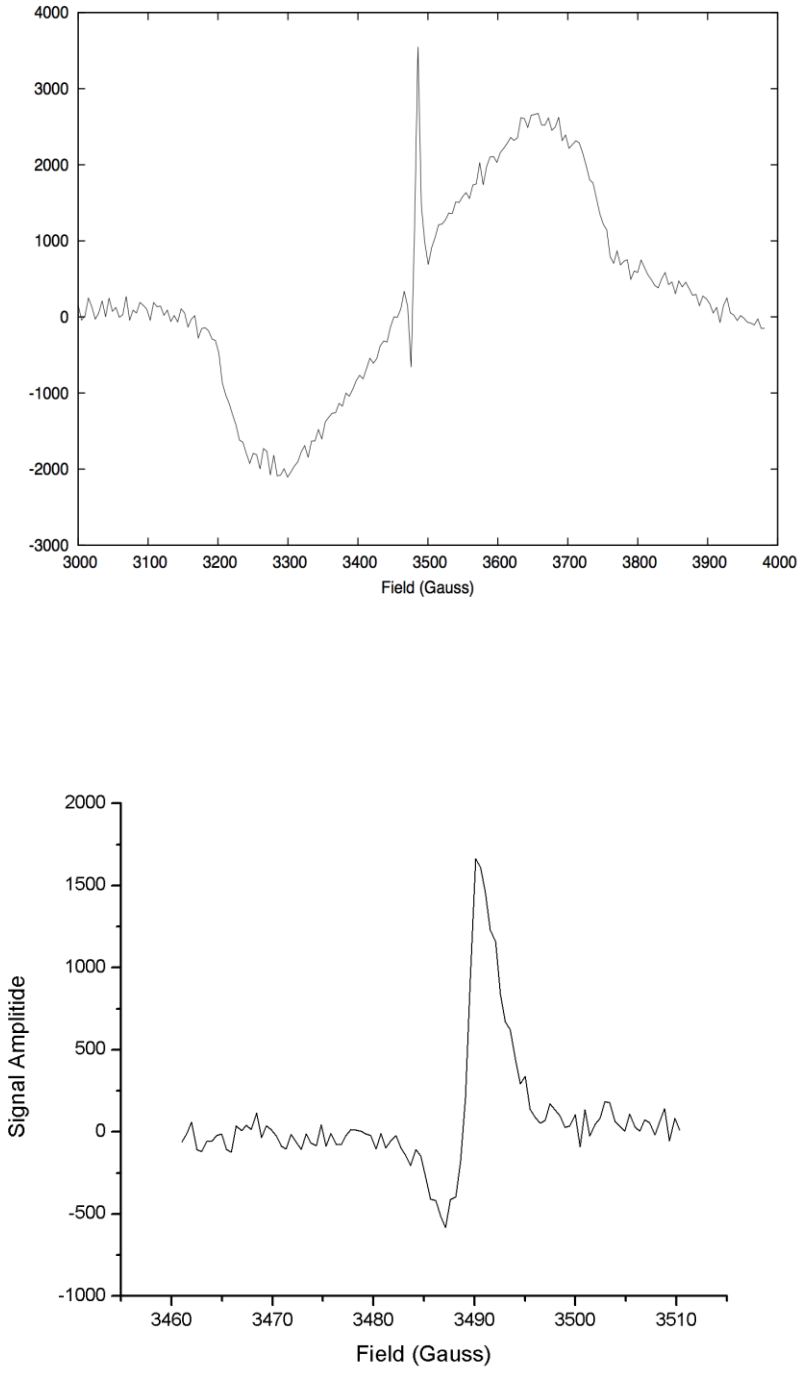

Figure 5.6. Transient EPR taken at 100K (top). Transient EPR taken at room temperature (bottom)

An interesting question arises from TR-EPR data, what is the partner for the phosphorous porphyrin in the radical pair signal? In other words, it is easy to say with confidence that the porphyrin is involved in this radical pair. The radical pair is photoinduced and the low temperature spectrum clearly is dominated by a triplet state signal consistent with such hypervalent phosphorous porphyrins (Poddutoori et al. 2010). However, assigning the partner to the porphyrin in the radical pair is far less trivial. We could start by assuming that the assignment of the shoulder CW-EPR to a tyrosine is correct due to its width. One would then need to know which tyrosine. In BFR-RC, mutants of each possible tyrosine to phenylalanine were needed to examine which mutant would cause a change in the CW-EPR. Similarly, mutants of each tyrosine can be made in this case and TR-EPR done on each mutant. This is a future project currently being planned with collaborators at East Anglia. The measurements of the distance between the two electron spins have been possible in similar situations of light-induced radical pairs through analysis of an out-of-phase echo. Unfortunately, these samples do not have an out-of-phase echo.

5.4.4 Fluorescence Decay kinetics

The time-limit for detecting light-induced radical pairs in EPR is limited to events happening on a time-scale slower than 30ns. In order to observe events happening on faster time-scales, fluorescence decay kinetics measurements have been employed. Figure 5.7 shows the fluorescence decay of the pigment in solution (POEP in DMSO) and of BFR-RC2. The fluorescence decay is that of the porphyrin. The pigment is excited at a wavelength of 420 nm (Soret band) and the decay is monitored at 600nm.

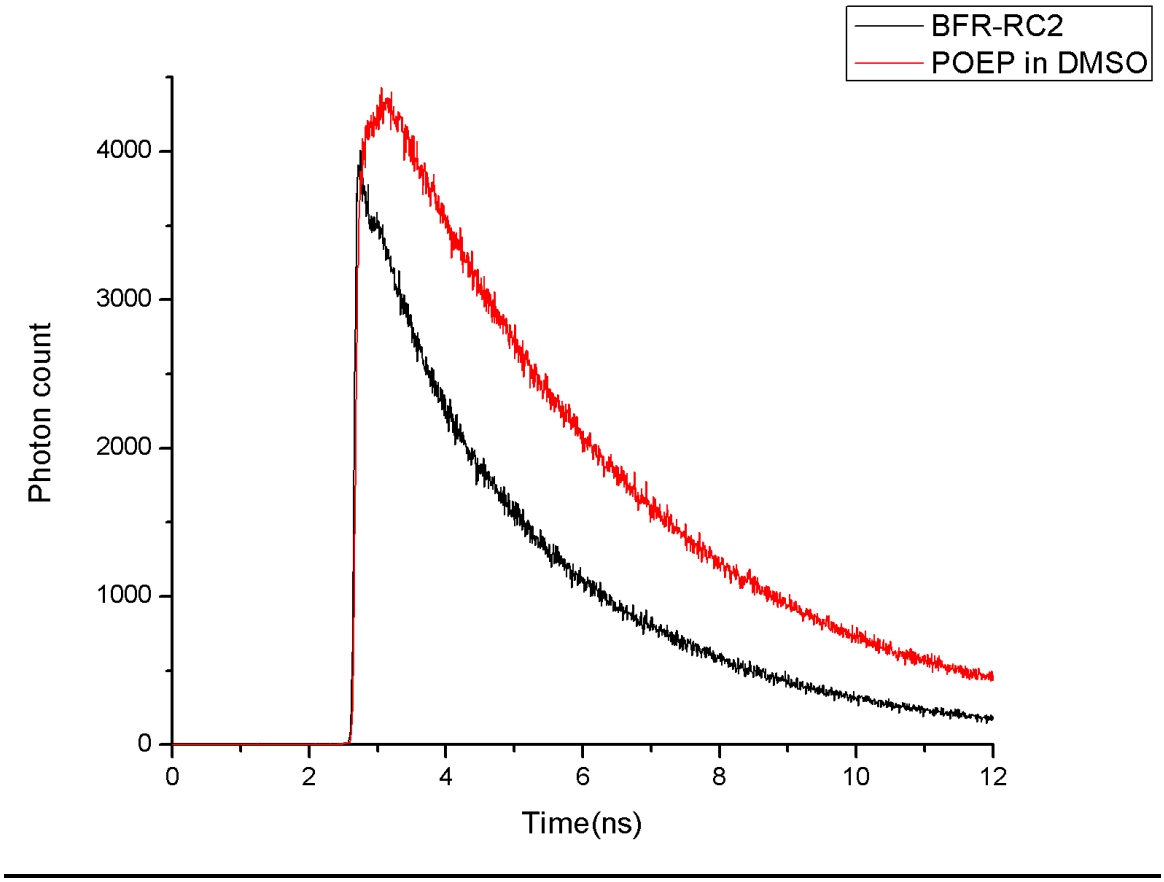

Figure 5.7. Fluorescence decay kinetics at room temperature for pigment in DMSO and pigment-protein complex

Table 5.1. Fitting of decay lifetimes for $[P(OEP)Cl_2]^+Cl^-$ in solution (POEP-DMSO) and for the Bacterioferritin Second Generation 'reaction centre' BFR-RC2. For residual of fits please see **APPENDIX IV**

	Number of components	τ(ns)	X^2	Normalized yield	Amplitude
POEP-DMSO	1	3.875	1.04	3.87	1
BFR-RC2	2	τ_1=0.517	1.25	1.30	A1=0.743
		τ_2=3.245			A2=0.257

The data was fitted using in-house fitting software. Results of the fits are shown in Table 5.1. The pigment in solution POEP-DMSO decays with a lifetime of 3.9ns. This lifetime is typical of similar phosphorous porphyrins. In BFR-RC2, the pigment decays with two lifetimes: one at 3.2ns and another, at a much shorter lifetime of 0.5ns. Based upon the amplitudes, the shorter lifetime contributes approximately 70% of the decay. The normalized fluorescence yield is much smaller in the protein than in the pigment in solution. Taken together, these results reinforce the TR-EPR data of the presence of a singlet electron transfer causing a radical pair (seen as the shorter lifetime). The fact that the number of components required to fit the decay profile for BFR-RC2 is two indicates that there are likely two events happening. One event is likely the decay of the pigment itself, which happens at the lifetime of 3.2 ns. The shorter lifetime is explained by considering Kasha's rule regarding the transitions causing the fluorescence. Fluorescence

is caused by the transition from s1 to s0. The loss of the excited state occurs through the an electron transfer event, making the relaxation from s1 back to s0 not possible.

5.4.5 Reduction of NAD by BFR-RC2

So far, results have shown that BFR-RC2 does perform charge separation and might be able to create a radical pair that involves the porphyrin and likely a tyrosine. In order for this system to be eventually used in the solar production of alcohols and another oxygenated fuels from CO_2, one needs to show that it can also reduce cofactors. In the enzymatic synthesis of alcohol from CO_2, three enzymes have been used: Formate Dehydrogeanse (FDH), Aldehyde Dehydrogenase (AlDH), and Alcohol Dehydrogeanse (ADH), (Jiang et al. 2002). Each of these three enzymes requires the reduction of CO_2, Formate, and Formaldehyde respectively, to be coupled to the oxidation of one NADH to NAD^+. Thus, one approach to the photochemical production of methanol from CO_2 can be achieved by the photochemical generation of NADH from NAD^+ since it will provide a continuous pool of NADH to be used in the reduction reactions described above. Illumination at room temperature of a of BFR-RC2, in a solution with NAD^+/NADH mixture shows an increase to the 320 nm peak corresponding to NADH as seen in figure 5.8.

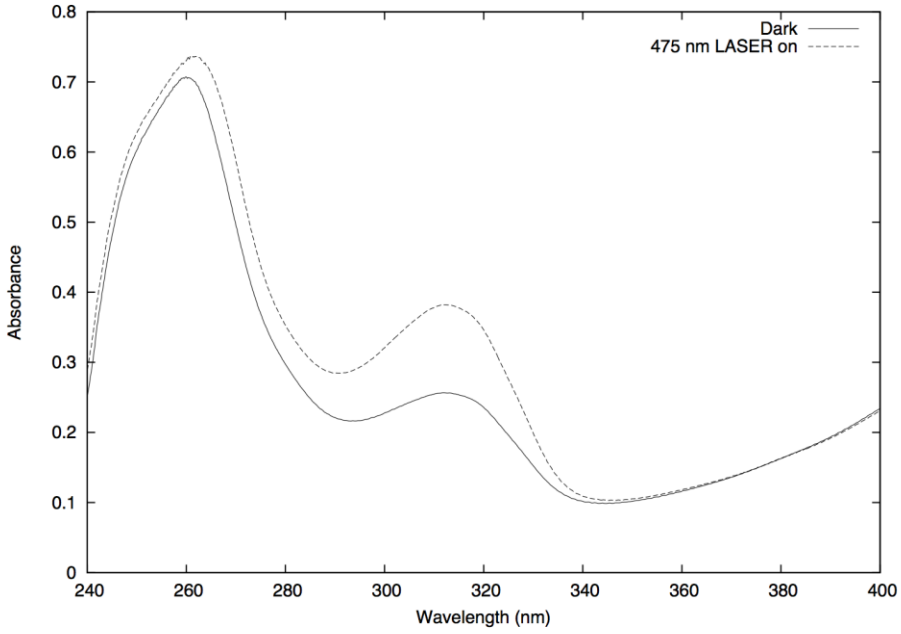

Figure 5.8. Photochemical reduction of NAD^+ through a brief 475nm LASER illumination of BFR-RC2:NAD^+/NADH mixture

The illumination was done using a 475 nm LASER. Similar results are seen with a blue light LED illumination and with white light illumination. However, a control in which NAD^+/NADH is present without the BFR-RC2 shows no such results. The spectrum remains the same before and after the illumination.

5.5. CONCLUSIONS

It is clear that BFR-RC2 is capable of forming light-induced radical pairs as clearly seen from TR-EPR and implied from fluorescence decay kinetics. The evidence suggests that the porphyrin is involved in this radical pair, likely giving rise to the radical pair observed in TR-EPR from its triplet state. The identity of the partner of this radical pair is less clear. From low-temperature CW-EPR measurements, it is possible that the partner is a tyrosyl radical. However, the efficiency of this process is not likely to be high. Point mutations of suspected tyrosines are likely needed to help with the assignment. Also, Transient Absorbance at wavelengths characteristic of suspected radicals (tyrosine or tryptophan) could help shed light on the mechanism of the charge separation mechanism. These measurements are currently being planned. It has been shown in this chapter that one can reduce NAD^+ using BFR-RC2. The question becomes, can we make BFR-RC2 work in tandem with other proteins to perform photochemical CO_2-fixing. This is long-term project that is of great interest (see **Chapter 6**).

Chapter 6

Future directions: The coupling of water oxidation to CO_2 reduction

Converting solar energy into chemical bonds of fuels could provide a solution to the challenges of a post-oil economy. Oxygenic photosynthesis achieves this task in plants, algae, and cyanobacteria through a series of light-activated redox reactions that result in the splitting of water to protons and oxygen gas. The protons are used ultimately to drive the synthesis of ATP. Moreover, CO_2 is reduced and incorporated into sugar molecules in a series of biochemical transformations known as the dark reactions (Nelson and Ben-Shem 2004). A protein network in which water oxidation is coupled to CO_2 reduction in a photocatalytic manner would provide a novel source of fuel. The next step of this research should aim at developing such a system.

Water oxidation occurs in PSII, a large protein system that is unstable in solution. PSII houses an organometallic catalytic center known as the Oxygen Evolving Complex (OEC). The OEC acts to accumulate oxidation potential on manganese metal centers and eventually oxidizes water to oxygen. Stable protein scaffolds containing di-manganese centers can be used to reverse engineer PSII as seen with preliminary results shown in chapter 4. The electrons taken out of water through the di-Manganese center can be shuttled to a second enzyme, Formate Dehydrogenase (FDH), which has been shown to reduce CO_2 to formic acid (a liquid fuel). Such coupled catalysis networks would constitute a novel platform for artificial photosynthesis that can produce a liquid, carbon neutral fuel, since formic acid burns in oxygen to give off CO_2.

The future work has three main stages:

(1) Development of water oxidizing engineered small protein systems

(2) Development of a CO_2 reducing FDH

(3) Linking the products from (1) to the product from (2) towards a liquid fuel producing, artificial electron transport network

In 2009, Dr. Wydrzynsky's group at the Australian National University reported that an engineered form of the *E. coli* iron storage Bacterioferritin (BFR) protein, is capable of oxidizing a protein-bound di-Manganese cluster. The protein was also able to oxidize a tyrosine residue. Both oxidations were linked to the oxidation of a photoactive pigment known as $ZnCe_6$ (Conlan et al. 2009). BFR is a good mimic of PSII since the oxidation of water in PSII occurs through a water-binding manganese cluster and a tyrosine residue, creating an electron flow from water. The electron flow in PSII is paralleled in this engineered BFR 'reaction centre', (BFR-RC). Computer simulations and experiments presented in this thesis (**Chapter 4**) show that while $ZnCe_6$ might be able to perform one oxidation of the di-manganese cluster, it does not possess the necessary oxidizing power for the subsequent oxidations that are required to fully oxidize water to oxygen (Mahboob et al. 2013). In PSII, the manganese cluster is oxidized four times to yield oxygen gas. The oxidation of water is driven primarily by the high oxidation potential of a dimeric pigment known as P680. P680 has an oxidation potential of ~1200mV while BFR-RC's pigment ($ZnCe_6$) was found to have an oxidation potential of only 618mV.

In **Chapter 5**, a second generation of the Bacterioferritin 'reaction centre' was built using a phosphorous porphyrin pigment capable of binding to BFR-RC with an oxidation potential near that of P680. The high potential of P680 is not the only requirement to successful photooxidation. It has been shown that pigment binds covalently at the dimer interface of the BFR-RC2. Photooxidation is done through a process of generating progressively distant radical pairs known as charge separation. The more distance between the components of the radical pair, the more stable it is. Part of this stabilization is due to the protein's reaction to accommodate the emerging charges in the form of radical anions and cations as presented with respect to PSII in **Chapter 2**. A major limitation to the success of photocatalytic electron transfer in engineered small peptides is the lack of distance inside the scaffold, which creates far less stable radical pairs. Just as the problem of oxidation potential in BFR-RC was solved by using a pigment with a high oxidation potential, the problem of stabilization is also solved by the use of this Phosphorous pigment, which due to the high valence phosphorous central atom has a positive charge, causing a high enough oxidation potential to abstract an electron from a tyrosine. The stability of the resulting radical pair; however, would depend on the distance. The phosphorous pigment cross-linked to a small peptide ensures that both the charge separation and the protein scaffold are stable. Both TR-EPR and CW-EPR evidence demonstrate that BFR-RC2 has a light induced radical pair which is relatively stable at room temperature and CW-EPR gives some indications that the partner of the phosphorous porphyrin might be a tyrosyl radical.

Cross-linking the pigment was done by mutating two methionine residues to cysteine residues with help from collaborators at the University of East Anglia. The two cysteine residues are to be cross-linked to the pigment in an axial manner. Having a high oxidation and stable charge separation are but only two requirements to achieve photocatalytic water oxidation. The di-manganese cluster needs to have the correct electronic and electrostatic environments. The planned work will begin by comparing the BFR-RC di-manganese cluster to organometallic model systems consisting of di-manganese clusters and natural di-manganese clusters of Mn-Catalase, through DFT computations and Poisson-Boltzmann numerical solvers. The results can shed light on what mutations can be made in the vicinity of the di-manganese cluster of BFR-RC system to allow it to perform catalytic water oxidation.

DFT will be combined with EPR techniques to determine the catalytic mechanism of water oxidation within the BFR-RC2 system, while using previously proposed mechanisms of model di-manganese clusters as guidelines (Parent, Crabtree, and Brudvig 2013). Difference FT-IR spectroscopy will also be used to match DFT models by comparing vibrations in DFT calculations to those in the spectrum. Such comparisons can reveal structural details such as the presence of μ-oxo bonds in higher oxidation states, which are known to occur in model organometallic complexes, in Mn-Catalase, and most importantly in the OEC.

As an alternative to BFR-RC, the pigment will be cross-linked to a mutant form of Mn-catalase with a surface cysteine residue. Previous research work has shown that Mn-

catalase in its Mn^{III}-Mn^{IV} state is a good mimic of PSII's OEC (McConnell et al. 2012). While previous work has focused on using chemical oxidants, this research will use a phosphorous porphyrin cross-linked pigment with a high oxidation potential to accumulate higher oxidation on the di-manganese cluster of Mn-catalase. The di-Manganese cluster will be examined using EPR and difference FT-IR spectroscopy. Spectra will be compared to DFT models. It may be possible for this engineered Mn-catalase to perform catalytic water oxidation since it will have both a high oxidizing pigment and a tyrosine residue near the di-manganese cluster.

There is no good chemical reason why Mn should be used as a metal for water oxidation, indeed many researchers have used Ru and Ir complexes to oxidize water through organometallic complexes (Hetterscheid and Reek 2011). Replacement of the Mn with Ru and Ir inside the di-Manganese centers of BFR-RC and of Mn-Catalse can be done to examine the effects of the metal itself on the water oxidation. The Ru and Ir protein centers will be all examined using spectroscopic methods and results will be interpreted with the help of computational methods. The goal of full catalytic water oxidation within BFR-RC2 would constitute first stage of this project.

The electrons from the oxidized water need to flow to a second catalytic system that can reduce CO_2, turning it into a liquid fuel in the form of formic acid. In nature, carbon fixing is used to generate sugar molecules. Sugar molecules do not make good fuel for car engines! FDH oxidizes formate to CO_2. The second stage of the program will make use of DFT calculations and Poisson-Boltzmann calculations to design single point

mutations that can allow optimization of the reverse reaction in FDH. The mutations should allow for the conversion of CO_2 to formate. The proposed approach is a form of directed evolution guided by simulations. Both DFT and Poisson-Boltzmann calculations will serve to examine mutants that can increase the binding affinity of CO_2 while reducing the binding affinity of formate. In nature, enzymes evolve to bind the Transition State (TS), while having less affinity to the reactants and much less affinity to the product (to allow the product to exit the catalytic site). Previous research on examining and designing point mutants aided by computer simulations has shown how FDH can accept ligands different from formate (Hoelsch et al. 2012). The same principle can be used to weaken formate binding while strengthening CO_2 binding to optimize the process of Carbon Fixing. The combination of DFT and electrostatic calculations to guide point mutation work has been used in my PhD research in the case of BFR-RC2. It shows promise as a novel and exciting approach to protein design.

In the third and last stage of the program, engineered FDH can then be cross-linked to BFR-RC through either an electron wire or a polypeptide chain (Figure 6.1). Similarly, engineered Mn-catalase can be also crosslinked to FDH.

The culmination of this work may be the first example of a complete human-made protein photosynthetic electron transport chain! It will consist of a water-splitting side and a carbon fixing side. The eventual goal of the proposed experiments and approaches above is to develop a system that will use up water and CO_2 and give off formic acid (liquid fuel) as product, along with oxygen gas as a side product. So far, results have been

encouraging with regards to the use of computational techniques towards rational design of these protein systems. The above research project provides an industrially viable solution to a post-oil economy challenge: a solar liquid fuel through easily produced and stable engineered protein systems.

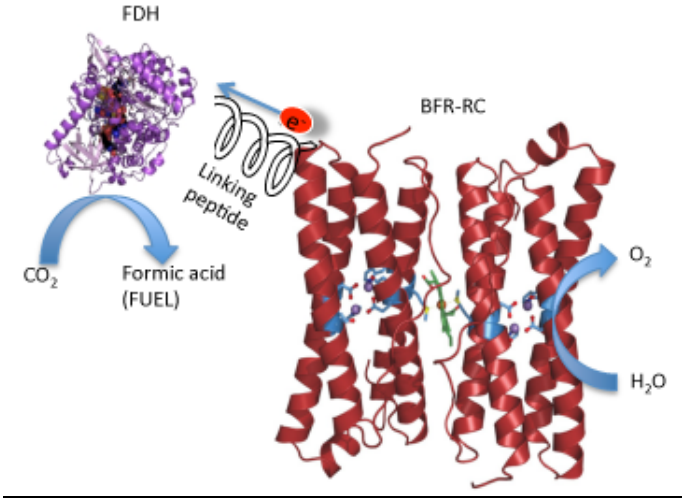

Figure 6.1. Schematic of the artificial photosynthesis system proposed: showing engineered Bacterioferriting 'reaction centre' (BFR-RC) where water oxidation occurs. Electrons then flow through a linking peptide to Formate Dehydrogenase (FDH) where CO_2 is reduced to formic acid.

APPENDICES

Appendix I. Protonation state changes with respect to charge separation steps (please see Table 2.1 for details).

Amino acid	State 1	State 2	State 3	State 4	State 5	State 6
GLU-A0015	-0.99	-1	-1	-1	-1	-1
ARG+A0016	1	1	1	1	1	1
CYS-A0018	0	0	0	0	0	0
ASP-A0025	-0.99	-0.97	-0.98	-0.97	-0.99	-0.97
ARG+A0027	1	1	1	1	1	1
TYR-A0029	0	0	0	0	0	0
CYS-A0047	0	0	0	0	0	0
ASP-A0059	-1	-1	-1	-1	-1	-1
ASP-A0061	-1	-1	-1	-1	-1	-1
ARG+A0064	1	1	1	1	1	1
GLU-A0065	-1	-1	-1	-1	-1	-1
TYR-A0073	0	0	0	0	0	0
HIS+A0092	0.97	0.97	0.96	0.93	0.93	0.94
TYR-A0094	0	0	0	0	0	0
GLU-A0098	-1	-0.99	-0.99	-1	-0.99	-0.99
ASP-A0103	-1	-1	-1	-1	-1	-1
GLU-A0104	-0.99	-1	-0.99	-1	-1	-1
TYR-A0107	0	0	0	0	0	0
TYR-A0112	0	0	0	0	0	0
HIS+A0118	0	0	0	0	0	0
CYS-A0125	0	0	0	0	0	0
TYR-A0126	0	0	0	0	0	0
ARG+A0129	1	1	1	1	1	1
GLU-A0132	-1	-1	-1	-1	-1	-1
TYR-A0135	0	0	0	0	0	0
ARG+A0136	1	1	1	1	1	1
ARG+A0140	1	1	1	1	1	1
CYS-A0144	0	0	0	0	0	0

TYR-A0147	0	0	0	0	0	0
TYR-A0161	0	0	0	0	0	0
ASP-A0170	-1	-1	-1	-1	-1	-1
GLU-A0189	0	0	0	0	0	0
HIS+A0190	0	0	0	0	0	0
HIS+A0195	0	0	0	0	0	0
HIS+A0198	0	0	0	0	0	0
CYS-A0212	0	0	0	0	0	0
HIS+A0215	0	0	0	0	0	0
ARG+A0225	1	1	1	1	1	1
GLU-A0226	-1	-1	-1	-1	-1	-1
GLU-A0229	-1	-1	-1	-1	-1	-1
GLU-A0231	-0.99	-0.99	-0.99	-0.99	-0.99	-0.99
TYR-A0235	0	0	0	0	0	0
TYR-A0237	0	0	0	0	0	0
LYS+A0238	1	1	1	1	1	1
GLU-A0242	-0.99	-0.99	-1	-1	-0.99	-0.99
GLU-A0243	-0.96	-0.95	-0.96	-0.96	-0.9	-0.95
GLU-A0244	-1	-1	-1	-1	-1	-1
TYR-A0246	0	0	0	0	0	0
HIS+A0252	0	0	0	0	0.16	0.1
TYR-A0254	0	0	0	0	0	0
ARG+A0257	1	1	1	1	1	1
TYR-A0262	0	0	0	0	0	0
ARG+A0269	1	1	1	1	1	1
HIS+A0272	0	0	0	0	0	0
HIS+A0304	0.05	0.04	0.03	0.01	0.04	0.03
ASP-A0308	-1	-1	-1	-1	-1	-1
LYS+A0310	1	1	1	1	1	1
ASP-A0319	-1	-1	-1	-1	-1	-1
ARG+A0323	1	1	1	1	1	1
GLU-A0329	-0.95	-0.96	-0.96	-0.97	-0.93	-0.97
HIS+A0332	0	0	0	0	0	0
GLU-A0333	0	0	0	0	0	0
ARG+A0334	1	1	1	1	1	1
HIS+A0337	0	0.04	0.03	0.04	0	0.03
ASP-A0342	-1	-1	-1	-1	-1	-1
TYR-B0006	0	0	0	0	0	0
ARG+B0007	1	1	1	1	1	1
HIS+B0009	0	0	0	0	0	0
ASP-B0015	-1	-1	-1	-1	-1	-1
ARG+B0018	1	1	1	1	1	1
HIS+B0023	0	0	0	0	0	0

HIS+B0026	0	0	0	0	0	0
TYR-B0040	0	0	0	0	0	0
GLU-B0041	-1	-1	-1	-1	-1	-1
ASP-B0046	-0.99	-1	-1	-1	-1	-1
ASP-B0049	-1	-1	-1	-1	-1	-1
ARG+B0057	1	1	1	1	1	1
ARG+B0068	1	1	1	1	1	1
GLU-B0083	-0.99	-0.99	-0.99	-0.99	-0.99	-0.99
ASP-B0087	-0.97	-0.98	-0.96	-0.98	-0.97	-0.98
GLU-B0094	-1	-1	-1	-1	-1	-1
HIS+B0100	0	0	0	0	0	0
CYS-B0112	0	0	0	0	0	0
HIS+B0114	0	0	0	0	0	0
TYR-B0117	0	0	0	0	0	0
ASP-B0119	-0.94	-0.9	-0.89	-0.96	-0.89	-0.97
GLU-B0121	-0.96	-0.93	-0.96	-0.94	-0.97	-0.97
ARG+B0124	1	1	1	1	1	1
ASP-B0125	-1	-1	-1	-1	-1	-1
ARG+B0127	1	1	1	1	1	1
GLU-B0130	-0.99	-0.98	-0.99	-0.99	-0.99	-0.98
ASP-B0134	-1	-1	-1	-1	-1	-1
LYS+B0137	1	1	1	1	1	1
HIS+B0142	0	0	0	0	0	0
CYS-B0150	0	0	0	0	0	0
HIS+B0157	0	0	0	0	0	0
ASP-B0170	-1	-1	-1	-1	-1	-1
TYR-B0172	0	0	0	0	0	0
GLU-B0184	-0.99	-0.99	-0.99	-0.99	-0.99	-1
ASP-B0188	-0.99	-0.99	-0.99	-0.99	-0.99	-0.99
TYR-B0193	0	0	0	0	0	0
HIS+B0201	0	0	0	0	0	0
HIS+B0202	0	0	0	0	0	0
HIS+B0216	0	0	0	0	0	0
ARG+B0220	1	1	1	1	1	1
ARG+B0224	1	1	1	1	1	1
TYR-B0226	0	0	0	0	0	0
LYS+B0227	0.99	0.99	0.99	0.99	0.99	0.99
ARG+B0230	1	1	1	1	1	1
GLU-B0235	-1	-1	-1	-1	-1	-1
TYR-B0258	0	0	0	0	0	0
GLU-B0266	-1	-1	-1	-1	-1	-1
ARG+B0272	1	1	1	1	1	1
TYR-B0273	0	0	0	0	0	0

ASP-B0276	-1	-1	-1	-1	-1	-1
TYR-B0279	0	0	0	0	0	0
GLU-B0283	-1	-1	-1	-1	-1	-1
ARG+B0286	1	1	1	1	1	1
ARG+B0287	1	1	1	1	1	1
GLU-B0299	-0.99	-0.99	-0.99	-0.99	-0.99	-0.99
GLU-B0300	-0.99	-0.99	-0.98	-0.99	-0.99	-0.99
GLU-B0307	-0.95	-0.96	-0.95	-0.95	-0.96	-0.95
LYS+B0308	1	1	1	1	1	1
TYR-B0312	0	0	0	0	0	0
ASP-B0313	-1	-1	-1	-1	-1	-1
TYR-B0314	0	0	0	0	0	0
LYS+B0321	1	1	1	1	1	1
ARG+B0326	1	1	1	1	1	1
LYS+B0332	1	1	1	1	1	1
ASP-B0334	-1	-1	-1	-1	-1	-1
LYS+B0341	1	1	1	1	1	1
HIS+B0343	0.2	0.13	0.26	0.15	0.26	0.26
ARG+B0347	1	1	1	1	1	1
LYS+B0349	1	1	1	1	1	1
GLU-B0350	-0.88	-0.93	-0.87	-0.94	-0.93	-0.87
GLU-B0352	-1	-1	-1	-1	-1	-1
GLU-B0353	-0.84	-0.93	-0.85	-0.91	-0.94	-0.84
ARG+B0357	1	1	1	1	1	1
ARG+B0358	1	1	1	1	1	1
GLU-B0364	-1	-1	-1	-1	-1	-1
ASP-B0372	-1	-1	-1	-1	-1	-1
LYS+B0373	1	1	1	1	1	1
LYS+B0378	1	1	1	1	1	1
ASP-B0380	0	0	0	0	0	0
ARG+B0384	0.98	0.99	0.98	0.98	0.98	0.99
ARG+B0385	1	1	1	1	1	1
GLU-B0387	-0.55	-0.34	-0.71	-0.64	-0.72	-0.53
LYS+B0389	1	1	1	1	1	1
TYR-B0390	0	0	0	0	0	0
GLU-B0393	-0.96	-0.95	-0.99	-0.96	-0.96	-0.97
TYR-B0402	0	0	0	0	0	0
GLU-B0405	-0.51	-0.5	-0.52	-0.55	-0.5	-0.53
ASP-B0413	-0.92	-0.94	-0.91	-0.93	-0.93	-0.93
LYS+B0418	1	1	1	1	1	1
TYR-B0420	0	0	0	0	0	0
ARG+B0422	1	1	1	1	1	1
LYS+B0423	1	1	1	1	1	1

GLU-B0428	-0.19	-0.11	-0.25	-0.14	-0.24	-0.25
GLU-B0431	-1	-0.98	-0.98	-0.98	-0.99	-0.99
ASP-B0433	-1	-1	-1	-0.99	-0.99	-0.99
GLU-B0435	-0.99	-0.97	-0.99	-0.97	-0.98	-0.99
ASP-B0440	-1	-1	-1	-1	-1	-1
ARG+B0444	1	1	1	1	1	1
ARG+B0448	1	1	1	1	1	1
HIS+B0455	0	0	0	0	0	0
HIS+B0466	0	0	0	0	0	0
HIS+B0469	0	0	0	0	0	0
ARG+B0472	1	1	1	1	1	1
ARG+B0476	1	1	1	1	1	1
ASP-B0477	-1	-1	-1	-1	-1	-1
ASP-B0483	-1	-1	-1	-1	-1	-1
GLU-B0485	-1	-1	-1	-1	-1	-1
GLU-B0489	-0.98	-0.97	-0.98	-0.96	-0.96	-0.96
GLU-B0492	-0.06	-0.12	-0.06	-0.14	-0.11	-0.11
TYR-B0496	0	0	0	0	0	0
LYS+B0498	1	1	1	1	1	1
ASP-B0501	-1	-1	-1	-1	-1	-1
ARG+B0505	1	1	1	1	1	1
ARG+C0026	1	1	1	1	1	1
ASP-C0027	-1	-1	-1	-1	-1	-1
GLU-C0029	-1	-1	-1	-1	-1	-1
ARG+C0041	1	1	1	1	1	1
LYS+C0048	1	1	1	1	1	1
HIS+C0053	0	0	0	0	0	0
HIS+C0056	0	0	0	0	0	0
GLU-C0071	-1	-1	-1	-1	-1	-1
HIS+C0074	0.77	0.95	0.95	0.92	0.82	0.9
GLU-C0078	-0.99	-1	-1	-1	-0.99	-1
LYS+C0079	1	1	1	1	1	1
TYR-C0082	0	0	0	0	0	0
GLU-C0083	-1	-1	-1	-1	-1	-1
HIS+C0091	1	1	1	1	1	1
GLU-C0104	-0.99	-0.99	-1	-1	-1	-1
ASP-C0107	-1	-0.99	-0.99	-1	-0.99	-1
HIS+C0118	0	0	0	0	0	0
TYR-C0131	0	0	0	0	0	0
HIS+C0132	0	0	0	0	0	0
ARG+C0135	1	1	1	1	1	1
GLU-C0138	-1	-0.99	-0.98	-1	-0.99	-1
GLU-C0141	-1	-1	-1	-1	-1	-1

GLU-C0142	-0.99	-0.99	-0.99	-0.99	-0.99	-0.99
TYR-C0143	0	0	0	0	0	0
TYR-C0149	0	0	0	0	0	0
ASP-C0150	-1	-1	-1	-1	-1	-1
LYS+C0152	1	1	1	1	1	1
ASP-C0153	-1	-1	-1	-1	-1	-1
LYS+C0154	0.84	0.84	0.84	0.84	0.84	0.84
LYS+C0156	1	1	1	1	1	1
HIS+C0164	0	0	0	0	0	0
LYS+C0178	1	1	1	1	1	1
TYR-C0186	0	0	0	0	0	0
ASP-C0187	-1	-1	-1	-1	-1	-1
ASP-C0195	-0.9	-0.8	-0.89	-0.8	-0.87	-0.78
ARG+C0197	1	1	1	1	1	1
ASP-C0205	-1	-1	-1	-1	-1	-1
ARG+C0207	1	1	1	1	1	1
TYR-C0212	0	0	0	0	0	0
LYS+C0215	1	1	1	1	1	1
GLU-C0221	-0.91	-0.82	-0.89	-0.76	-0.66	-0.76
GLU-C0231	-1	-1	-1	-1	-1	-1
ASP-C0232	-1	-1	-1	-1	-1	-1
HIS+C0237	0	0	0	0	0	0
CYS-C0244	0	0	0	0	0	0
HIS+C0251	0	0	0	0	0	0
ARG+C0261	1	1	1	1	1	1
ARG+C0262	1	1	1	1	1	1
GLU-C0269	-1	-1	-1	-1	-1	-1
TYR-C0271	0	0	0	0	0	0
TYR-C0274	0	0	0	0	0	0
CYS-C0288	0	0	0	0	0	0
TYR-C0297	0	0	0	0	0	0
GLU-C0300	-1	-1	-1	-1	-1	-1
TYR-C0302	0	0	0	0	0	0
GLU-C0308	-1	-1	-1	-1	-1	-1
ARG+C0320	1	1	1	1	1	1
ASP-C0321	-1	-1	-1	-1	-1	-1
LYS+C0323	1	1	1	1	1	1
LYS+C0339	1	1	1	1	1	1
TYR-C0340	0	0	0	0	0	0
ARG+C0343	1	1	1	1	1	1
GLU-C0348	-1	-1	-1	-1	-1	-1
GLU-C0354	0	-0.04	-0.03	-0.04	0	-0.03
ARG+C0357	1	1	1	1	1	1

ASP-C0360	-1	-1	-1	-1	-1	-1
ARG+C0362	1	1	1	1	1	1
GLU-C0367	-1	-1	-1	-1	-1	-1
ARG+C0370	1	1	1	1	1	1
ASP-C0376	-1	-1	-1	-1	-1	-1
LYS+C0379	1	1	1	1	1	1
LYS+C0381	1	1	1	1	1	1
ASP-C0383	-0.85	-0.85	-0.85	-0.93	-0.85	-0.86
GLU-C0389	-1	-1	-1	-1	-1	-1
ARG+C0390	1	1	1	1	1	1
ARG+C0391	1	1	1	1	1	1
GLU-C0394	-1	-1	-1	-1	-1	-1
TYR-C0395	0	0	0	0	0	0
HIS+C0398	0.99	0.99	0.98	0.98	0.98	0.99
GLU-C0413	-1	-1	-1	-1	-1	-1
ARG+C0423	1	1	1	1	1	1
HIS+C0430	0	0	0	0	0	0
HIS+C0441	0	0	0	0	0	0
HIS+C0444	0	0	0	0	0	0
ARG+C0447	1	1	1	1	1	1
ARG+C0449	1	1	1	1	1	1
GLU-C0456	-1	-1	-1	-1	-1	-1
LYS+C0457	1	1	1	1	1	1
ASP-C0460	-0.96	-0.97	-0.96	-0.96	-0.97	-0.97
ARG+C0461	1	1	1	1	1	1
GLU-C0462	-0.91	-0.9	-0.91	-0.92	-0.92	-0.91
GLU-C0464	-1	-1	-1	-1	-1	-1
ASP-C0473	-1	-1	-1	-1	-1	-1
GLU-D0011	-0.56	-0.56	-0.72	-0.67	-0.68	-0.77
ARG+D0012	1	1	1	1	1	1
ASP-D0016	-1	-1	-1	-1	-1	-1
ASP-D0019	-1	-1	-1	-1	-1	-1
ASP-D0020	-1	-1	-1	-1	-1	-1
LYS+D0023	1	1	1	1	1	1
ARG+D0024	1	1	1	1	1	1
ASP-D0025	-1	-1	-1	-1	-1	-1
ARG+D0026	1	1	1	1	1	1
CYS-D0040	0	0	0	0	0	0
TYR-D0042	0	0	0	0	0	0
TYR-D0059	0	0	0	0	0	0
HIS+D0061	0	0	0	0	0	0
TYR-D0067	0	0	0	0	0	0
GLU-D0069	-1	-1	-1	-1	-1	-1

CYS-D0071	0	0	0	0	0	0
HIS+D0087	0	0	0	0	0	0
GLU-D0096	-1	-1	-1	-1	-1	-1
ASP-D0100	-1	-1	-1	-1	-1	-1
ARG+D0103	1	1	1	1	1	1
CYS-D0105	0	0	0	0	0	0
HIS+D0117	0	0	0	0	0	0
ARG+D0128	1	1	1	1	1	1
GLU-D0131	-1	-1	-1	-1	-1	-1
ARG+D0134	1	1	1	1	1	1
ARG+D0139	1	1	1	1	1	1
TYR-D0141	0	0	0	0	0	0
TYR-D0160	0	0	0	0	0	0
ARG+D0180	1	1	1	1	1	1
HIS+D0189	0	0	0	0	0	0
HIS+D0197	0	0	0	0	0	0
CYS-D0211	0	0	0	0	0	0
HIS+D0214	0	0	0	0	0	0
GLU-D0219	0	0	0	0	0	0
ASP-D0225	-1	-1	-1	-1	-1	-1
GLU-D0227	-0.97	-0.96	-0.98	-0.97	-0.97	-0.97
ARG+D0233	1	1	1	1	1	1
GLU-D0241	-1	-1	-1	-1	-1	-1
GLU-D0242	-0.13	-0.09	-0.09	-0.03	-0.11	-0.07
TYR-D0244	0	0	0	0	0	0
ARG+D0251	1	1	1	1	1	1
LYS+D0264	1	1	1	1	1	1
ARG+D0265	0.3	0.19	0.25	0.51	0.6	0.46
HIS+D0268	0	0	0	0	0	0
ARG+D0294	1	1	1	1	1	1
TYR-D0296	0	0	0	0	0	0
ASP-D0297	-1	-1	-1	-1	-1	-1
GLU-D0302	-1	-1	-1	-1	-1	-1
ARG+D0304	1	1	1	1	1	1
GLU-D0307	-0.68	-0.71	-0.69	-0.7	-0.69	-0.69
ASP-D0308	-1	-1	-1	-1	-1	-1
GLU-D0310	-0.99	-0.97	-0.98	-0.98	-0.98	-0.92
GLU-D0312	0	0	0	0	0	0
TYR-D0315	0	0	0	0	0	0
LYS+D0317	1	1	1	1	1	1
GLU-D0323	-1	-1	-1	-1	-1	-1
ARG+D0326	1	1	1	1	1	1
ASP-D0333	-1	-1	-1	-1	-1	-1

HIS+D0336	0	0	0	0	0	0
GLU-D0337	-1	-1	-1	-1	-1	-1
GLU-D0343	-0.66	-0.84	-0.79	-0.75	-0.77	-0.77
GLU-D0344	-1	-1	-1	-1	-1	-1
ARG+D0348	0.35	0.2	0.47	0.32	0.49	0.25
GLU-E0007	-1	-1	-1	-1	-1	-1
ARG+E0008	1	1	1	1	1	1
ASP-E0012	-1	-1	-1	-1	-1	-1
ARG+E0018	1	1	1	1	1	1
TYR-E0019	0	0	0	0	0	0
HIS+E0023	0	0	0	0	0	0
TYR-E0044	0	0	0	0	0	0
ASP-E0045	-1	-1	-1	-1	-1	-1
ARG+E0051	1	1	1	1	1	1
ASP-E0053	-1	-1	-1	-1	-1	-1
TYR-E0055	0	0	0	0	0	0
TYR-E0056	0	0	0	0	0	0
GLU-E0059	-1	-1	-1	-0.99	-1	-1
ARG+E0061	1	1	1	1	1	1
ASP-E0068	-1	-0.99	-1	-1	-1	-1
ARG+E0069	1	1	1	1	1	1
GLU-E0071	-0.86	-0.95	-0.85	-0.95	-0.94	-0.95
LYS+E0073	1	1	1	1	1	1
GLU-E0077	-1	-1	-1	-1	-1	-1
GLU-E0081	-1	-1	-1	-1	-1	-1
LYS+E0084	1	1	1	1	1	1
TYR-F0013	0	0	0	0	0	0
ARG+F0019	1	1	1	1	1	1
HIS+F0024	0	0	0	0	0	0
ARG+F0045	1	1	1	1	1	1
ARG+H0003	1	1	1	1	1	1
ARG+H0004	1	1	1	1	1	1
ASP-H0009	-1	-1	-1	-1	-1	-1
ARG+H0012	1	1	1	1	1	1
GLU-H0017	-1	-1	-1	-1	-1	-1
TYR-H0018	0	0	0	0	0	0
LYS+H0020	1	1	1	1	1	1
GLU-H0047	0	0	0	0	0	0
TYR-H0049	0	0	0	0	0	0
ASP-H0056	-0.68	-0.86	-0.69	-0.85	-0.68	-0.67
LYS+H0063	1	1	1	1	1	1
GLU-I0002	-0.73	-0.73	-0.73	-0.75	-0.75	-0.73
LYS+I0005	1	1	1	1	1	1

TYR-I0009	0	0	0	0	0	0
ASP-I0027	-1	-1	-1	-1	-1	-1
ARG+I0030	1	1	1	1	1	1
LYS+I0033	1	1	1	1	1	1
ARG+I0034	1	1	1	1	1	1
LYS+I0035	1	1	1	1	1	1
ASP-I0036	-1	-1	-1	-1	-1	-1
GLU-I0038	-0.99	-0.99	-1	-1	-1	-1
GLU-J0004	-0.99	-1	-0.99	-1	-1	-0.99
ARG+J0007	1	1	1	1	1	1
TYR-J0030	0	0	0	0	0	0
TYR-J0033	0	0	0	0	0	0
LYS+K0010	1	1	1	1	1	1
GLU-K0013	-0.97	-0.98	-0.96	-0.92	-0.97	-0.92
TYR-K0015	0	0	0	0	0	0
ASP-K0019	-0.61	-0.83	-0.85	-0.84	-0.82	-0.63
ASP-K0023	-0.9	-0.98	-0.97	-0.95	-0.91	-0.98
ARG+K0046	1	1	1	1	1	1
GLU-L0002	-0.99	-0.99	-0.98	-0.99	-0.98	-0.99
ARG+L0007	1	1	1	1	1	1
GLU-L0011	-0.81	-0.76	-0.68	-0.69	-0.79	-0.8
ARG+L0014	1	1	1	1	1	1
TYR-L0018	0	0	0	0	0	0
TYR-L0034	0	0	0	0	0	0
GLU-M0002	-1	-0.99	-0.99	-1	-0.99	-1
TYR-M0026	0	0	0	0	0	0
GLU-M0030	-1	-1	-1	-1	-1	-0.99
LYS+M0034	1	1	1	1	1	1
TYR-O0007	0	0	0	0	0	0
ASP-O0008	-1	-1	-1	-1	-1	-1
ASP-O0009	-1	-1	-1	-0.99	-1	-1
LYS+O0018	1	1	1	1	1	1
ASP-O0023	-1	-1	-1	-1	-1	-1
ASP-O0024	-1	-1	-1	-1	-1	-1
ARG+O0027	1	1	1	1	1	1
TYR-O0030	0	0	0	0	0	0
ASP-O0033	-0.99	-0.99	-1	-0.99	-1	-1
TYR-O0038	0	0	0	0	0	0
ARG+O0039	1	1	1	1	1	1
ARG+O0042	1	1	1	1	1	1
LYS+O0053	1	1	1	1	1	1
GLU-O0054	-1	-1	-1	-1	-1	-1
GLU-O0055	-0.9	-0.91	-0.92	-0.9	-0.79	-0.92

LYS+O0057	1	1	1	1	1	1
LYS+O0059	1	1	1	1	1	1
ARG+O0060	1	1	1	1	1	1
GLU-O0064	-0.94	-0.98	-0.98	-0.98	-0.98	-0.98
LYS+O0069	1	1	1	1	1	1
ARG+O0073	1	1	1	1	1	1
GLU-O0074	-0.99	-1	-1	-0.99	-0.99	-1
ASP-O0079	-1	-1	-1	-1	-1	-1
GLU-O0084	-0.96	-0.98	-0.98	-0.98	-0.98	-0.98
LYS+O0086	1	1	1	1	1	1
ASP-O0090	-1	-1	-1	-1	-1	-1
GLU-O0097	-0.29	-0.28	-0.29	-0.33	-0.19	-0.27
GLU-O0098	-1	-1	-1	-1	-1	-1
ASP-O0099	-1	-1	-1	-1	-1	-1
ASP-O0102	-0.06	-0.07	-0.07	-0.03	-0.05	-0.05
GLU-O0114	-0.93	-0.96	-0.93	-0.98	-0.98	-0.98
ARG+O0115	1	1	1	1	1	1
LYS+O0123	1	1	1	1	1	1
ASP-O0141	-1	-1	-1	-1	-1	-1
LYS+O0143	1	1	1	1	1	1
GLU-O0145	-1	-1	-1	-1	-1	-1
TYR-O0151	0	0	0	0	0	0
ARG+O0152	1	1	1	1	1	1
ASP-O0158	-1	-1	-1	-1	-1	-1
LYS+O0160	1	1	1	1	1	1
ARG+O0162	1	1	1	1	1	1
TYR-O0168	0	0	0	0	0	0
ASP-O0169	-1	-1	-1	-1	-1	-1
LYS+O0178	1	1	1	1	1	1
GLU-O0179	-0.94	-0.95	-0.94	-0.97	-0.98	-0.97
GLU-O0180	-0.97	-0.98	-0.99	-0.98	-0.99	-0.99
GLU-O0181	-1	-0.99	-0.99	-0.99	-1	-1
ARG+O0184	1	1	1	1	1	1
LYS+O0188	1	1	1	1	1	1
ARG+O0189	1	1	1	1	1	1
LYS+O0194	1	1	1	1	1	1
LYS+O0203	1	1	1	1	1	1
ASP-O0205	-1	-1	-1	-1	-1	-1
ARG+O0207	1	1	1	1	1	1
GLU-O0210	-0.99	-0.98	-0.98	-1	-0.99	-0.99
GLU-O0216	-0.99	-0.99	-1	-0.99	-1	-0.99
GLU-O0218	-1	-1	-1	-1	-1	-1
ASP-O0222	-0.97	-0.96	-0.96	-0.96	-0.97	-0.96

ASP-O0223	-0.99	-0.99	-0.99	-0.99	-0.99	-0.99
ASP-O0224	0	0	0	0	0	0
HIS+O0228	0.99	0.99	0.99	0.99	0.99	0.95
GLU-O0229	-1	-1	-1	-1	-1	-1
HIS+O0231	0	0	0	0	0	0
GLU-O0232	-1	-1	-1	-1	-1	-1
LYS+O0234	1	1	1	1	1	1
TYR-O0240	0	0	0	0	0	0
GLU-O0244	-1	-1	-1	-1	-1	-1
GLU-T0002	-0.99	-1	-1	-1	-1	-1
TYR-T0006	0	0	0	0	0	0
CYS-T0012	0	0	0	0	0	0
ARG+T0024	1	1	1	1	1	1
GLU-T0025	-1	-1	-1	-0.99	-0.99	-1
ARG+T0028	1	1	1	1	1	1
GLU-U0008	-0.96	-0.92	-0.91	-0.95	-0.96	-0.9
ASP-U0014	-1	-1	-1	-1	-1	-1
GLU-U0015	-1	-1	-1	-1	-1	-1
LYS+U0016	1	1	1	1	1	1
TYR-U0021	0	0	0	0	0	0
GLU-U0023	-0.98	-0.96	-0.98	-0.96	-0.98	-0.98
LYS+U0024	1	1	1	1	1	1
ASP-U0026	-1	-1	-1	-1	-1	-1
TYR-U0038	0	0	0	0	0	0
ARG+U0039	1	1	1	1	1	1
TYR-U0042	0	0	0	0	0	0
LYS+U0047	1	1	1	1	1	1
LYS+U0051	1	1	1	1	1	1
TYR-U0055	0	0	0	0	0	0
GLU-U0056	-1	-1	-1	-1	-1	-1
GLU-U0059	-1	-1	-1	-1	-1	-1
ASP-U0060	-1	-1	-1	-1	-1	-1
GLU-U0069	-1	-1	-1	-1	-1	-1
ARG+U0070	1	1	1	1	1	1
LYS+U0072	1	1	1	1	1	1
ARG+U0076	1	1	1	1	1	1
GLU-U0077	-1	-1	-1	-1	-1	-1
GLU-U0080	-0.99	-0.97	-0.97	-0.99	-0.97	-0.98
HIS+U0081	0.99	0.98	0.99	0.99	0.99	0.99
GLU-U0086	-0.99	-1	-0.99	-0.99	-0.99	-1
GLU-U0088	-1	-0.99	-1	-1	-1	-1
GLU-U0093	-0.99	-0.99	-0.99	-0.99	-0.99	-0.99
ASP-U0096	-0.97	-0.98	-0.98	-0.98	-0.98	-0.98

ARG+U0097	1	1	1	1	1	1
TYR-U0098	0	0	0	0	0	0
TYR-U0103	0	0	0	0	0	0
LYS+U0104	1	1	1	1	1	1
GLU-V0002	-1	-1	-0.99	-0.99	-1	-1
GLU-V0006	-0.95	-0.94	-0.95	-0.85	-0.84	-0.94
GLU-V0015	-0.98	-0.98	-0.95	-0.95	-0.98	-0.98
LYS+V0017	1	1	1	1	1	1
GLU-V0023	-1	-1	-1	-1	-1	-1
LYS+V0024	1	1	1	1	1	1
TYR-V0026	0	0	0	0	0	0
GLU-V0028	-1	-1	-1	-1	-1	-1
LYS+V0030	0.53	0.52	0.46	0.46	0.53	0.49
ARG+V0031	1	1	1	1	1	1
TYR-V0035	0	0	0	0	0	0
CYS-V0037	0	0	0	0	0	0
CYS-V0040	0	0	0	0	0	0
HIS+V0041	0	0	0	0	0	0
LYS+V0047	1	1	1	1	1	1
ASP-V0053	-0.99	-0.99	-1	-1	-1	-0.99
ARG+V0055	1	1	1	1	1	1
GLU-V0057	-0.99	-0.99	-0.99	-0.99	-1	-0.99
ARG+V0066	1	1	1	1	1	1
ASP-V0067	-0.97	-0.97	-0.97	-0.93	-0.92	-0.97
GLU-V0070	-1	-1	-1	-1	-1	-1
ASP-V0074	-1	-1	-1	-0.99	-1	-1
TYR-V0075	0	0	0	0	0	0
LYS+V0077	1	1	1	1	1	1
TYR-V0082	0	0	0	0	0	0
ASP-V0083	-1	-1	-1	-1	-1	-1
GLU-V0085	-1	-1	-1	-1	-1	-1
GLU-V0087	-0.99	-0.99	-0.99	-0.99	-0.99	-0.99
GLU-V0090	-0.98	-0.98	-0.99	-0.98	-0.99	-0.98
HIS+V0092	0	0	0	0	0	0
ARG+V0096	1	1	1	1	1	1
ASP-V0099	-1	-1	-1	-1	-1	-1
LYS+V0103	1	1	1	1	1	1
ARG+V0105	1	1	1	1	1	1
GLU-V0109	-1	-1	-1	-1	-1	-1
LYS+V0110	1	1	1	1	1	1
ASP-V0111	-1	-1	-1	-1	-1	-1
HIS+V0118	0	0	0	0	0	0
GLU-V0122	-0.98	-0.96	-0.95	-0.95	-0.97	-0.99

LYS+V0124	1	1	1	1	1	1
ASP-V0128	-0.99	-0.99	-1	-0.99	-0.99	-0.99
LYS+V0129	1	1	1	1	1	1
LYS+V0134	0.94	0.95	0.93	0.94	0.92	0.95
TYR-V0136	0	0	0	0	0	0
TYR-V0137	0	0	0	0	0	0
LYS+X0008	0.82	0.83	0.82	0.84	0.83	0.82
ASP-X0035	-0.66	-0.44	-0.47	-0.48	-0.43	-0.44
LYS+X0036	1	1	1	1	1	1
ARG+X0039	1	1	1	1	1	1
ARG+Y0042	1	1	1	1	1	1
ARG+Y0043	1	1	1	1	1	1
TYR-Z0027	0	0	0	0	0	0
ASP-Z0032	-1	-1	-1	-1	-1	-1
ASP-Z0034	-1	-1	-1	-1	-1	-1
ARG+Z0035	1	1	1	1	1	1
LYS+Z0037	1	1	1	1	1	1

Appendix II. Supplemental data for Bacterioferritin-$ZnCe_6$ paper

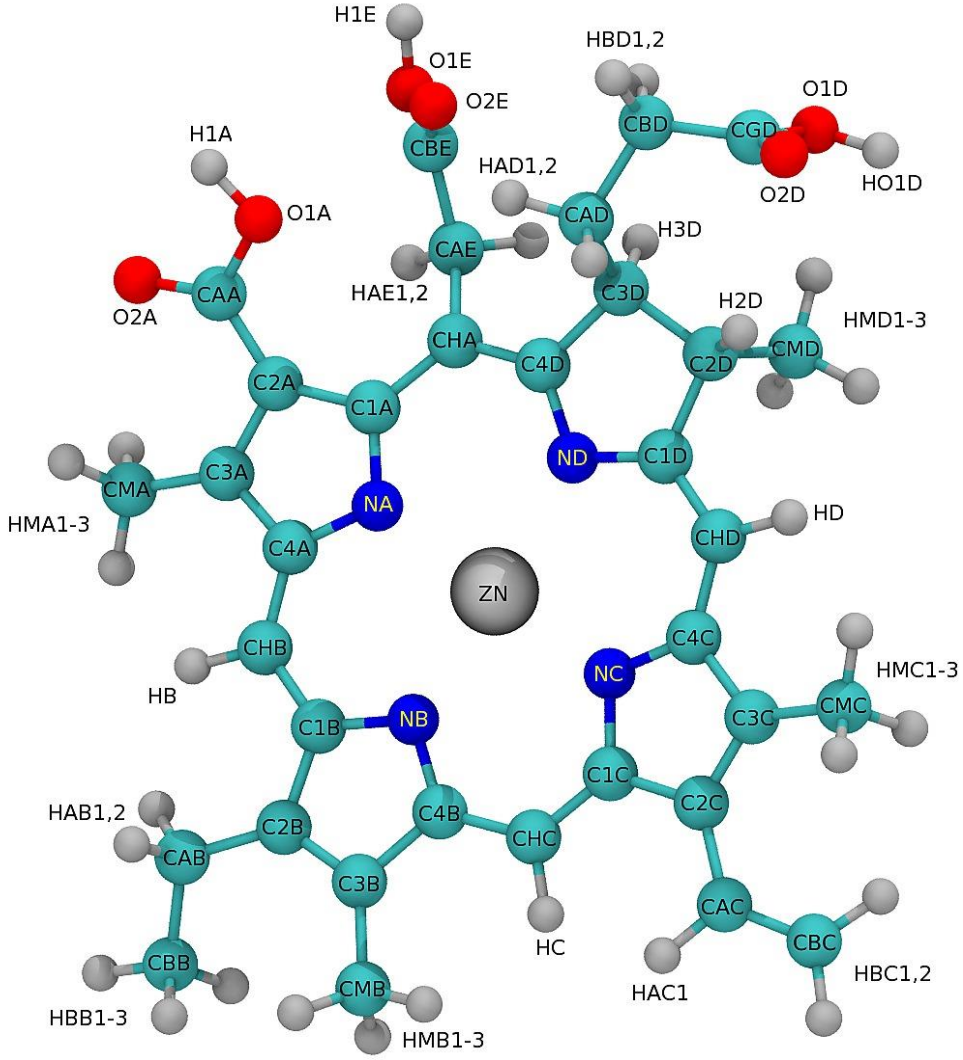

Figure S1. Schematic diagram of atom names for $ZnCe_6$

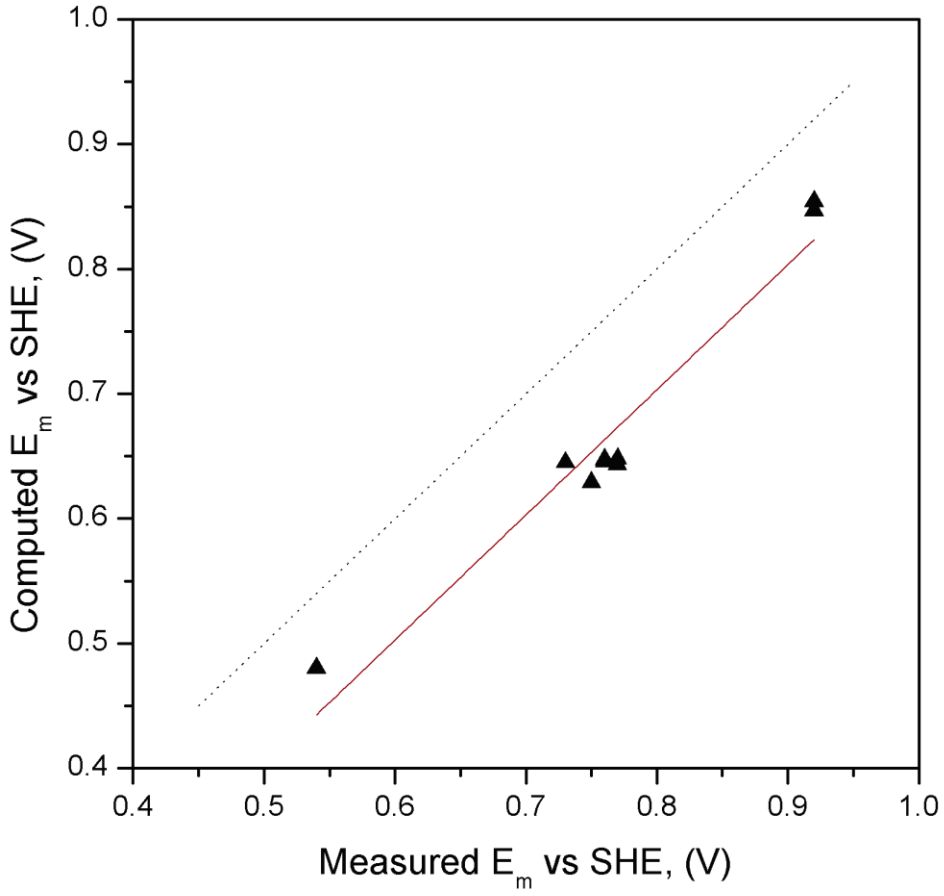

Figure S2. Experimental vs. calculated E_m's of Zn-chlorin derivatives. DFT systematically underestimates values by 0.1 V, but after correction for this systematic shift all computed values are within 20 mV from measured. Experimental E_m's of the following Zn-chlorins were used: ZnC, ZnC -$A^3M^{10}A^{13}$, ZnC -M^{10}, ZnC -T^5, ZnC -P^{15}, ZnC -OP, ZnC -$T^5M^{10}P^{15}$, ZnC -P^{10}, ZnC -P^3M^{10} from [1] and $ZnCe_6$ from the current work. [1] H.L. Kee, C. Kirmaier, G. Tang, J.R. Diers, C. Muthiah, M. Taniguch, J.K. Laha, M. Ptaszek, J.S. Lindsey, D.F. Bocian, D. Hoten, Effects of substituents on synthetic analogs of chlorophylls. Part 2: Redox properties, optical spectra and electronic structure, Photochem. Photobiol. 83 (2007) pp. 1125–1143.

Table S1. Atomic charges for neutral and oxidized $ZnCe_6$. The charges were derived using RESP-A1 procedure (HF/6-31G*, Connolly surface, 2 RESP stages, qwt = 0.0005/0.001). Cavity radii for Poisson-Boltzmann electro-statics computations: Zn=1.47, C=1.7, O=1.4, N=1.5, H=1.0. PARSE charges for –COOH groups were used for computation of pKas.

#	Atom name	Charge reduced	Charge oxidized
1	ZN	1.153119	1.135671
2	NA	-0.500472	-0.523643
3	C1A	0.029232	0.146484
4	C2A	-0.078838	-0.025960
5	C3A	0.043641	0.056489
6	C4A	0.037627	0.195239
7	CHA	-0.004483	-0.022431
8	NB	-0.446619	-0.442603
9	C1B	-0.031386	0.059164
10	C2B	-0.057905	-0.081145
11	C3B	0.067260	0.106337
12	C4B	0.083702	0.212731
13	CHB	-0.020760	-0.025440
14	HB	0.131281	0.093844
15	NC	-0.545711	-0.588825
16	C1C	0.063483	0.107711
17	C2C	0.041989	0.050908
18	C3C	0.082014	0.098751
19	C4C	0.245178	0.287763
20	CHC	-0.106474	-0.114445
21	HC	0.106884	0.106817
22	ND	-0.476973	-0.440841
23	C1D	0.191954	0.166771
24	C2D	0.111139	0.110710
25	H2D	0.042283	0.063478
26	C3D	0.018045	0.019635
27	H3D	0.078805	0.104812
28	C4D	0.040879	0.049045
29	CHD	-0.382213	-0.358231
30	HD	0.139720	0.147613
31	CMA	-0.259038	-0.378873
32	HMA1	0.093060	0.144193
33	HMA2	0.093060	0.144193
34	HMA3	0.093060	0.144193
35	CMB	-0.232209	-0.268436
36	HMB1	0.075913	0.104880
37	HMB2	0.075913	0.104880
38	HMB3	0.075913	0.104880
39	CMC	-0.208352	-0.208295
40	HMC1	0.071852	0.082916
41	HMC2	0.071852	0.082916
42	HMC3	0.071852	0.082916
43	CMD	-0.207389	-0.215648
44	HMD1	0.061232	0.073863
45	HMD2	0.061232	0.073863
46	HMD3	0.061232	0.073863
47	CAB	-0.017080	-0.020219
48	HAB1	0.033666	0.049637
49	HAB2	0.033666	0.049637
50	CBB	-0.022956	-0.022505
51	HBB1	0.013844	0.022816
52	HBB2	0.013844	0.022816
53	HBB3	0.013844	0.022816
54	CAC	-0.169178	-0.193477
55	HAC1	0.150771	0.155417
56	CBC	-0.321297	-0.281741
57	HBC1	0.156711	0.165305
58	HBC2	0.169478	0.164342
59	CAA	0.653594	0.737304
60	O1A	-0.556759	-0.556759
61	O2A	-0.556759	-0.556759
62	H2A	0.430379	0.430379
63	CAE	-0.029570	-0.132547
64	HAE1	0.056834	0.086955
65	HAE2	0.056834	0.086955
66	CBE	0.544857	0.608873
67	O1E	-0.556759	-0.556759
68	O2E	-0.556759	-0.556759
69	H2E	0.430379	0.430379
70	CAD	-0.075040	-0.145945
71	HAD1	0.042558	0.067811
72	HAD2	0.042558	0.067811
73	CBD	-0.046107	-0.066981
74	HBD1	0.033979	0.053151
75	HBD2	0.033979	0.053151
76	CGD	0.624042	0.655322
77	O1D	-0.556759	-0.556759
78	O2D	-0.556759	-0.556759
79	HO1D	0.430379	0.430379

Appendix III. NMR of $[P(OEP)Cl_2]^+Cl^-$

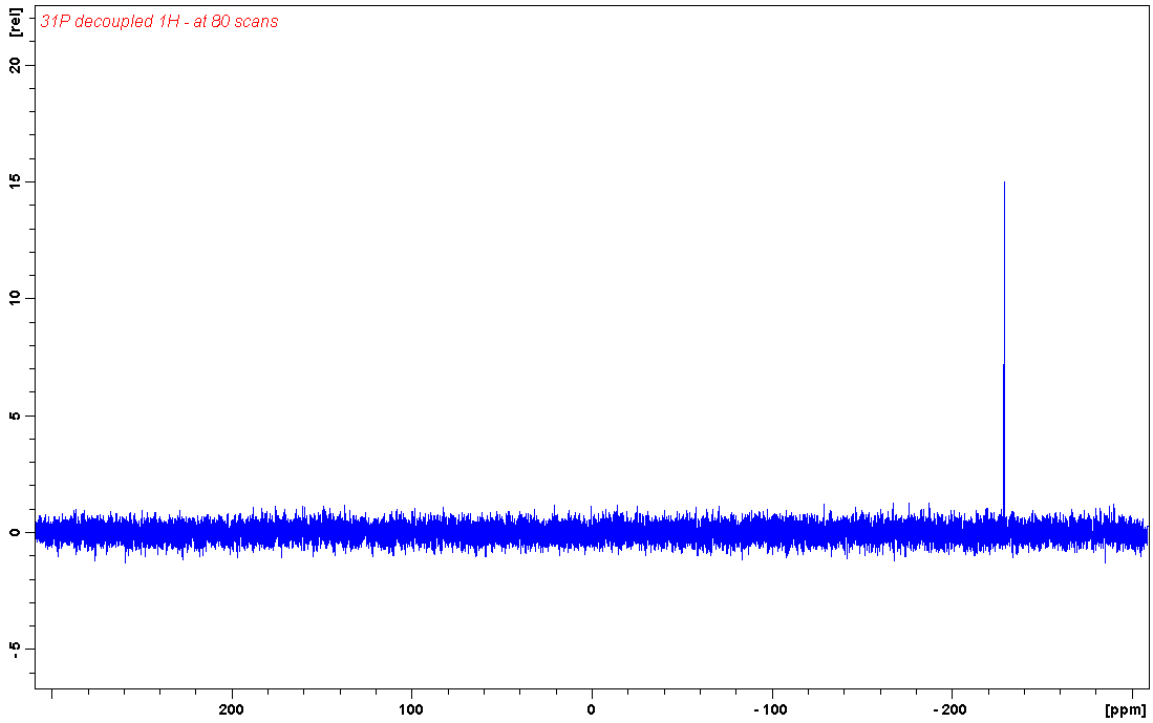

Figure 1. Proton decoupled ^{31}P NMR of $[P(OEP)Cl_2]^+Cl^-$

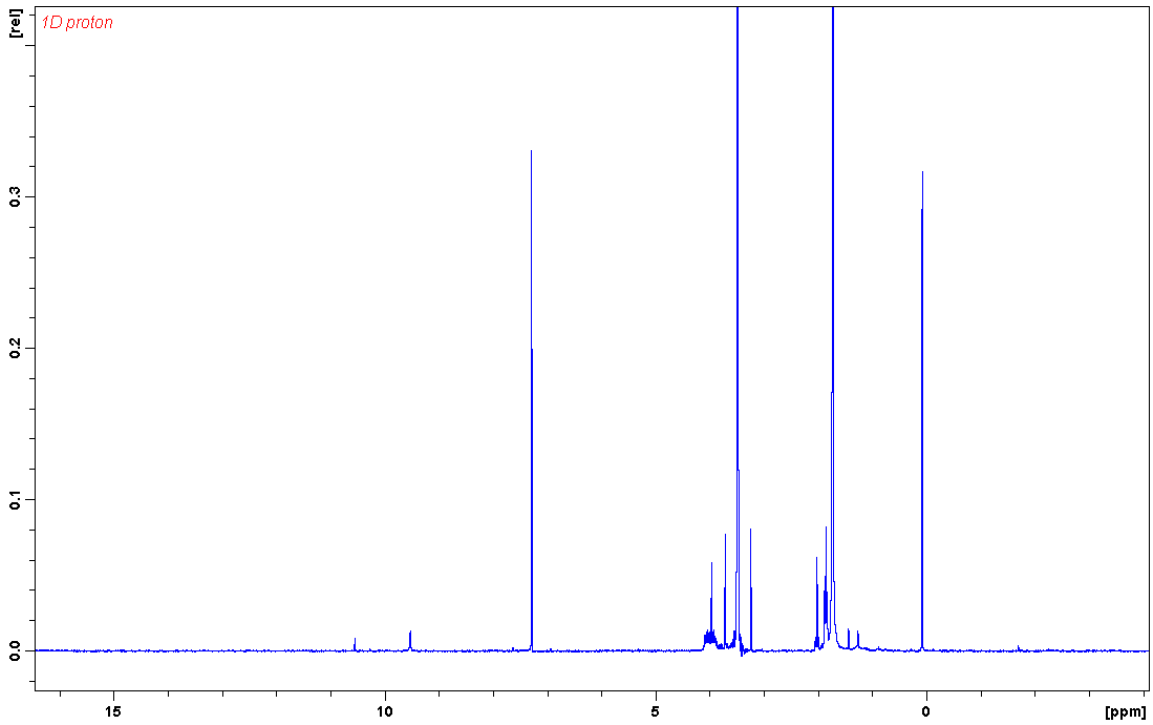

Figure 2. Proton NMR of $[P(OEP)Cl_2]^+Cl^-$

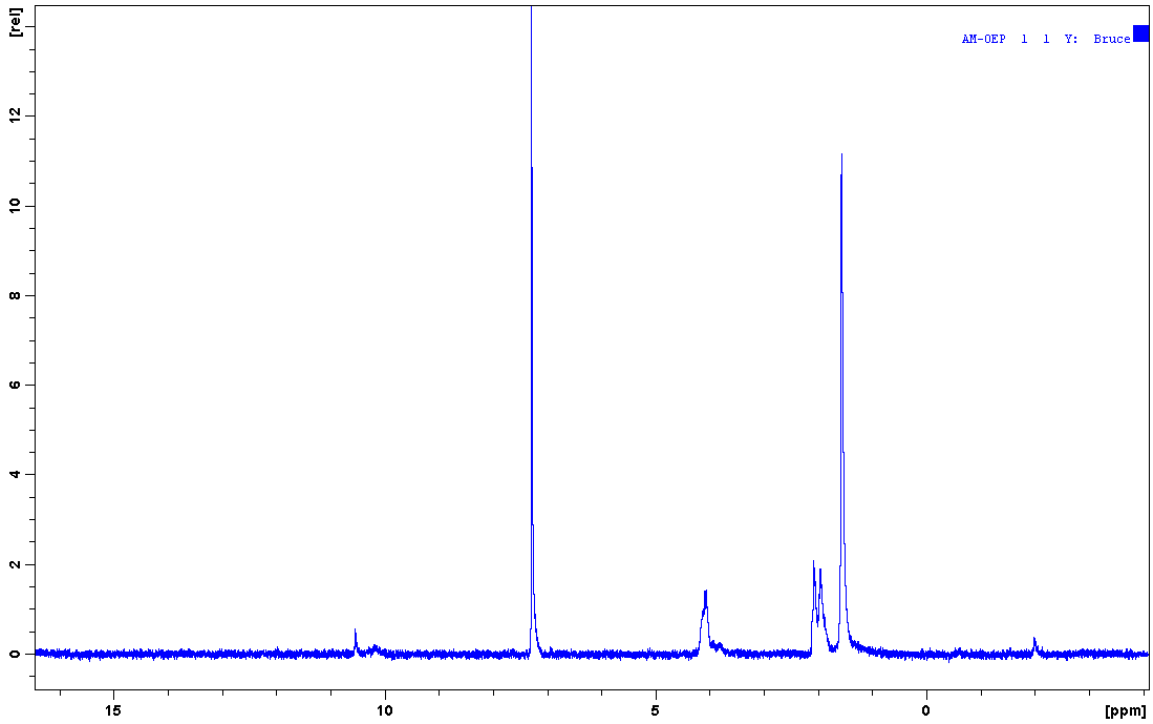

Figure 3. Starting material for the pigment synthesis Octaethylporphine proton NMR

Appendix IV. Fits of Fluorescence Decay Kinetics

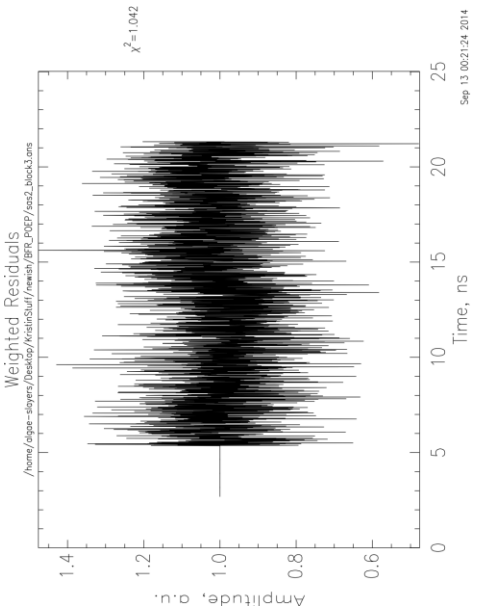

Figure1. Residual of the for Fluorescence Decay Kinetics to one component in the case of fluorescence of pigment in DMSO solution

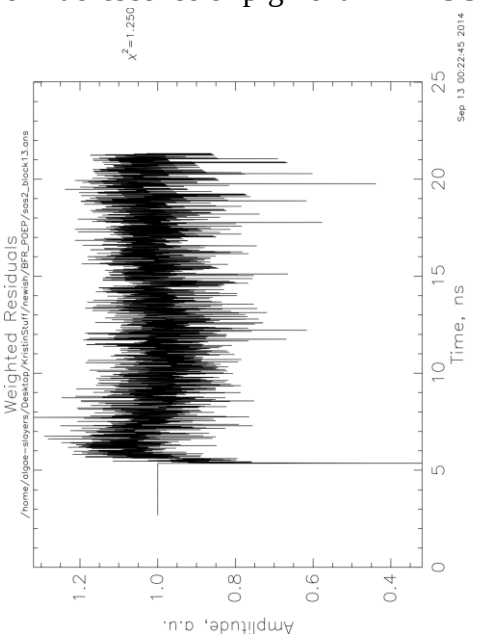

Figure2. Residual of the for Fluorescence Decay Kinetics to two component in the case of fluorescence of pigment crosslinked to BFR (BFR-RC2)

REFERENCES

Akiba, K, R Nadano, W Satoh, Y Yamamoto, S Nagase, Z Ou, X Tan, and K M Kadish. 2001. "Synthesis, Structure, Electrochemistry, and Spectroelectrochemistry of Hypervalent phosphorus(V) Octaethylporphyrins and Theoretical Analysis of the Nature of the PO Bond in P(OEP)(CH(2)CH(3))(O)." *Inorganic Chemistry* 40 (22): 5553–67. http://www.ncbi.nlm.nih.gov/pubmed/11599954.

Allakhverdiev, Suleyman I, Tatsuya Tomo, Yuichiro Shimada, Hayato Kindo, Ryo Nagao, Vyacheslav V Klimov, and Mamoru Mimuro. 2010. "Redox Potential of Pheophytin a in Photosystem II of Two Cyanobacteria Having the Different Special Pair Chlorophylls." *Proceedings of the National Academy of Sciences of the United States of America* 107 (8): 3924–29. doi:10.1073/pnas.0913460107.

Anderson, Jan M, and W S Chow. 2002. "Structural and Functional Dynamics of Plant Photosystem II." *Philosophical Transactions of the Royal Society of London. Series B, Biological Sciences* 357 (1426): 1421–30; discussion 1469–70. doi:10.1098/rstb.2002.1138.

Andrews, Simon C. 2010. "The Ferritin-like Superfamily: Evolution of the Biological Iron Storeman from a Rubrerythrin-like Ancestor." *Biochimica et Biophysica Acta - General Subjects*. doi:10.1016/j.bbagen.2010.05.010.

Andrews, Simon C., Andrea K. Robinson, and Francisco Rodríguez-Quiñones. 2003. "Bacterial Iron Homeostasis." *FEMS Microbiology Reviews*. doi:10.1016/S0168-6445(03)00055-X.

Arlt, T, S Schmidt, W Kaiser, C Lauterwasser, M Meyer, H Scheer, and W Zinth. 1993. "The Accessory Bacteriochlorophyll: A Real Electron Carrier in Primary Photosynthesis." *Proceedings of the National Academy of Sciences of the United States of America* 90: 11757–61. doi:10.1073/pnas.90.24.11757.

ARO, E, I VIRGIN, and B ANDERSSON. 1993. "Photoinhibition of Photosystem II. Inactivation, Protein Damage and Turnover." *Biochimica et Biophysica Acta (BBA) - Bioenergetics* 1143 (2): 113–34. doi:10.1016/0005-2728(93)90134-2.

Baker, Christopher M, Pedro E M Lopes, Xiao Zhu, Benoît Roux, and Alexander D Mackerell. 2010. "Accurate Calculation of Hydration Free Energies Using Pair-Specific Lennard-Jones Parameters in the CHARMM Drude Polarizable Force Field." *Journal of Chemical Theory and Computation* 6: 1181–98. doi:10.1021/ct9005773.

Barber, James. 2003. “Photosystem II: The Engine of Life.” *Quarterly Reviews of Biophysics* 36 (1): 71–89. doi:10.1017/S0033583502003839.

Barker, P D, and S M Freund. 1996. “Bis-Methionine Ligation to Heme Iron in Mutants of Cytochrome b562. 2. Characterization by NMR of Heme-Ligand Interactions.” *Biochemistry* 35: 13627–35. doi:10.1021/bi961128p.

Basma, M, S Sundara, D Calgan, T Vernali, and R J Woods. 2001. “Solvated Ensemble Averaging in the Calculation of Partial Atomic Charges.” *Journal of Computational Chemistry* 22 (11): 1125–37. doi:10.1002/jcc.1072.

Basser, P J, S Pajevic, C Pierpaoli, J Duda, and A Aldroubi. 2000. “In Vivo Fiber Tractography Using DT-MRI Data.” *Magnetic Resonance in Medicine : Official Journal of the Society of Magnetic Resonance in Medicine / Society of Magnetic Resonance in Medicine* 44: 625–32. doi:10.1002/1522-2594(200010)44:4<625::AID-MRM17>3.0.CO;2-O.

Bayly, CI Christopher I, Piotr Cieplak, Wendy D Cornell, and Peter A Kollman. 1993. “A Well-Behaved Electrostatic Potential Based Method Using Charge Restraints for Deriving Atomic Charges: The RESP Model.” *The Journal of Physical …* 97: 10269–80. doi:10.1021/j100142a004.

Berry, B. W., M. C. Martinez-Rivera, and C. Tommos. 2012. “Reversible Voltammograms and a Pourbaix Diagram for a Protein Tyrosine Radical.” *Proceedings of the National Academy of Sciences*. doi:10.1073/pnas.1112057109.

Brettel, Klaus. 1997. “Electron Transfer and Arrangement of the Redox Cofactors in Photosystem I.” *Biochimica et Biophysica Acta (BBA) - Bioenergetics*. doi:10.1016/S0005-2728(96)00112-0.

Burnap, Robert L. 2004. “D1 Protein Processing and Mn Cluster Assembly in Light of the Emerging Photosystem II Structure.” *Physical Chemistry Chemical Physics* 6 (20). The Royal Society of Chemistry: 4803–9. doi:10.1039/B407094A.

Cardona, Tanai, Arezki Sedoud, Nicholas Cox, and a William Rutherford. 2012. “Charge Separation in Photosystem II: A Comparative and Evolutionary Overview.” *Biochimica et Biophysica Acta* 1817 (1). Elsevier B.V. 26–43. doi:10.1016/j.bbabio.2011.07.012.

Carrondo, Maria Arménia. 2003. “Ferritins, Iron Uptake and Storage from the Bacterioferritin Viewpoint.” *The EMBO Journal* 22: 1959–68. doi:10.1093/emboj/cdg215.

Case, D. A., Darden, T. A., Cheatham, T. E., Simmerling, C., Wang, J., et al. 2008. “AMBER 10”. San Francisco: University of California.

Cohen, Jordi, Kwiseon Kim, Paul King, Michael Seibert, and Klaus Schulten. 2005. "Finding Gas Diffusion Pathways in Proteins: Application to O2 and H2 Transport in CpI [FeFe]-Hydrogenase and the Role of Packing Defects." *Structure (London, England : 1993)* 13 (9): 1321–29. doi:10.1016/j.str.2005.05.013.

Comte, Pascal, Sergei Vassiliev, Sheridan Houghten, and Doug Bruce. 2011. "Genetic Algorithm with Alternating Selection Pressure for Protein Side-Chain Packing and pK(a) Prediction." *Bio Systems* 105 (3). Elsevier Ireland Ltd: 263–70. doi:10.1016/j.biosystems.2011.05.013.

Conlan, Brendon, Nicholas Cox, Ji Hu Su, Warwick Hillier, Johannes Messinger, Wolfgang Lubitz, P. Leslie Dutton, and Tom Wydrzynski. 2009. "Photo-Catalytic Oxidation of a Di-Nuclear Manganese Centre in an Engineered Bacterioferritin 'Reaction Centre.'" *Biochimica et Biophysica Acta - Bioenergetics* 1787: 1112–21. doi:10.1016/j.bbabio.2009.04.011.

Crichton, Robert R., and Jean Paul Declercq. 2010. "X-Ray Structures of Ferritins and Related Proteins." *Biochimica et Biophysica Acta - General Subjects*. doi:10.1016/j.bbagen.2010.03.019.

DAU, H, and M HAUMANN. 2008. "The Manganese Complex of Photosystem II in Its Reaction cycle—Basic Framework and Possible Realization at the Atomic Level." *Coordination Chemistry Reviews* 252 (3-4): 273–95. doi:10.1016/j.ccr.2007.09.001.

Dautant, Alain, Jean Brice Meyer, Joseph Yariv, Gilles Précigoux́, Robert M. Sweet, A. Joseph Kalb, and Felix Frolow. 1998. "Structure of a Monoclinic Crystal Form of Cytochrome b1 (Bacterioferritin) from E. Coli." *Acta Crystallographica Section D: Biological Crystallography* 54: 16–24. doi:10.1107/S0907444997006811.

De Groot, Bert L., Tomaso Frigato, Volkhard Helms, and Helmut Grubmüller. 2003. "The Mechanism of Proton Exclusion in the Aquaporin-1 Water Channel." *Journal of Molecular Biology* 333 (2): 279–93. doi:10.1016/j.jmb.2003.08.003.

Dekker, J P, and R Van Grondelle. 2000. "Primary Charge Separation in Photosystem II." *Photosynthesis Research* 63 (3): 195–208. doi:10.1023/A:1006468024245.

Emerson, R, and W Arnold. 1932. "THE PHOTOCHEMICAL REACTION IN PHOTOSYNTHESIS." *The Journal of General Physiology* 16: 191–205. doi:10.1085/jgp.16.2.191.

Fajer, J, D C Borg, a Forman, D Dolphin, and R H Felton. 1970. "Pi-Cation Radicals and Dications of Metalloporphyrins." *Journal of the American Chemical Society* 92 (11): 3451–59. http://www.pubmedcentral.nih.gov/articlerender.fcgi?artid=319414&tool=pmcentrez&rendertype=abstract.

Farquhar, James, Aubrey L Zerkle, and Andrey Bekker. 2011. “Geological Constraints on the Origin of Oxygenic Photosynthesis.” *Photosynthesis Research* 107: 11–36. doi:10.1007/s11120-010-9594-0.

Ferreira, Kristina N, Tina M Iverson, Karim Maghlaoui, James Barber, and So Iwata. 2004. “Architecture of the Photosynthetic Oxygen-Evolving Center.” *Science (New York, N.Y.)* 303: 1831–38. doi:10.1126/science.1093087.

Force, Dee Ann, David W Randall, Gary A Lorigan, Keri L Clemens, and R David Britt. 1998. “ESEEM Studies of Alcohol Binding to the Manganese Cluster of the Oxygen Evolving Complex of Photosystem II”, no. 18: 13321–33.

Forrest, Lucy R, and Barry Honig. 2005. “An Assessment of the Accuracy of Methods for Predicting Hydrogen Positions in Protein Structures.” *Proteins* 61: 296–309. doi:10.1002/prot.20601.

Frisch, M. J., Trucks, G. W., Schlegel, H. B., Scuseria, G. E., Robb, M. A., et al. “Gaussian 09, Revision A.1”. Wallingford CT: Gaussian, Inc.

Frolow, F, A J Kalb, and J Yariv. 1994. “Structure of a Unique Twofold Symmetric Haem-Binding Site.” *Nature Structural Biology* 1: 453–60. doi:10.1038/nsb0794-453.

Gabdulkhakov, Azat, Albert Guskov, Matthias Broser, Jan Kern, Frank Müh, Wolfram Saenger, and Athina Zouni. 2009. “Probing the Accessibility of the Mn(4)Ca Cluster in Photosystem II: Channels Calculation, Noble Gas Derivatization, and Cocrystallization with DMSO.” *Structure (London, England : 1993)* 17 (9): 1223–34. doi:10.1016/j.str.2009.07.010.

Georgescu, Roxana E, Emil G Alexov, and Marilyn R Gunner. 2002. “Combining Conformational Flexibility and Continuum Electrostatics for Calculating pK(a)s in Proteins.” *Biophysical Journal* 83 (4). Elsevier: 1731–48. doi:10.1016/S0006-3495(02)73940-4.

Gouterman, Martin, Georges H. Wagni[?]re, and Lawrence C. Snyder. 1963. “Spectra of Porphyrins : Part II. Four Orbital Model.” *Journal of Molecular Spectroscopy* 11: 108–27. doi:10.1016/0022-2852(63)90011-0.

Govindjee, and David Krogmann. 2004. “Discoveries in Oxygenic Photosynthesis (1727-2003): A Perspective.” *Photosynthesis Research* 80: 15–57. doi:10.1023/B:PRES.0000030443.63979.e6.

Gunner, R, Dan E Robertson, and Leslie Dutton. 1986. “Kinetic Studies on the Reaction Center Protein from”, no. 1: 3783–95.

Guskov, Albert, Jan Kern, Azat Gabdulkhakov, Matthias Broser, Athina Zouni, and Wolfram Saenger. 2009. “Cyanobacterial Photosystem II at 2.9-A Resolution and the Role of Quinones, Lipids, Channels and Chloride.” *Nature Structural & Molecular Biology* 16 (3): 334–42. doi:10.1038/nsmb.1559.

Gust, Devens, Thomas A Moore, and Ana L Moore. 2009. “Solar Fuels via Artificial Photosynthesis.” *Accounts of Chemical Research* 42: 1890–98. doi:10.1021/ar900209b.

Hasegawa, J, Y Ozeki, K Ohkawa, M. Hada, and H. Nakatsuji. 1998. “Theoretical Study of the Excited States of Chlorin, Bacteriochlorin, Pheophytin a , and Chlorophyll a by the SAC/SAC−CI Method.” *The Journal of Physical Chemistry B* 102: 1320–26. doi:10.1021/jp972894o.

Hasegawa, Koji, and Takumi Noguchi. 2005. “Density Functional Theory Calculations on the Dielectric Constant Dependence of the Oxidation Potential of Chlorophyll: Implication for the High Potential of P680 in Photosystem II.” *Biochemistry* 44: 8865–72. doi:10.1021/bi050273c.

Havelius, Kajsa G V, and Stenbjörn Styring. 2007. “pH Dependent Competition between Y(Z) and Y(D) in Photosystem II Probed by Illumination at 5 K.” *Biochemistry* 46 (26): 7865–74. doi:10.1021/bi700377g.

Hawkins, G D, C J Cramer, and D G Truhlar. 1996. “Parametrized Models of Aqueous Free Energies of Solvation Based on Pairwise Descreening of Solute Atomic Charges from a Dielectric Medium.” *Journal of Physical Chemistry* 100: 19824–39. doi:10.1021/jp961710n.

Heimdal, Jimmy, Kasper P Jensen, Ajitha Devarajan, and Ulf Ryde. 2007. “The Role of Axial Ligands for the Structure and Function of Chlorophylls.” *Journal of Biological Inorganic Chemistry : JBIC : A Publication of the Society of Biological Inorganic Chemistry* 12: 49–61. doi:10.1007/s00775-006-0164-z.

Hetterscheid, Dennis G H, and Joost N H Reek. 2011. “Me2-NHC Based Robust Ir Catalyst for Efficient Water Oxidation.” *Chemical Communications (Cambridge, England)* 47: 2712–14. doi:10.1039/c0cc05108j.

Hill, Robert. 1937. “© 1937 Nature Publishing Group.” *Nature* 139: 3225.

Hingorani, Kastoori, Brendon Conlan, Warwick Hillier, and Tom Wydrzynski. 2009. “Elucidating Photochemical Pathways of Tyrosine Oxidation in an Engineered Bacterioferritin ‘Reaction Centre.’” *Australian Journal of Chemistry* 62 (10): 1351. doi:10.1071/CH09264.

Ho, Felix M. 2008. “Uncovering Channels in Photosystem II by Computer Modelling: Current Progress, Future Prospects, and Lessons from Analogous Systems.” *Photosynthesis Research* 98 (1-3): 503–22. doi:10.1007/s11120-008-9358-2.

Ho, Felix M, and Stenbjörn Styring. 2008. “Access Channels and Methanol Binding Site to the CaMn4 Cluster in Photosystem II Based on Solvent Accessibility Simulations, with Implications for Substrate Water Access.” *Biochimica et Biophysica Acta* 1777 (2): 140–53. doi:10.1016/j.bbabio.2007.08.009.

Hoelsch, Kathrin, Ilka Sührer, Moritz Heusel, and Dirk Weuster-Botz. 2012. “Engineering of Formate Dehydrogenase: Synergistic Effect of Mutations Affecting Cofactor Specificity and Chemical Stability.” *Applied Microbiology and Biotechnology*. doi:10.1007/s00253-012-4142-9.

Hohmann-Marriott, Martin F, and Robert E Blankenship. 2011. “Evolution of Photosynthesis.” *Annual Review of Plant Biology* 62: 515–48. doi:10.1146/annurev-arplant-042110-103811.

Holzwarth, A R, M G Müller, M Reus, M Nowaczyk, J Sander, and M Rögner. 2006. “Kinetics and Mechanism of Electron Transfer in Intact Photosystem II and in the Isolated Reaction Center: Pheophytin Is the Primary Electron Acceptor.” *Proceedings of the National Academy of Sciences of the United States of America* 103: 6895–6900. doi:10.1073/pnas.0505371103.

Hou, Harvey J M, and David Mauzerall. 2011. “Listening to PS II: Enthalpy, Entropy, and Volume Changes.” *Journal of Photochemistry and Photobiology. B, Biology* 104 (1-2). Elsevier B.V. 357–65. doi:10.1016/j.jphotobiol.2011.03.007.

Hu, Zhongqiao, and Jianwen Jiang. 2008. “Molecular Dynamics Simulations for Water and Ions in Protein Crystals.” *Langmuir : The ACS Journal of Surfaces and Colloids* 24 (8): 4215–23. doi:10.1021/la703591e.

Hu, Zhongqiao, Jianwen Jiang, and Stanley I Sandler. 2008. “Water in Hydrated Orthorhombic Lysozyme Crystal: Insight from Atomistic Simulations.” *The Journal of Chemical Physics* 129 (7): 075105. doi:10.1063/1.2969811.

Huzisige, Hirosi, and Bacon Ke. 1993. “Dynamics of the History of Photosynthesis Research.” *Photosynthesis Research*. doi:10.1007/BF00146418.

Ishikita, Hiroshi, and Ernst-Walter Knapp. 2005. “Control of Quinone Redox Potentials in Photosystem II: Electron Transfer and Photoprotection.” *Journal of the American Chemical Society* 127 (42): 14714–20. doi:10.1021/ja052567r.

———. 2006. “Function of Redox-Active Tyrosine in Photosystem II.” *Biophysical Journal* 90: 3886–96. doi:10.1529/biophysj.105.076984.

Ishikita, Hiroshi, Bernhard Loll, Jacek Biesiadka, Wolfram Saenger, and Ernst-Walter Knapp. 2005. “Redox Potentials of Chlorophylls in the Photosystem II Reaction Center.” *Biochemistry* 44: 4118–24. doi:10.1021/bi047922p.

Ishikita, Hiroshi, Wolfram Saenger, Jacek Biesiadka, Bernhard Loll, and Ernst-Walter Knapp. 2006. “How Photosynthetic Reaction Centers Control Oxidation Power in Chlorophyll Pairs P680, P700, and P870.” *Proceedings of the National Academy of Sciences of the United States of America* 103: 9855–60. doi:10.1073/pnas.0601446103.

Jakob, Manuela, Alexander Berg, Eli Stavitski, Erin T. Chernick, Emily a. Weiss, Michael R. Wasielewski, and Haim Levanon. 2006. “Photoinduced Electron Transfer through Hydrogen Bonds in a Rod-like Donor–acceptor Molecule: A Time-Resolved EPR Study.” *Chemical Physics* 324 (1): 63–71. doi:10.1016/j.chemphys.2005.11.044.

Jensen, Morten Ø, Sanghyun Park, Emad Tajkhorshid, and Klaus Schulten. 2002. “Energetics of Glycerol Conduction through Aquaglyceroporin GlpF.” *Proceedings of the National Academy of Sciences of the United States of America* 99 (10): 6731–36. doi:10.1073/pnas.102649299.

Jiang, Zhongyi, Hong Wu, Songwei Xu, and Shufang Huang. 2002. “ENZYMATIC CONVERSION OF CARBON DIOXIDE TO METHANOL BY DEHYDROGENASES ENCAPSULATED IN SOL-GEL MATRIX” 47 (2): 2002.

Joliot, P., G. Barbieri, and R. Chabaud. 1969. “Un Nouveau Modele Des Centres Photochimiques Du Systeme II.” *Photochem. Photobiol.* 10: 309–29. doi:10.1111/j.1751-1097.1969.tb05696.x.

Kal, Laxmikant, Robert Skeel, Milind Bhandarkar, Robert Brunner, Attila Gursoy, Neal Krawetz, James Phillips, Aritomo Shinozaki, Krishnan Varadarajan, and Klaus Schulten. 1999. “NAMD2 : Greater Scalability for Parallel Molecular Dynamics” 312: 283–312.

Kee, Hooi Ling, Christine Kirmaier, Qun Tang, James R Diers, Chinnasamy Muthiah, Masahiko Taniguchi, Joydev K Laha, et al. 2007. “Effects of Substituents on Synthetic Analogs of Chlorophylls . Part 2 : Redox Properties , Optical Spectra and Electronic Structure”, no. 26: 1125–43.

Klapper, Michael H. 1991. “Electrochemical Properties of Tyrosine Phenoxy and Tryptophan Indolyl Radicals In Peptides and Amino Acid Analoguest”, 3416–19.

Kok, B, B Forbush, and M McGloin. 1970. “Cooperation of Charges in Photosynthetic O2 Evolution-I. A Linear Four Step Mechanism.” *Photochemistry and Photobiology* 11: 457–75. doi:10.1111/j.1751-1097.1970.tb06017.x.

Krausz, Elmars, Joseph L Hughes, Paul Smith, Ron Pace, and Sindra Peterson Arsköld. 2005. "Oxygen-Evolving Photosystem II Core Complexes: A New Paradigm Based on the Spectral Identification of the Charge-Separating State, the Primary Acceptor and Assignment of Low-Temperature Fluorescence." *Photochemical & Photobiological Sciences : Official Journal of the European Photochemistry Association and the European Society for Photobiology* 4: 744–53. doi:10.1039/b417905f.

Le Bihan, D, E Breton, D Lallemand, P Grenier, E Cabanis, and M Laval-Jeantet. 1986. "MR Imaging of Intravoxel Incoherent Motions: Application to Diffusion and Perfusion in Neurologic Disorders." *Radiology* 161: 401–7. doi:10.1148/radiology.161.2.3763909.

Leibl, W, J Breton, J Deprez, and H W Trissl. 1989. "Photoelectric Study on the Kinetics of Trapping and Charge Stabilization in Oriented PS II Membranes." *Photosynthesis Research* 22 (3): 257–75. doi:10.1007/BF00048304.

Li, Lin, Chuan Li, Subhra Sarkar, Jie Zhang, Shawn Witham, Zhe Zhang, Lin Wang, Nicholas Smith, Marharyta Petukh, and Emil Alexov. 2012. "DelPhi: A Comprehensive Suite for DelPhi Software and Associated Resources." *BMC Biophysics* 5 (1). BMC Biophysics: 9. doi:10.1186/2046-1682-5-9.

Lin, Chia Ling, May Yang Fang, and Shu H. Cheng. 2002. "Substituent and Axial Ligand Effects on the Electrochemistry of Zinc Porphyrins." *Journal of Electroanalytical Chemistry* 531: 155–62. doi:10.1016/S0022-0728(02)01056-2.

Loll, Bernhard, Jan Kern, Wolfram Saenger, Athina Zouni, and Jacek Biesiadka. 2005. "Towards Complete Cofactor Arrangement in the 3.0 A Resolution Structure of Photosystem II." *Nature* 438 (7070): 1040–44. doi:10.1038/nature04224.

Lubitz, Wolfgang, Friedhelm Lendzian, and Robert Bittl. 2002. "Radicals, Radical Pairs and Triplet States in Photosynthesis." *Accounts of Chemical Research* 35 (5): 313–20. http://www.ncbi.nlm.nih.gov/pubmed/12020169.

Mahboob, Abdullah, Serguei Vassiliev, Prashanth K Poddutoori, Art van der Est, and Doug Bruce. 2013. "Factors Controlling the Redox Potential of ZnCe6 in an Engineered Bacterioferritin Photochemical 'Reaction Centre'." *PloS One* 8 (7): e68421. doi:10.1371/journal.pone.0068421.

Marenich, Aleksandr V, Ryan M Olson, Casey P Kelly, Christopher J Cramer, and Donald G Truhlar. 2007. "Self-Consistent Reaction Field Model for Aqueous and Nonaqueous Solutions Based on Accurate Polarized Partial Charges." *Journal of Chemical Theory and Computation* 3: 2011–33. doi:10.1021/ct7001418.

McConnell, Iain L, Vladimir M Grigoryants, Charles P Scholes, William K Myers, Ping-Yu Chen, J W Whittaker, and Gary W Brudvig. 2012. "EPR-ENDOR

Characterization of (17O, 1H, 2H) Water in Manganese Catalase and Its Relevance to the Oxygen-Evolving Complex of Photosystem II." *Journal of the American Chemical Society* 134: 1504–12. doi:10.1021/ja203465y.

Merrick, Jeffrey P, Damian Moran, and Leo Radom. 2007. "An Evaluation of Harmonic Vibrational Frequency Scale Factors." *The Journal of Physical Chemistry. A* 111: 11683–700. doi:10.1021/jp073974n.

Miller, Anne Frances, and Gary W Brudvig. 1989. "Manganese and Calcium Requirements for Reconstitution of Oxygen-Evolution Activity in Manganese-Depleted Photosystem II Membranes." *Biochemistry* 28 (20). American Chemical Society: 8181–90. doi:10.1021/bi00446a033.

Minnetun, M, and Raymond J Abraham. 1984. "The Nmr Spectra of Porphyrins-25'" 40 (17): 3263–72.

Moore, Gary F, Michael Hambourger, Gerdenis Kodis, Weston Michl, Devens Gust, Thomas A Moore, and Ana L Moore. 2010. "Effects of Protonation State on a Tyrosine-Histidine Bioinspired Redox Mediator." *The Journal of Physical Chemistry. B* 114: 14450–57. doi:10.1021/jp101592m.

Murray, James W, and James Barber. 2007. "Structural Characteristics of Channels and Pathways in Photosystem II Including the Identification of an Oxygen Channel." *Journal of Structural Biology* 159 (2): 228–37. doi:10.1016/j.jsb.2007.01.016.

Nelson, Nathan, and Adam Ben-Shem. 2004. "The Complex Architecture of Oxygenic Photosynthesis." *Nature Reviews. Molecular Cell Biology* 5: 971–82. doi:10.1038/nrm1525.

Nugent, Jonathan H a, Richard J Ball, and Michael C W Evans. 2004. "Photosynthetic Water Oxidation: The Role of Tyrosine Radicals." *Biochimica et Biophysica Acta* 1655 (1-3): 217–21. doi:10.1016/j.bbabio.2003.09.015.

Parent, Alexander R., Robert H. Crabtree, and Gary W. Brudvig. 2013. "Comparison of Primary Oxidants for Water-Oxidation Catalysis." *Chemical Society Reviews*. doi:10.1039/c2cs35225g.

Patiño, Rodrigo, Myriam Campos, and Luis Alfonso Torres. 2007. "Strength of the Zn-N Coordination Bond in Zinc Porphyrins on the Basis of Experimental Thermochemistry." *Inorganic Chemistry* 46: 9332–36. doi:10.1021/ic0702522.

Poddutoori, Prashanth K., Ann Dion, Songjie Yang, Melanie Pilkington, John D. Wallis, and Art van der Est. 2010. "Light-Induced Hole Transfer in a Hypervalent phosphorus(V) Octaethylporphyrin Bearing an Axially Linked Bis(ethylenedithio)tetrathiafulvalene." *Journal of Porphyrins and Phthalocyanines* 14 (02): 178–87. doi:10.1142/S108842461000191X.

Prokhorenko, Valentin I., and Alfred R. Holzwarth. 2000. “Primary Processes and Structure of the Photosystem II Reaction Center: A Photon Echo Study.” *The Journal of Physical Chemistry B* 104: 11563–78. doi:10.1021/jp002323n.

Radmer, Richard, and Otto Ollinger. 1983. “Topography of the O2-Evolving Site Determined with Water Analogs.” *FEBS Letters* 152 (1): 39–43. doi:10.1016/0014-5793(83)80477-3.

Rappaport, Fabrice, Mariana Guergova-Kuras, Peter J Nixon, Bruce A Diner, and Jérôme Lavergne. 2002. “Kinetics and Pathways of Charge Recombination in Photosystem II.” *Biochemistry* 41: 8518–27. doi:Doi 10.1021/Bi025725p.

Rigby, Stephen E J, Jonathan H A Nugent, and Patrick J O Malleyl. 1994. “ENDOR and Special Triple Resonance Studies of Chlorophyll Cation Radicals in Photosystem 27” 2: 10043–50.

Rutherford, A.W., and J.E. Mullet. 1981. “Reaction Center Triplet States in Photosystem I and Photosystem II.” *Biochimica et Biophysica Acta (BBA) - Bioenergetics* 635 (2): 225–35. doi:10.1016/0005-2728(81)90022-0.

Saito, Keisuke, a William Rutherford, and Hiroshi Ishikita. 2013. “Mechanism of Tyrosine D Oxidation in Photosystem II.” *Proceedings of the National Academy of Sciences of the United States of America* 110 (19): 7690–95. doi:10.1073/pnas.1300817110.

Schatz, G H, H Brock, and a R Holzwarth. 1987. “Picosecond Kinetics of Fluorescence and Absorbance Changes in Photosystem II Particles Excited at Low Photon Density.” *Proceedings of the National Academy of Sciences of the United States of America* 84 (23): 8414–18. http://www.pubmedcentral.nih.gov/articlerender.fcgi?artid=299554&tool=pmcentrez&rendertype=abstract.

Sieckmann, Ina, and Klaus Brettel. 1993. “Transient Electron Paramagnetic Resonance of the Triplet State of”, 4842–47.

Siegbahn, Per E M. 2013. “Substrate Water Exchange for the Oxygen Evolving Complex in PSII in the S1, S2, and S3 States.” *Journal of the American Chemical Society* 135 (25): 9442–49. doi:10.1021/ja401517e.

Siegbahn, Per E M, and Margareta R a Blomberg. 2004. “Important Roles of Tyrosines in Photosystem II and Cytochrome Oxidase.” *Biochimica et Biophysica Acta* 1655 (1-3): 45–50. doi:10.1016/j.bbabio.2003.07.003.

Simmerling, Carlos, Bentley Strockbine, and Adrian E Roitberg. 2002. “All-Atom Structure Prediction and Folding Simulations of a Stable Protein.” *Journal of the*

American Chemical Society 124 (38): 11258–59. http://www.ncbi.nlm.nih.gov/pubmed/12236726.

Song, Yifan, Junjun Mao, and M R Gunner. 2009. "MCCE2: Improving Protein pKa Calculations with Extensive Side Chain Rotamer Sampling." *Journal of Computational Chemistry* 30: 2231–47. doi:10.1002/jcc.21222.

Song, Yifan, Ekaterina Michonova-Alexova, and M R Gunner. 2006. "Calculated Proton Uptake on Anaerobic Reduction of Cytochrome C Oxidase: Is the Reaction Electroneutral?" *Biochemistry* 45: 7959–75. doi:10.1021/bi052183d.

Sproviero, Eduardo M, José a Gascón, James P McEvoy, Gary W Brudvig, and Victor S Batista. 2007. "Quantum Mechanics/molecular Mechanics Structural Models of the Oxygen-Evolving Complex of Photosystem II." *Current Opinion in Structural Biology* 17 (2): 173–80. doi:10.1016/j.sbi.2007.03.015.

Sproviero, Eduardo M, James P McEvoy, José a Gascón, Gary W Brudvig, and Victor S Batista. 2008. "Computational Insights into the O2-Evolving Complex of Photosystem II." *Photosynthesis Research* 97 (1): 91–114. doi:10.1007/s11120-008-9307-0.

Stowell, M H, T M McPhillips, D C Rees, S M Soltis, E Abresch, and G Feher. 1997. "Light-Induced Structural Changes in Photosynthetic Reaction Center: Implications for Mechanism of Electron-Proton Transfer." *Science (New York, N.Y.)* 276: 812–16. doi:10.1126/science.276.5313.812.

Tan, Chunhu, Lijiang Yang, and Ray Luo. 2006. "How Well Does Poisson-Boltzmann Implicit Solvent Agree with Explicit Solvent? A Quantitative Analysis." *The Journal of Physical Chemistry. B* 110: 18680–87. doi:10.1021/jp063479b.

Tommos, Cecilia, and Gerald T. Babcock. 2000. "Proton and Hydrogen Currents in Photosynthetic Water Oxidation." *Biochimica et Biophysica Acta - Bioenergetics*. doi:10.1016/S0005-2728(00)00069-4.

Tyystjärvi, Esa, Marja Hakala, and Päivi Sarvikas. 2005. "Mathematical Modelling of the Light Response Curve of Photoinhibition of Photosystem II." *Photosynthesis Research* 84 (1-3): 21–27. doi:10.1007/s11120-004-7174-x.

Umena, Yasufumi, Keisuke Kawakami, Jian-Ren Shen, and Nobuo Kamiya. 2011. "Crystal Structure of Oxygen-Evolving Photosystem II at a Resolution of 1.9 Å." *Nature* 473: 55–60. doi:10.1038/nature09913.

Vasil'ev, Sergej, and Doug Bruce. 2006. "A Protein Dynamics Study of Photosystem II: The Effects of Protein Conformation on Reaction Center Function." *Biophysical Journal* 90 (9). Elsevier: 3062–73. doi:10.1529/biophysj.105.076075.

Wang, Junmei, Piotr Cieplak, and Peter a. Kollman. 2000. "How Well Does a Restrained Electrostatic Potential (RESP) Model Perform in Calculating Conformational Energies of Organic and Biological Molecules?" *Journal of Computational Chemistry* 21 (12): 1049–74. doi:10.1002/1096-987X(200009)21:12<1049::AID-JCC3>3.0.CO;2-F.

Williams, J C, R G Alden, H A Murchison, J M Peloquin, N W Woodbury, and J P Allen. 1992. "Effects of Mutations near the Bacteriochlorophylls in Reaction Centers from Rhodobacter Sphaeroides." *Biochemistry* 31: 11029–37. doi:10.1021/bi00160a012.

Witt, H. T. 1996. "Primary Reactions of Oxygenic Photosynthesis." *Berichte Der Bunsengesellschaft Für Physikalische Chemie* 100: 1923–42. doi:10.1002/bbpc.19961001202.

Wraight, Colin A. 2006. "Chance and Design--Proton Transfer in Water, Channels and Bioenergetic Proteins." *Biochimica et Biophysica Acta* 1757 (8): 886–912. doi:10.1016/j.bbabio.2006.06.017.

Wydrzynski, Tom, Warwick Hillier, and Johannes Messinger. 1996. "On the Functional Significance of Substrate Accessibility in the Photosynthetic Water Oxidation Mechanism." *Physiologia Plantarum* 96 (2). Blackwell Publishing Ltd: 342–50. doi:10.1111/j.1399-3054.1996.tb00224.x.

Yruela, I, P J van Kan, M G Müller, and A R Holzwarth. 1994. "Characterization of a D1-D2-Cyt B-559 Complex Containing 4 Chlorophyll a/2 Pheophytin a Isolated with the Use of MgSO4." *FEBS Letters* 339: 25–30. doi:10.1016/0014-5793(94)80377-3.

Zhang, L, and J Hermans. 1996. "Hydrophilicity of Cavities in Proteins." *Proteins* 24 (4): 433–38. doi:10.1002/(SICI)1097-0134(199604)24:4<433::AID-PROT3>3.0.CO;2-F.

Zheng, Zhong, and M R Gunner. 2009. "Analysis of the Electrochemistry of Hemes with E(m)s Spanning 800 mV." *Proteins* 75: 719–34. doi:10.1002/prot.22282.

Zhou, H X, S T Wlodek, and J A McCammon. 1998. "Conformation Gating as a Mechanism for Enzyme Specificity." *Proceedings of the National Academy of Sciences of the United States of America* 95: 9280–83. doi:10.1073/pnas.95.16.9280.

Zhou, Huan-Xiang, Stanislaw T Wlodek, and J Andrew McCammon. 1998. "Conformation Gating as a Mechanism for Enzyme Specificity." *Proceedings of the National Academy of Sciences* 95 (16): 9280–83. http://www.pnas.org/content/95/16/9280.abstract.

Zhu, F, E Tajkhorshid, and K Schulten. 2001. “Molecular Dynamics Study of Aquaporin-1 Water Channel in a Lipid Bilayer.” *FEBS Letters* 504 (3): 212–18. http://www.ncbi.nlm.nih.gov/pubmed/11532456.

Zhukov, L., and A.H. Barr. 2002. “Oriented Tensor Reconstruction: Tracing Neural Pathways from Diffusion Tensor MRI.” *IEEE Visualization, 2002. VIS 2002.* doi:10.1109/VISUAL.2002.1183799.